UNIVERSITY OF CALIFORNIA
Los Angeles

Tuning magnetism and superconductivity in topological material candidates

A dissertation submitted in partial satisfaction
of the requirements for the degree
Doctor of Philosophy in Physics

by

Tiema Qian

2024

ABSTRACT OF THE DISSERTATION

Tuning magnetism and superconductivity in topological material candidates

by

Tiema Qian
Doctor of Philosophy in Physics
University of California, Los Angeles, 2024
Professor Ni Ni, Chair

Since the theoretical proposals of topological phases of matter and topological phase transitions, the experimental realization of topological materials and associated emerging phenomena had become an essential goal in condensed matter physics. The experimental discoveries of the quantum Hall effect (QHE), the quantum spin Hall effect (QSHE), and three-dimensional (3D) time-reversal symmetry protected topological insulators (TIs) further sparked intensive research effort, leading to a kaleidoscope of topological phases and realizations of diverse topological materials, such as Dirac semimetals, Weyl semimetals, magnetic topological insulators, topological superconductor, etc. A topological phase of matter is distinguished from trivial materials by showing a nonzero topological invariant and topologically protected surface states, which result in exotic phenomena in its transport, thermodynamic, optical and other physical properties. Practically, new topological phases may be realized by combining the topological band structure with other physical aspects. For example, breaking time reversal symmetry in an existing TI by introducing ferromagnetism or net magnetization, a gaped surface state with dissipationless edge conduction may emerge, resulting in the quantum anomalous Hall effect (QAHE) in the absence of external magnetic field.

My thesis focuses on the study of topological materials with two major research themes. One is the synthesis, characterization and tuning of ternary Mn-Bi-Te magnetic topological

insulators, including the synthetic exploration of new magnetic topological insulators, with a focus on the investigation of the interplay of magnetism and band topology through doping and external pressure. The other involves investigating proposed topological superconductor candidates through external stimuli, such as uniaxial strain and hydrostatic pressure, to enhance our understanding of superconductivity in such material systems.

QAHE was first realized in magnetically doped TI $Cr_{0.15}(Bi_{0.1}Sb_{0.9})_{0.85}Te_{0.3}$ thin film in 2013. However, doped materials brought inevitable sample inhomogeneity, and thus the phenomenon was only observed at very low temperature, in the range of mK. To overcome this material challenge, it is believed that intrinsic magnetic TIs, i.e., stoichiometric magnetic TIs without doping, will be superior due to their higher magnetic and electronic homogeneity compared to doped materials. The first intrinsic magnetic TI $MnBi_2Te_4$ was discovered in 2018. It is an antiferromagnetic (AFM) TI with van der Wall (vdW) coupling that orders below 24 K. Its spins align ferromagnetically (FM) in individual planes but AFM between neighboring layers. Due to its vdW nature, it can be exfoliated and fabricated into odd-layer devices with net magnetization, theoretically proposed as QAH insulators, or into even-layer devices that preserve AFM, proposed as axion insulators. QAH effect was soon observed experimentally at 1.6 K and zero field in a 5-layer device with Hall signal plateau at $0.998h/e^2$ while Layer Hall effect and quantum metric nonlinear Hall effect were observed in 6-layer devices. To better engineer the magnetic properties of this family, growth trails had led to the discovery of new intrinsic magnetic TIs that with alternating $[Bi_2Te_3]$ and magnetic $[MnBi_2Te_4]$ layers, forming the natural heterostructural series of $MnBi_{2n}Te_{3n+2}$. In this family of compound, Mn layer is brought apart by adding more layers of Bi_2Te_3, causing the phase to eventually evolve from AFM TI in $MnBi_2Te_4$ to FM axion insulator in $MnBi_8Te_{13}$.

Although field-induced quantized Hall conductance has been reported by a few groups in both odd- and even-layer $MnBi_2Te_4$ devices, there is only one report showing the observation of zero-field QAHE. Several major reasons why it remains challenging to realize QAH in this system: chemical disorders in the bulk samples; chemical disorders introduced during

the device fabrication process; weak net magnetism in odd-layer devices. Synthesis efforts are needed to reduce the chemical disorders, particularly the Mn_{Bi} antisites that are most detrimental to the realization of a universal surface gap and thus QAH, to improve the outcome while the weak net magnetism in devices can be addressed by achieving a ferromagnetic (FM) ground state in bulk sample. $Mn(Bi_{1-x}Sb_x)_2Te_4$ was made with the hope that it might address the problems. The doping indeed induces FM ground state of the Mn sublattice. However, it also significantly increases the Mn_{Bi} antisite concentration from around 2% to about 16%, forming a secondary FM Mn sublattice that aligns antiferromagnetically with the dominant Mn sublattice. As a result, the Hall conductance in devices made from Sb-doped samples is far from the quantization value. Therefore, progress in solving this outstanding material challenge remains unsatisfactory. The theme of my thesis work on the Mn-Bi-Te system focuses on addressing these issues by conducting doping trials to suppress Mn_{Bi} antisites (chapter 3), investigating the competition between FM and AFM energy scales in the system (chapter 4), and searching for new magnetic topological insulators (chapter 5).

Chapter 3 reports our study of the effect of Pb substitution of Mn in $MnBi_2Te_4$. We grew single crystals of $(Mn_{1-x}Pb_x)Bi_2Te_4$ ($0 \leq x \leq 0.82$) and investigated the evolution of crystal structure, magnetic order and band topology upon doping. With increasing x, the amount of the Mn_{Bi} antisites is reduced, and the magnetic dilution effect manifested as a decrease of ordering temperature and magnetic interactions is observed. First-principles density functional theory calculations (DFT) reveal potential topological phase transitions in this doping series with two gapless points appear at $x = 0.44$ and $x = 0.66$. Chapter 4 summarizes our study of the effect of hydrostatic pressure on the metamagnetic phase transitions in the Sb doped $MnBi_4Te_7$ series. We show that external pressure, which enhances the interlayer hopping without introducing chemical disorders, triggers multiple metamagnetic transitions upon cooling in the topological van der Waals magnets $Mn(Bi_{1-x}Sb_x)_4Te_7$, where the antiferromagnetic interlayer superexchange coupling competes with the ferromagnetic interlayer coupling mediated by the antisite Mn spins. The temperature–pressure phase diagrams reveal that while the ordering temperature from the paramagnetic to ordered states is almost

pressure-independent, the metamagnetic transitions show nontrivial pressure and temperature dependence, even re-entrance. For these highly anisotropic magnets, we attribute the former to the ordering temperature being only weakly dependent on the intralayer parameters and the latter to the parametrically different pressure and temperature dependence of the two interlayer couplings. Our independent probing of these disparate magnetic interactions paves an avenue for efficient magnetic manipulations in van der Waals magnets. Chapter 5 reports our synthetic exploration which leads to the discovery of new magnetic topological insulators. By doping Mn into $(Ge_{1-\delta})_2Bi_2Te_5$, we successfully grew $(Ge_{1-\delta-x}Mn_x)_2Bi_2Te_5$ ($x \leq 0.47$, $0.11 \leq \delta \leq 0.20$) single crystals. Upon doping up to $x = 0.47$, the lattice parameter c decreases by 0.8%, while the lattice parameter a remains nearly unchanged. Significant Ge vacancies and Ge/Bi site mixing are revealed via elemental analysis as well as refinements of the neutron and X-ray diffraction data, resulting in holes dominating the charge transport. At $x = 0.47$, below 10.8 K, a bilayer A-type antiferromagnetic ordered state emerges, featuring an ordered moment of 3.0(3) μ_B/Mn at 5 K, with the c axis as the easy axis. Magnetization data unveil a much stronger interlayer antiferromagnetic exchange interaction and a much smaller uniaxial anisotropy compared to $MnBi_2Te_4$. We attribute the former to the shorter superexchange path and the latter to the smaller ligand-field splitting in $(Ge_{1-\delta-x}Mn_x)_2Bi_2Te_5$. Our study demonstrates that this series of materials holds promise for the investigation of the Layer Hall effect and quantum metric nonlinear Hall effect.

Topological superconductors are proposed to host intriguing phenomena such as Majorana fermions, which form the foundation of topological quantum computing. Chapter 6 of this dissertation summarizes our study of the uniaxial-strain tuning of superconductivity in the Kagome topological superconductor candidate CsV_3Sb_5. It shows a superconducting temperature $T_c = 3.3$ K and a charge-density-wave (CDW) temperature at $T_{CDW} = 94.5$ K. Upon applying uniaxial strain from -0.90% to 0.90%, we found T_c increases while T_{CDW} decreases. These opposite response suggests strong competition between these two orders. Comparison with hydrostatic pressure measurements indicate that it is the change in the c axis that is responsible for these behaviors of the CDW and superconducting transitions, and

that the explicit breaking of the sixfold rotational symmetry by strain has a negligible effect. Combined with our first-principles calculations and phenomenological analysis, we conclude that the enhancement in T_c with decreasing lattice parameter c is caused primarily by the suppression of T_{CDW}, rather than strain-induced modifications in the bare superconducting parameters. We propose that the sensitivity of T_{CDW} with respect to the changes in the c axis arises from the impact of the latter on the trilinear coupling between the M_1^+ and L_2^- phonon modes associated with the CDW. Overall, our work reveals that the c-axis lattice parameter, which can be controlled by both pressure and uniaxial strain, is crucial for the phase diagram of CsV_3Sb_5.

In summary, we have successfully reduced the amount of the Mn_{Bi} antisites by substituting Mn with Pb in $MnBi_2Te_4$ and revealed the roles of the interlayer coupling, intralayer coupling and magnetic anisotropy play in tuning the competition between AFM and FM energy scales in Sb doped $MnBi_4Te_7$ by applying hydrostatic pressure. Moreover, structure engineering helps us to discover new topological insulating phase $(Ge_{1-\delta-x}Mn_x)_2Bi_2Te_5$. Our work on the strain effect in topological superconductor candidate CsV_3Sb_5 has revealed the competition between CDW and superconductivity and suggested the important role of the trilinear coupling of phonon modes in CDW. Our work advances the understanding of the interplay of magnetism, band topology and superconductivity in magnetic/superconducting topological material systems.

The dissertation of Tiema Qian is approved.

Stuart Brown

Christopher Gutiérrez

Chee Wei Wong

Ni Ni, Committee Chair

University of California, Los Angeles

2024

I would like to dedicate this thesis to my precious wife Chuqi Cai.

Table of Contents

List of Figures . . . . . **xiii**

List of Tables . . . . . **xxi**

Acknowledgements . . . . . **xxiv**

Curriculum Vitae . . . . . **xxvi**

1 Introduction to Band Topology, Magnetism and Superconductivity . . . **1**

1.1 Hall effects and band topology 2

1.1.1 Classical Hall effects 3

1.1.2 Quantum Hall effect 4

1.1.3 Quantum Spin Hall effect 7

1.1.4 Quantum Anomalous Hall effect 9

1.2 Theory of topology 11

1.2.1 Berry phase 12

1.2.2 Chern Number 13

1.2.3 $\mathbb{Z}_2$ invariant and topological insulator 14

1.2.4 Majorana Fermion 16

1.3 Magnetism 16

1.3.1 Magnetic orders 17

1.3.2 Magnetic exchange interaction 17

1.3.3 Magnetic anisotropy 18

1.3.4 Zeeman energy 19

1.3.5 Stoner-Wohlfarth model . . . 19
1.4 Superconductivity . . . 20
1.4.1 Macroscopic interpretations . . . 20
1.4.2 Microscopic picture . . . 21
1.4.3 Charge density wave . . . 22
1.5 Introduction to Magnetic topological insulators $MnBi_{2n}Te_{3n+1}$ . . . 23
1.5.1 The first intrinsic AFM TI $MnBi_2Te_4$ . . . 23
1.5.2 Natural Heterostructures . . . 25
1.5.3 Growth and Characterization . . . 25
1.5.4 Magnetic and Transport Properties . . . 27
1.5.5 Antisites and Doping . . . 29

2 Experimental Techniques . . . 31
2.1 Material Growth . . . 31
2.1.1 High-temperature Flux Growth . . . 31
2.1.2 Chemical Vapor Transport Growth . . . 33
2.2 Structure Determination and Chemical Analysis . . . 34
2.2.1 X-ray Diffraction . . . 34
2.2.2 Neutron Diffraction . . . 35
2.2.3 Energy- and Wavelength- Dispersive X-ray Spectroscopy . . . 35
2.3 Physical Property Measurements . . . 36
2.3.1 Electrical Transport Measurements . . . 37
2.3.2 Specific Heat Measurements . . . 37
2.3.3 Magnetic Property Measurements . . . 38
2.3.4 Uniaxial Strain Measurements . . . 38

2.3.5 Hydrostatic Pressure Measurements 40

3 Magnetic dilution effect and topological phase transitions in magnetic topological insulator ($Mn_{1-x}Pb_x$)Bi_2Te_4 41

3.1 Introduction 41

3.2 Obtaining ($Mn_{1-x}Pb_x$)Bi_2Te_4 single crystals 44

3.3 Results 44

3.3.1 Magnetic and electrical transport properties 49

3.3.2 Band topology engineering 55

3.4 Discussion 56

3.5 Summary and Outlook 61

4 Unconventional Pressure-Driven Metamagnetic Transitions in Topological van der Waals Magnets 62

4.1 Introduction 62

4.2 Result 64

4.3 Discussion 67

4.4 Summary and outlook 74

5 Single crystal growth, chemical defects, magnetic and transport properties of antiferromagnetic topological insulators ($Ge_{1-\delta-x}Mn_x$)$_2Bi_2Te_5$ ($x \leq 0.47$, $0.11 \leq \delta \leq 0.20$) 75

5.1 Introduction 75

5.2 Experimental methods 77

5.3 Experimental Results 80

5.3.1 Growth optimization and phase characterization 80

5.3.2 Magnetic and Transport properties of $(Ge_{1-\delta-x}Mn_x)_2Bi_2Te_5$ single crystals . . . 81
5.3.3 Crystal and Magnetic Structure . . . 84
5.4 Discussion . . . 92
5.5 Summary and Outlook . . . 94

6 Revealing the competition between charge-density wave and superconductivity in CsV_3Sb_5 through uniaxial strain . . . 95
6.1 Introduction . . . 95
6.2 Methods . . . 97
6.3 Experimental results . . . 101
6.4 Discussion . . . 106
6.5 Summary and Outlook . . . 110

7 Conclusion . . . 111

A Additional Structural Refinement of $(Ge_{1-\delta-x}Mn_x)_2Bi_2Te_5$ ($x \leq 0.47$, $0.11 \leq \delta \leq 0.20$) . . . 113
A.1 Neutron diffraction to determine stacking . . . 113
A.2 Powder X-ray Refinement . . . 114
A.2.1 Determine vacancy amount . . . 114
A.2.2 Determine vacancy position . . . 115

Bibliography . . . 120

List of Figures

1.1 The predictions and discoveries of different types of Hall effects in chronological order. H and M are external field and magnetism, respectively. Figures are adapted from [8] 2

1.2 Quantum Hall effect: (a-c) Evolution of landau levels under magnetic field from low to high. The fields are in the ratio of $2:3:4$ giving v as 4, 8/3 and 2. (b) Localized cycling electrons in the bulk and chiral edge states on the boundary under field. (c) Transport behavior showing the quantized Hall resistance R_{xy} and vanishing longitudinal resistance R_{xx} at high field. Figures are adapted from Ref. [14]. 5

1.3 A comparison between a trivial insulator, a quantum Hall material and a quantum spin Hall system. For a insulating state, a gap is present at all values of momentum since the outer electrons are pinned by their atoms. In the quantum Hall state, the gap is crossed by conducting edge states. In the quantum spin Hall state, the edge states that cross the gap carry counterpropagating currents of spin-up and spin-down electrons. Figures are adapted from Ref. [16]. 8

1.4 The electronic strutcture of a MTI at its 2D limit, and QAHE in Cr-doped $(Bi/Sb)_2Te_3$ thin films. (a) The Dirac-like dispersion of the edge state in a 2D MTI that connects the surface states gap due to the magnetism. (b) the chiral edge mode that becomes apparent in a 2D MTI device when the Fermi level is located in the surface gap. (c) Magnetic field dependence of ρ_{xy} at different gating voltage in $(Bi/Sb)_2Te_3$ thin films. (d) Magnetic field dependence of ρ_{xx} at different gating voltage. Figures are adapted from Ref. [3, 6]. 10

1.5 Comparison between normal state and charge density wave state of material in terms of real space and band structure. (a) shows the normal state with evenly spaced atoms and electron density with a periodicity of a. Gaps open at the edge of Brillouin zone at $\pm\pi/a$. (b) depictes a distortion of lattice and electron with a periodicity at $2a$. Additional gaps open at $\pm\pi/2a$. Figures are adapted from Ref. [21]. 22

1.6 Growth and characterization of $MnBi_{2n}Te_{3n+1}$. (a) Phase diagrm of the quasi-binary MnTe-Bi_2Te_3, in which small growth window for compounds can be seen, taken from [23]. (b) XRD data for (00l) surface for $MnBi_{2n}Te_{3n+1}$ family. 24

1.7 Evolution of magnetism in $MnBi_{2n}Te_{3n+1}$. (a-d): Magnetic structure for single crystal $MnBi_2Te_4$, $MnBi_4Te_7$, $MnBi_6Te_{10}$ and $MnBi_8Te_{13}$, respectively. (e-h): The temperature-dependent magnetic susceptibility measured with in-plane and out-of-plane magnetic fields. (i-l): Isothermal magnetization under in-plane and out-of-plane fields at 2 K. Insets of (j-l): The magnetization hysteresis loop near zero field. This figure is taken from Ref. [28]. 28

2.1 Bragg's condition for constructive interference that gives a peak in XRD pattern. 34

2.2 Schematic of uniaxial strain and hydrostatic pressure measurement. (a) and (b) show the home built three-piezostack strain apparatus, L and l marks the length of piezostack and width of the gap that the sample is strained. White arrows show the movement of the piezostack when tensile strain is applied to the sample. (c) and (d) show the hydrostatic pressure apparatus that measures transport and magnetization properties. The major difference is that a channel is needed at the bottom of (c) so conducting wire can be passed through to measure electric signals, while no contacts are needed for magnetization measurement. 39

3.1 Schematic drawing of the crystal and magnetic structure of $MnBi_{2n}Te_{3n+1}$ ($n = 0, 1, 2, 3$ and 4) with the stacking sequence listed. Purple arrows indicate the spin direction for Mn atoms in different layers. Inset: Manetic ordering temperature T_c verses interlayer distance between the adjacent Mn-Mn layers d_{Mn-Mn} and n versus d_{Mn-MN}. Figures are adapted from Ref. [31]. 43

3.2 X-ray diffraction of $(Mn_{1-x}Pb_x)Bi_2Te_4$. (a) PXRDs for various concentrations. Inset: the zoom-in plot of the (1 0 7) PXRD peak. (b) The doping-dependent relative lattice parameters a/a_0, c/c_0 and nominal concentration used in growth. a_0 and c_0 are the lattice parameters of $MnBi_2Te_4$. 46

3.3 The evolution of temperature-dependent properties of $(Mn_{1-x}Pb_x)Bi_2Te_4$. Top row: $\chi(T)$, the temperature-dependent magnetic susceptibility under 0.01 T with $H \parallel$ c. Middle row: $\rho_{xx}(T)$, the temperature-dependent electrical resistivity with the current along the ab plane. Ordering temperature T_N for each concentration is marked and a correlation between two measurements can be observed. Bottom row: $1/\chi(T)$, the inverse magnetic susceptibility measured at 1 T above T_N. Curie-Weiss fits are shown in solid lines. 47

3.4 The evolution of magnetic-field-dependent properties of $(Mn_{1-x}Pb_x)Bi_2Te_4$. First row: $M(H)$, the isothermal magnetization at 2 K with $H \parallel c$. The reflection-point criterion used to determine the H_s is shown for $x \geq 0.53$. Second row: $\rho_{xx}(H)$, the magnetic field dependence of electrical resistivity with the current along the ab plane and $H \parallel c$. Third row: $\rho_{xy}(H)$, the Hall resistivity with the current along ab plane and $H \parallel c$. Fourth row: $\rho^A_{xy}(H)$, the anomalous Hall resistivity calculated by subtracting linear Hall background in $\rho_{xy}(H)$. 48

3.5 The temperature-dependent neutron peak intensity at magnetic reflection (1 0 -0.5) for the $x = 0.37$ sample. Order parameter fit results in a value of $\beta = 0.44(2)$. Curves with $\beta = 0.36$ (3D Heisenberg case) and $\beta = 0.32$ (3D Ising case) are also shown for comparison. 51

3.6 Pressure measurement of the $x = 0.37$ sample. (a) The temperature dependence of ρ_{xx} at different pressures. T_N is marked by black arrows. (b) The evolution of T_N with pressure. Linear fits of both data were shown in lines. (c) The field dependence of ρ_{xx} at different pressures with offset. H_s is marked by black arrows. (d) The evolution of H_s with pressure. Linear fit is shown in line. 52

3.7 (a) The bulk band structure of $MnBi_2Te_4$ and (b) $PbBi_2Te_4$. The blue and red dots indicate the weight of the Bi-p orbitals and Te-p orbitals, respectively. (c) The gap value at Γ and Z point as a function of SOC strength for $MnBi_2Te_4$ and (d) $PbBi_2Te_4$. (e) The minimum bulk band gap along Γ - Z as function of Pb content. 54

3.8 (a) The doping dependence of the Curie-Weiss temperature, (b) The doping dependence of the Curie-Weiss effective moment per Mn, (c) The doping dependence of the magnetic moment per Mn for $x = 0$ (2 K, 7.7 T) and $x > 0$ (2 K, 7 T), (d) Néel temperature vs. x, Néel temperature vs. $(a - a_0)/a_0$ and Néel temperature vs. $(c - c_0)/c_0$ for the pressure work (Ref. [56]) and this doping work, (e) Spin-flop field and saturation field determined from magnetic and transport measurements with $H \parallel c$, (f) The doping dependence of the $effective$ (see the main text) interlayer plane-plane coupling per Mn site SJ_c and the $effective$ magnetic anisotropy per Mn SK. All lines are guides to the eye. 57

4.1 (a): The crystal structure of $Mn(Bi_{1-x}Sb_x)_4Te_7$. Sb doping can introduce $Mn_{(Bi,Sb)}$ antisites. Mn1 represents the Mn atoms on the Mn site; Mn2 labels the Mn atoms on the (Bi, Sb) site in the SLs; Mn3 denotes the Mn atoms on the (Bi, Sb) site in the QLs. (b) The temperature-dependent resistivity, $\rho(T)$ of $x = 0.48$ sample under ambient pressure, with schematics of the magnetic structures [60]. Upon cooling, Mn1 sublattice undergoes PM $\rightarrow$ AFM $\rightarrow$ FM transitions. In these ordered states, Mn1 and Mn2 sublattices are always AFM to each other along the c axis while Mn3 spins are paramagnetic. Right inset: its magnetoresistance MR(H) in the FM state (2 K) and AFM state (10 K). 65

4.2 The effect of external pressures on the electrical properties of $Mn(Bi_{1-x}Sb_x)_4Te_7$ (x = 0, 0.48, 0.57, 0.67 and 0.76). (a)-(e) $\rho(T)$ at different pressures with the current $I//ab$ plane. (f)-(j): MR(H) at 2 K under pressures with $I//ab$ and $H//c$. The sharp drop in MR indicates the Mn1 spins are at the AFM state while the MR showing weak field dependence suggests FM state of the Mn1 spins. 66

4.3 The effect of external pressures on the magnetic properties of $Mn(Bi_{1-x}Sb_x)_4Te_7$ (x = 0.57, 0.67 and 0.76): (a), (c), (f) The temperature dependant ZFC and FC magnetic susceptibility $\chi(T)$ with $H//c$. (b), (g): The isothermal magnetization $M(H)$ at 2 K at different pressures for x = 0.57 (b), and 0.76 (g). (d), (e) and (h): at fixed pressures, the $M(H)$ curves at different temperatures for x = 0.67 ((d) and (e)), and x = 0.76 (h). $M(H)$ data are analyzed to remove the lead signal, so slight discontinuity in data are induced. 68

4.4 (a)-(e) Temperature-pressure ($T-P$) phase diagrams for $Mn(Bi_{1-x}Sb_x)_4Te_7$ (x = 0, 0.48, 0.57, 0.67 and 0.76) under pressures. T_C and T_N are the magnetic ordering temperatures of a PM to FM or AFM transition, respectively. T_{M1} and T_{M2} are the metamagnetic temperatures where an AFM $\rightarrow$ FM transition or a FM $\rightarrow$ AFM transition appears upon cooling, respectively. T_N^R, T_C^R and T_{M1}^R were extracted by taking the first derivative of resistivity data. T_N^M, T_C^M, T_{M1}^M and T_{M2}^M are determined by the first derivative of magnetic susceptibility data and then confirmed with isothermal magnetization measurements across critical temperatures. Note: the □/■ phase line representing the AFM to FM metamagnetic transition upon cooling is a first-order phase line while the others are all second-order phase lines. (f) Typical behavior of susceptibility in a system with antiferromagnetic or spin-glass type correlations. The blue/red/green lines correspond to $T_{CW} \approx 3, 7$ and 15. note that in a limited temperature range shown by pink shading, χ can either grow, decay, or show non-monotonic behavior. . . 69

5.1 (a) Crystal structures of Bi_2Te_3 QL, XBi_2Te_4 SL and $X_2Bi_2Te_5$ NL. (b) (0 0 L) Bragg peaks of different X-Bi-Te series. Inset: an as-grown hexagonal single crystal of GeMn225 ($x = 0.47$) against a mm-grid. (c) PXRD of $(Ge_{1-\delta-x}Mn_x)_2Bi_2Te_5$. (d) $x_{nominal}$ vs. x_{WDS} when growing GeMn225. (e) Lattice parameters a and c of $(Ge_{1-\delta-x}Mn_x)_2Bi_2Te_5$, dashed line shows the linear fit of lattice parameters. . 78

5.2 Thermodynamic and transport properties of GeMn225. (a) Temperature dependent magnetic susceptibility under 0.1 T for different doping levels and direction. Inset: inverse magnetic susceptibility measured at 1 T above T_N. Curie-Weiss fit is shown in solid line. (b) Normalized temperature-dependent electrical resistivity with current along the ab plane for different doping levels. Inset: temperature-dependence of specific heat of the $x = 0.47$ sample with the criterion to determine T_N. 82

5.3 (a) Isothermal magnetization at 2 K of GeMn225 with $H \parallel c$. (b) Isothermal magnetization measured at 2 K up to 14 T for the $x = 0.47$ sample with $H \parallel ab$ and $H \parallel c$. (c) Field-dependence of MR of GeMn225. (d) MR at various temperatures for the $x = 0.47$ sample. (e) Field-dependence of Hall resistivity. Dotted lines refer to H_{sf} in the $x = 0.33$ and 0.47 samples. 83

5.4 Magnetic order parameter at magnetic reflection (0 1 1) for the $x = 0.47$ sample measured at DEMAND. The blue line depicts the best fit using the mean-field power law, see text. Left inset: the magnetic structure. Right inset: the intensity of the (0 1 0) and (0 0 4) peak above and below T_N. 90

5.5 (a) Isothermal magnetization of the $x = 0.47$ sample at 2 K. The red line is the experimental curve and the black dashed line is a linear extrapolation of the magnetization at 2 K, it reaches to 4.5 μ_B/Mn at around 30 T. (b) Crystal structure of X225 (X = GeMn) and X124 (X = Mn). The superexchanges are indicated with red arrows, the nearest-neighbor Mn-Mn distances are highlighted with olive lines. (c) Distorted $MnTe_6$ octahedron, the building blocks of the magnetic layer in the 124 and 225 phases. The Mn atom in the center refers to the circled one in (b). Different Te-Mn-Te bond angels are shown, the asymmetry in GeMn225 arises from its asymmetric next-nearest-neighbor environment. . . . 91

6.1 a) The $(00l)$ x-ray diffraction peaks of the cleaved ab plane for CsV_3Sb_5. Inset: a piece of single crystal against a 1-mm scale with the a and b axes labeled. b) The zoomed-in temperature-dependent electrical resistivity $\rho_{xx}(T)$ near the superconducting transition with the current along the a axis. Left inset: The crystal structure of CsV_3Sb_5. Right inset: $\rho_{xx}(T)$ from 2 K to 300 K. c) The ZFC and FC susceptibilities measured at 10 Oe with $H||ab$. To minimize the demagnetization factor, a thin plate with a thickness $\sim$0.05mm was selected for the measurement and H was applied to be parallel to the sample plate. Inset: the mapping of the actual strain on the sample, see text for more details. . . . 98

6.2 Strain dependence of T_{CDW} of a single crystal of CsV_3Sb_5. (a) Temperature dependence of the in-plane resistance of CsV_3Sb_5 near the CDW transition measured at different strain values. Negative values denote compressive strain, whereas positive values, tensile strain. (b) The temperature-derivative of the resistance, dR_{xx}/dT, whose peaks determine T_{CDW}. (c) T_{CDW} and resistance as a function of strain applied along the a-axis. Resistance is linearly proportional to the strain applied. 100

6.3 Strain dependence of T_c of CsV_3Sb_5. (a) Temperature dependence of the in-plane resistance R_{xx} of CsV_3Sb_5 near the superconducting transition. (b) Strain dependence of the resistance at 6 K and of T_c, which is determined by the 50%-resistance criterion. Resistance is linearly proportional to the strain applied. (c) Magnetic field dependence of the in-plane resistance in the presence of an applied 0.90% tensile strain. (d) H_{c2} diagram of CsV_3Sb_5 subjected to different strain values. Solid lines are fittings to the Ginzburg-Landau model. 102

6.4 Comparison between the phase diagrams obtained from uniaxial strain measurements (this work) and previous hydrostatic pressure measurements [143, 144] (a) The effect of the change in lattice parameter a on T_{CDW} and T_c. The relationship between the lattice parameters and pressure was obtained from Ref. [145]. (b) The effect of the change in volume V on T_{CDW} and T_c. The response of the lattice parameter c with respect to the strain was extracted from DFT calculations. (c) The effect of the change in c on T_{CDW} and T_c. (d) T_c plotted as a function T_{CDW} for both pressure and uniaxial strain experiments. 103

6.5 (a) Left: the displacement pattern of the M_1^+ phonon mode. For clarity, only the vanadium ions and two consecutive kagome layers are shown. Red, blue, and green arrows correspond to displacements according to the M_1, M_2 and M_3 components. Right: Same as the left panel, but for the L_2^- mode. (b) Unstable phonon frequencies as a function of the c lattice parameter from first principles calculations. Because the squared phonon frequencies are negative for unstable modes, we plot the square root of the absolute value of the squared frequencies. (c) Electronic density of states (DOS) of CsV_3Sb_5, calculated from DFT, in the high temperature, high symmetry phase, as a function of the lattice parameter c. The inset is a zoom of the low-energy part of the spectrum. The van Hove singularity peak below the Fermi level is suppressed under compression of the c-axis. 108

List of Tables

1.1 Summary of the chemical, structural, magnetic properties of $MnBi_{2n}Te_{3n+1}$ from $n = 1$ to 4. Here, T_{growth} means the temperature that the growth was finished and flux was spun out. Table adapted from Ref. [28]. 26

3.1 Data summary of $(Mn_{1-x}Pb_x)Bi_2Te_4$. x refers to the molar ratio of Pb/(Pb+Mn) obtained by the WDS measurements. The lattice parameters obtained by PDXR refinement (a and c in Å). The effective magnetic momentum (μ_{eff} in μ_B/Mn) and Curie-Weiss temperature (T_{CW} in K) are calculated from Fig. 3.3 (see text), effective magnetic anisotropy (SK in meV) and effective interlayer magnetic interaction (SJ_c in meV) are obtained from magnetization measurements shown in the first row of Fig. 3.4 (see text), charge carrier density (n in $10^{20}cm^{-3}$) is calculated from Hall measurements shown in the third row of Fig. 3.4 (see text). 45

3.2 Refined structural parameters for the x =0.37 sample based on the single crystal neutron diffraction data. (number of reflections: 192; $R_F = 3.83\%$; $\chi^2 = 28.7$). χ^2 here is large because the experimental error bars are smaller than the standard deviation from merging equivalent reflections. 53

5.1 Summary of the $(Ge_{1-\delta-x}Mn_x)_2Bi_2Te_5$ series. All doped compounds are grown by the CVT method with MnI_2 as the transport agent while the parent compound is made by the flux method as discussed in the text. *: the ratio of $Ge_{1-x}Mn_xTe$: Bi_2Te_3 : MnI_2. a and c are the lattice parameters. T_N is the AFM transition temperature. p_1 is the charge carrier density calculated from Hall measurements via $p_1 = B/e\rho_{yx}$, p_2 is the charge carrier density estimated by $p_2 = 2\delta/A$, where A is the unit cell volume in cm^3. Both p_1 and p_2 has the unit of $\times 10^{20}cm^{-3}$ . . 79

5.2 Refined crystal structural parameters for the parent compound Ge225 based on the PXRD data measured at 300 K. The refinement is constrained by the WDS result. Number of reflections: 6474; $R_F = 8.42\%$; $\chi^2 = 46.4$. 86

5.3 Refined magnetic and crystal structural parameters for the x =0.47 sample based on the single crystal neutron diffraction measurement at 5 K constrained by WDS result. Number of reflections: 38; $R_F = 12.8\%$; $\chi^2 = 7.12$. 87

5.4 Comparison in Mn-Bi-Te family. SJ_c is the interlayer exchange coupling per Mn and SK is the uniaxial magnetic anisotropy. L_1 and L_2 refer to the nearest-neighbor Mn-Mn interlayer distances shown in Fig. 5.5 (b). α and β are the bond angles of the distorted $MnTe_6$ octahedron shown in the inset of Fig 5.5 (c). 89

A.1 Refined structural parameters for the x =0.53 sample based on the single crystal neutron diffraction data for stacking A, where Mn is located on site 2d, or inner layers. (for magnetic refinement, number of reflections: 38; $R_F = 9.83\%$; $\chi^2 = 5.56$) 114

A.2 Refined structural parameters for the x =0.53 sample based on the single crystal neutron diffraction data for stacking B, where Mn is located on site 2c, or outer layers. (for magnetic refinement, number of reflections: 38; $R_F = 16.5\%$; $\chi^2 = 9.04$) 115

A.3 Refined structural parameters for the x =0.53 sample based on the single crystal neutron diffraction data for mixed stacking. (for magnetic refinement, number of reflections: 38; $R_F = 11.7\%$; $\chi^2 = 6.38$) 116

A.4 Refined structural parameters for the $Ge_2Bi_2Te_5$ sample based on the powder X-ray sample with only Ge on both site 1 and site 2. ((Number of reflections: 6474; $R_F = 8.56\%$; $\chi^2 = 46.1$) 117

A.5 Refined structural parameters for the $Ge_2Bi_2Te_5$ sample based on the powder X-ray sample with only Bi on both site 1 and site 2. ((Number of reflections: 6474; $R_F = 8.64\%$; $\chi^2 = 45.8$) 117

A.6 Refined structural parameters for $Ge_2Bi_2Te_5$ sample based on the powder X-ray sample with WDS result been forced. The vacancy is all in site $2d$ ((Number of reflections: 6474; $R_F = 8.64\%$; $\chi^2 = 45.8$) 118

A.7 Refined structural parameters for $Ge_2Bi_2Te_5$ sample based on the powder X-ray sample with WDS result been forced. The vacancy is evenly distributed on site $2d$ and $2c$ ((Number of reflections: 6474; $R_F = 8.64\%$; $\chi^2 = 45.8$) 119

Acknowledgements

My Ph.D. journey has been joyful and life-changing. There are difficult and struggling times as well as fruitful and satisfied moments. I am grateful for the support from many people who helped during my Ph.D.

First and foremost, I would like to express my gratitude to Dr. Ni Ni for her support and mentorship as my supervisor. During my Ph.D. program, her unique vision and knowledge has always inspired and motivated my works. Her pedagogical approaches focus on helping me understand the underlying principles rather than simply providing the answers to my questions. Throughout her academic networks, I am able to interact with top scientists through our collaborations and travel to conferences to present my results. I feel very lucky to be a member in Dr. Ni Ni's lab.

I would also want to thank my colleges in Ni's lab. I learned and mastered experimental skills under the help of Chaowei Hu and Eve Emmanouilidou, who are like my big brother and sister. Discussions with them not only help me improve my research skills but also broaden my perspective in physics. I enjoy working with J Green, who joined the group with me. Daily discussions with J and growing together as researchers were truly enjoyable experiences. I would also like to thank Jonathan Loera, Asari Prado and Shuai Sun, who join the group as new generations. The mentoring experience had taught me a lot on communication skills. Lastly, I want to thank undergraduate researchers Qiaozhi Xu, Patrick Liu and Jiawei Qiu for their assistant.

During the years as a Ph.D. student, I understand the importance of collaboration and I would like to thank our wonderful collaborators. Huibo Cao and Erxi Feng helped us with many neutron diffraction measurements. Tay-Rong Chang's group at NCKU helped with band structure calculation. Igor Mazin from GMU helped with magnetic interaction analysis so we have a better understanding with the experimental results. Brian Andersen, Rafael Fernandes and Rutan Birol from University of Copenhagen and University of Minnesota on the theoretical calculation on Kagome superconductor. A special thanks to Suyang Xu and

Qiong Ma and their from Harvard University and Boston College. Discussion with them helps deepen my understanding of topological materials in device study.

I would like to thank all the help from UCLA physics department. It was a peasure to be a part of the condensed matter experimental journal club with Prof. Stuart Brown's, Prof. Anshul Kogar's, Prof. Christopher Gutiérrez's and Prof. Qianhui Shi's groups. Meeting and discuss with them greatly expand my vision as a condensed matter researcher. Finally, I would like to thank Prof. Brown, Prof. Gutiérrez and Prof. Wong for advising my thesis.

For the past five years, emotional supports from friends are essential for an international student. I would like to express my gratitude to all my friendes who accompanied me during the graduate school years: Yuchao Chen, Xuecheng Xu, Yuxuan Wang, Xiao Li, Haotian Wang, Yitao Chen, Bowen Liu, Jingyuan Dai and many more. It has been a blessing to have them in this journey.

Lastly, I would like to thank my beloved family for their unwavering love and support. I would not be here without the help and support from my parents and grand parents who always encourage my curiosity since my childhood. Also I would like to thank my wife Chuqi, who supported me so much that I can not imagine how I would have finished my degree without her. Thank you for your tender company, that always cheers me up during difficult times.

Curriculum Vitae

June 2019	B.S. in Physics
	B.A. in Music
	University of Washington

Publications

[1] T. Qian, MH. Christensen, C. Hu, A. Saha, Revealing the competition between charge density wave and superconductivity in CsV_3Sb_5 through uniaxial strain," *Physical Review B*, vol. 104, no. 14, pp. 144506, 2021.

[2] T. Qian, Y.-T Yao, C. Hu, E. Feng, H. Cao, I. I. Mazin, TR. Chang, N. Ni , "Magnetic dilution effect and topological phase transitions in $(Mn_{1-x}Pb_x)Bi_2Te_4$," *Physical Review B*, vol. 106, no. 4, pp. 045121, 2022.

[3] T. Qian, E. Emmanouilidou, C. Hu, J. C. Green, I. I. Mazin, and N. Ni, "Unconventional pressure-driven metamagnetic transitions in topological van der waals magnets," *Nano Letters*, vol. 22, no. 13, pp. 5523-5529, 2022.

[4] T. Qian, C. Hu, J. C. Green, E. Feng, H. Cao, and N. Ni, "Single crystal growth, chemical defects, magnetic and transport properties of antiferromagnetic topological insulators $(Ge_{1-\delta-x}Mn_x)_2Bi_2Te_5$ ($x \leq 0.47$, $0.11 \leq \delta \leq 0.20$)," *arXiv preprint*, arXiv:2404.17764 2024.

[5] T. Qian, J. Mutch, L. Wu, P. Went, Q. Jiang, P. Malinowski, J. Yang, J.-H. Chu, "Apparatus design for measuring of the strain dependence of the Seebeck coefficient of single crystals," *Review of Scientific Instruments*, vol. 91, no. 2, 2020.

[6] C. Hu, T. Qian and N. Ni, "Recent progress in $MnBi_{2n}Te_{3n+1}$ intrinsic magnetic topological insulators: crystal growth, magnetism and chemical disorder," *Natinoal Science Review*, vol. 11, no. 2, pp. nwad282, 2023.

[7] J. Mutch, W.-C. Chen, P. Went, T. Qian I. Z. Wilson, A. Andreev, C.-C. Chen, J.-H. Chu, "Evidence for a strain-tuned topological phase transition in $ZrTe_5$," *Science Advances*, vol. 5, no. 8, pp. eaav9771, 2019.

[8] A. Gao, Y.-F. Liu, J.-X. Qiu, B. Ghosh, T. V. Trevisan, Y. Onishi, C. Hu, T. Qian, H.-J. Tien, S.-W. Chen, *et al.* "Quantum metric nonlinear Hall effect in a topological antiferromagnetic heterostructure," *Science*, vol. 381, no. 6654, pp. 181-1861, 2023.

[9] J. Tang, T. S. Ding, H. Chen, A. Gao, T. Qian, Z. Huang, Z. Sun, X. Han, A. Strasser, J. Li *et al.* "Dual quantum spin Hall insulator by density-tuned correlations in TaIrTe4," *Nature*, vol. 628, pp. 515-521, 2024.

CHAPTER 1

Introduction to Band Topology, Magnetism and Superconductivity

For a long time, lattice, orbital and spin degrees of freedom are thought to be the only crucial ingredients in understanding the physical properties of materials. When quantum Hall effect (QHE) was discovered, topology was introduced in condensed matter physics [1]. Since then, the important role of the topology of a material's band structure has been gradually recognized, now band topology has even become a fundamental principle for classifying the states of matter. The classification is governed by topological invariant that arises from the electronic structure. One of the most important features of the topological invariant is that they are robust to external perturbations, making the applications of these materials very alluring. Significant results have been obtained upon studying the interplay between nontrivial topological band structure and other physical properties. These studies have led to the discoveries of various topological phases including 3D topological insulator (TI), magnetic topological insulator (MTI), and topological superconductor [2–4], as well as the discoveries of emergent phenomena including quantum spin Hall effect (QSHE), quantum anomalous Hall effect (QAHE), and so on [5–7]. There is no doubt that our progressive understanding of band topology has reshaped condensed matter physics and materials science. In this chapter, I will start by introducing different Hall effects, followed by the theoretical formalism of band topology. Then, I will briefly introduce magnetism and superconductivity, which link to the MTI and topological superconductor aspects in this dissertation. Lastly, I will introduce the intrinsic Mn-Bi-Te MTI system.

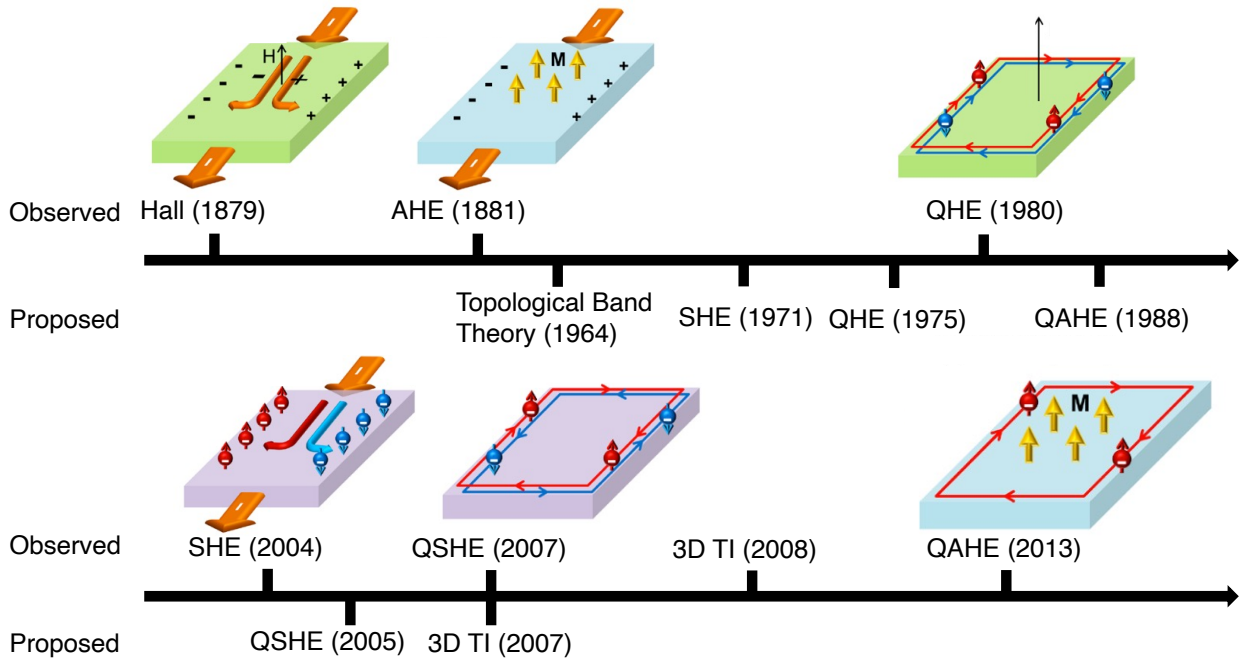

Figure 1.1: The predictions and discoveries of different types of Hall effects in chronological order. H and M are external field and magnetism, respectively. Figures are adapted from [8]

1.1 Hall effects and band topology

The history of predicting and discovering various Hall effects is closely intertwined with the development of topological materials. The theory of band topology was introduced to explain the integer quantum Hall effect (QHE) and was later found to be closely related to all other types of Hall effects. I will go through different kinds of Hall effects as well as their topological aspects. The Hall effect refers to the rise of a voltage difference transverse to the current direction, or in the spin Hall effect, the emergence of a spin current perpendicular to the applied electric field. Three classical Hall effects are categorized, the original Hall effect, the spin Hall effect and the anomalous Hall effect. Corresponding to them are three quantum variants, QAH, QSHE and QAHE. The history of the predictions and discoveries of different Hall effects are marked in Fig. 1.1.

1.1.1 Classical Hall effects

In this section I will briefly introduce three classical Hall effects. The original Hall effect was discovered by Edwin Hall in 1879. When considering a conductor placed in an external magnetic field **B** and current **I**, the charge carriers moving through the sample will be driven by the Lorentz force and accumulate at an edge of the sample. This will then result in a steady electric field across the sample and when the Lorentz force cancels out the resultant electric force, an equilibrium state is reached with the following relationship:

$$\mathbf{F} = q(\mathbf{E} + \mathbf{v} \times \mathbf{B}) = 0 \tag{1.1}$$

The Hall resistivity can be expressed as

$$\rho_{xy} = \frac{V_{xy}}{I_x t}, \tag{1.2}$$

where V_{xy} is Hall voltage and t is the thickness of the sample.

We can then calculate the Hall coefficient, which is defined as the slope of $\rho_{xy}(B)$ and according to Drude model:

$$R_H \equiv \frac{d\rho_{xy}}{dB} = \frac{1}{ne}. \tag{1.3}$$

where n is the charge carrier density and e is electron charge. As a result, a measurement of Hall effect in a sample can be used to identify the major carrier type and the charge carrier density in the sample. This method is commonly used in sample characterization.

While the ordinary Hall effect is induced by an external magnetic field, AHE comes from the intrinsic magnetization of ferromagnetic (FM) materials. The Hall voltage of FM materials shows an anomalous hump close to zero field that corresponds to the envelope of the magnetization. This leads to a nonzero intercept denoted as R_{xy}^A, or the anomalous Hall resistance. One simple understanding is that the internal magnetic field from the FM material provides the Lorentz force to induce AHE, thus the relative strength of R_{xy}^A is proportional to the magnetization. A more comprehensive understanding of AHE involves a combination of intrinsic and extrinsic factors. The intrinsic factor arises from a nonzero integrated Berry curvature over the entire Brillouin zone in the momentum space with the

internal magnetism breaking the time reversal (TR) symmetry. On the other hand, external factors such as side jump or skew scattering that related to impurities could also contribute to AHE [9]. Thus, AHE is not only related to the magnetic structure of a material, but the electronic band information as well. Recently, AHE has played an important role in searching for new magnetic Weyl semimetals and materials with spin textures of non zero scalar spin chirality.

The Spin Hall effect (SHE) was proposed in 1971 [10] and was discovered in doped semiconductors such as GaAs [11]. Compared with the ordinary Hall effect, in which the charge carrier current transports transversely under magnetic field, the SHE arises from a spin current that transports transversely under an electric field. The nature of the SHE leads to difficulties in detecting the effect since the accumulation of spin is hard to observe. Methods like Kerr effect microscopy, spin-polarized scanning tunneling microscopy, or other advanced magnetic sensing techniques are used to confidently detect and characterize the SHE [11, 12]. Like different types of charge carriers carry opposite charge, the sign of the spin currents tells the direction of momentum. The SHE relies on spin-orbit coupling, which is a relativistic quantum mechanical effect [13].

1.1.2 Quantum Hall effect

The first quantized version of the Hall effect, the integer QAH, was discovered in the Si-based metal–oxide–semiconductor field effect transistor in a strong external magnetic field [15]. The successful observation of QAH is attributed to the ideal 2D gas like behavior of electrons in the system. To understand the QAH, we can construct the Hamiltonian under the field $\mathbf{B} = \nabla \times \mathbf{A}$ as

$$H = \frac{1}{2m_e}(\mathbf{p} + e\mathbf{A}(\hat{x}, \hat{y}))^2. \tag{1.4}$$

We then simplify the Hamiltonian with Landau gauge $\mathbf{A} = xB\hat{\mathbf{y}}$ and obtain

$$H = \frac{1}{2m}(p_x^2 + (p_y + eBx)^2) \tag{1.5}$$

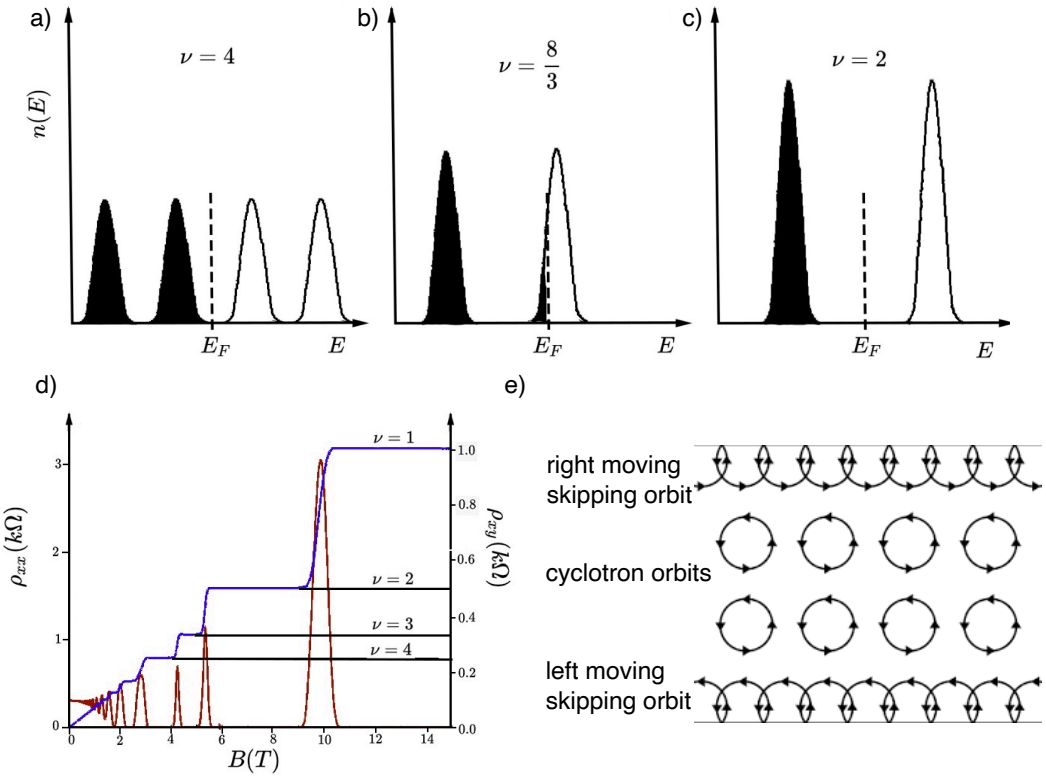

Figure 1.2: Quantum Hall effect: (a-c) Evolution of landau levels under magnetic field from low to high. The fields are in the ratio of $2:3:4$ giving v as 4, 8/3 and 2. (b) Localized cycling electrons in the bulk and chiral edge states on the boundary under field. (c) Transport behavior showing the quantized Hall resistance R_{xy} and vanishing longitudinal resistance R_{xx} at high field. Figures are adapted from Ref. [14].

This can be solved by separation of variables,

$$\psi_k(x,y) = e^{iky} f_k(x) \tag{1.6}$$

Apply the Hamiltonian on this wavefunction, we see that the operator p_y is replaced by its eigenvalue $\hbar k$,

$$\psi_k(x,y) = \frac{1}{2m}(p_x^2 + (\hbar k + eBx)^2)\psi_k(x,y) \equiv H_k\psi_k(x,y). \tag{1.7}$$

This is actually just the Hamiltonian for a harmonic oscillator in the x direction, the only difference being the displacement from the origin as $x + kl_B^2$. The frequency of the harmonic oscillator is the cyclotron frequency $\omega_B = eB/m$ and the characteristic length scale defined as the magnetic length:

$$l_B = \sqrt{\frac{\hbar}{eB}}. \tag{1.8}$$

An interesting factor to note is that the momentum in the y direction has become the position of the harmonic oscillator in the x direction centered at $x = -kl_B^2$. We then reduce the problem to a harmonic oscillator with the energy eigenvalues:

$$E_n = \hbar\omega_B(v + \frac{1}{2}) \tag{1.9}$$

This means that by applying the magnetic field, the system transfers from a free electron system that obeys Dirac-Fermi statistics to a quantized energy state that has energy gap $\hbar\omega_c$ and ground state of $\frac{1}{2}\hbar\omega_B$. Since the energy gap is proportional to B, chemical potentials can be tuned by external field. When the chemical potential lands between the Landau Levels, the sample is insulating or semiconducting in bulk. When the nth Landau level crosses the chemical potential at a certain field, the sample will then be conducting in bulk. The evolution of landau levels across the Fermi energy at different magnetic fields is shown in Fig. 1.2 (a-c). This indicates that when the external field is changing, the resistance of the sample will behave periodically with respect to B^{-1}. As a result, this will give rise to quantum oscillation of resistance or magnetization for a regular band bulk metal or semimetal, as indicated in Fig. 1.2 (d). In our case, in a bulk-insulating Hall state, there exist active conduction channels on the edge and the Hall conductance with:

$$\sigma_{xy} = ve^2/h \tag{1.10}$$

Here, the quantization of the Hall conductivity is closely related to a unique topological invariant called the Chern number, which equals the value v in the Hall conductance. I will discuss this more in the next section of this chapter.

At this moment, we can understand the phenomenon semi-classically. When an external field is applied to the system, electrons in the bulk enter localized cyclotron orbits, thus without free moving electrons, the bulk is a trivial insulator. In case of the conducting edge states, both the direction of the field as well as the carrier type will determine the chirality of the electrons, which will determine the transport direction of a certain edge. As shown in Fig. 1.2 (e), electrons bounce and continue to transport along the 1D edge through skipping cyclotron orbits, forming robust edge transport that is resistant to backscattering. With better sample growth techniques, disorder is decreased followed by more and more plateaux appearing. These plateaux emerge with fractional values of n, with integer levels becoming less prominent.

1.1.3 Quantum Spin Hall effect

The QSHE was theoretically proposed one year after the experimental observation of the SHE [5]. It was proposed in a graphene system and can be considered as two copies of the Haldane model. For the electrons in edge channels, the spin-up electrons exhibit a chiral QHE while the spin-down electrons exhibit an anti-chiral QHE as shown in the lowest panel of Fig. 1.3. The separation of the opposite spin edge states requires materials with an inverted band structure driven by strong spin-orbit coupling (SOC). The opposite states will have opposite Chern number and since time reversal symmetry is still preserved, the Chern number must be 0. Thus, a new topological invariant $\mathbb{Z}_2$ is defined in this case and will be further discussed in the next section.

I would like to explain why the backscattering or hybridization between the spin-up and spin-down states is forbidden as well as why the edge states are protected by time reversal symmetry by introducing the Kramer's degeneracy theorem. It states that for every energy eigenstate of a time reversal symmetric system with half-integer total spin, there is another

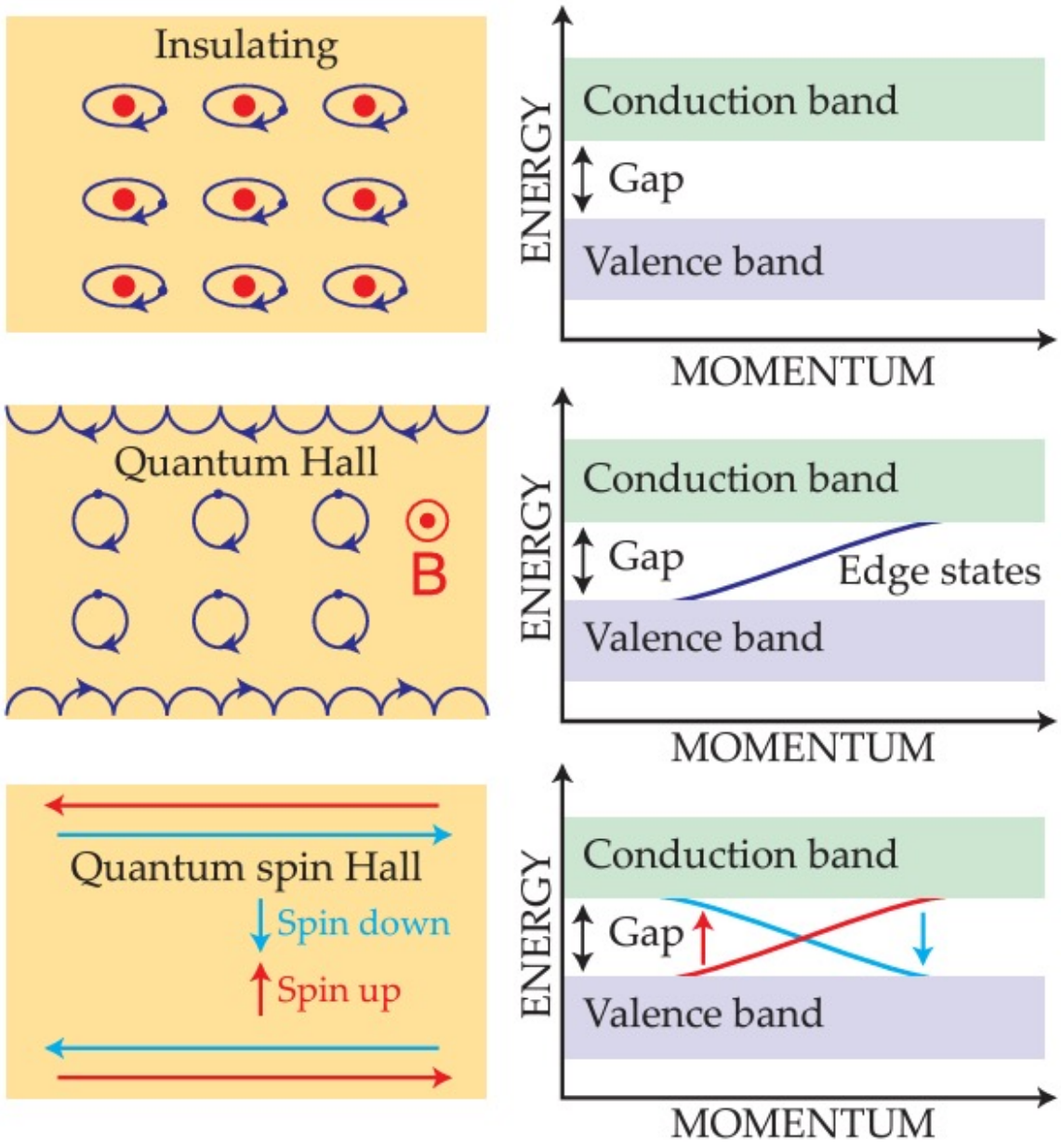

Figure 1.3: A comparison between a trivial insulator, a quantum Hall material and a quantum spin Hall system. For a insulating state, a gap is present at all values of momentum since the outer electrons are pinned by their atoms. In the quantum Hall state, the gap is crossed by conducting edge states. In the quantum spin Hall state, the edge states that cross the gap carry counterpropagating currents of spin-up and spin-down electrons. Figures are adapted from Ref. [16].

eigenstate with the same energy related by time reversal. Since $\mathcal{T}$ is an anti-unitary operator, for integer angular momentum, $\mathcal{T}^2 = 1$ and for half-integer, $\mathcal{T}^2 = -1$, implying the presence of a degenerate state. The opposite-chirality edge states are then the Kramer's degenerate states for each other and the matrix elements of the TR-invariant perturbation between two Kramer's degenerate states vanish identically. Thus the two dissipationless edge conducting states in QSHE are robust against perturbation. A band crossing at the high-symmetry point is required by the Kramer's theorem, as shown in Fig. 1.3, in which two 1D Dirac bands representing opposite edge states cross each other at $k = 0$.

SOC-driven band inversion will be the key feature to realize QSHE, so materials with heavy elements can possess QSHE. For heavy element nuclei, they carry a larger charge and induce a larger magnetic field that leads to the opposite spin states of the electrons. The SOC needs to be large enough to invert the bands to induce QSHE. In HgTe devices, the band inversion between $6s$ and $5p$ orbitals of Hg gives rise to a quantized longitudinal conduction of $2h/e^2$ from the edge states when the chemical potential was tuned to the band gap.

1.1.4 Quantum Anomalous Hall effect

The QAHE is the last of the Hall family to be discovered. It was proposed as early as 1988 by Haldane, who predicted that the QAHE can be realized in graphene lattice with an alternating magnetic field in the neighboring atom [17]. Since a spatially varying magnetic field will break the TRS, quantized Hall resistance with a Chern number of 1 can be realized without the formation of Landau levels, in other words, without an external magnetic field. Due to the difficulties in material realization, it was not until the discovery of 3D topological insulators (TI) that QAHE was brought up again. Without magnetism, TIs have a bulk gap induced by SOC and gapless Dirac surface states that are protected by TRS. When we introduce magnetism into a 2D limit TI, the topological surface state is no longer protected due to broken of TRS. Assuming the magnetization is along z, the new Hamiltonian for the Dirac surface states can be written as:

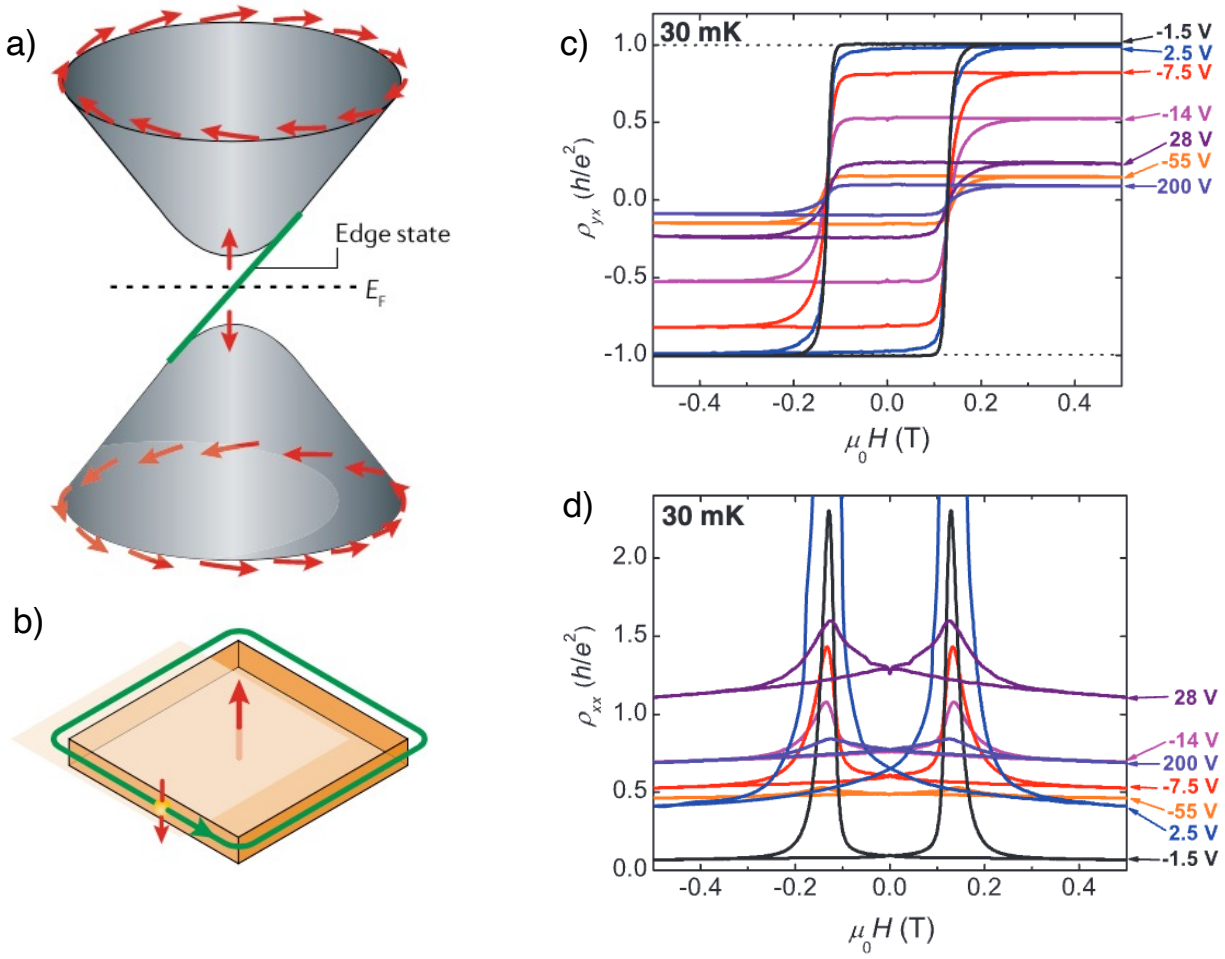

Figure 1.4: The electronic strutcture of a MTI at its 2D limit, and QAHE in Cr-doped $(Bi/Sb)_2Te_3$ thin films. (a) The Dirac-like dispersion of the edge state in a 2D MTI that connects the surface states gap due to the magnetism. (b) the chiral edge mode that becomes apparent in a 2D MTI device when the Fermi level is located in the surface gap. (c) Magnetic field dependence of ρ_{xy} at different gating voltage in $(Bi/Sb)_2Te_3$ thin films. (d) Magnetic field dependence of ρ_{xx} at different gating voltage. Figures are adapted from Ref. [3, 6].

$$H = v_F(-k_y\sigma_x + k_x\sigma_y) + m\sigma z \tag{1.11}$$

Here, v_F is the Fermi velocity of the linear dispersion and σ_i is the Pauli matrices for spin. This Hamiltonian will open a mass gap m at the Dirac point, while within the gap, there are chiral edge states similar to that in the QHE, as shown in Fig. 1.4 (a) and (b). For a nonmagnetic TI, the sample is insulating in the bulk and conducting in the surface if the Fermi level is tuned within the bulk gap. Here the topological phase is characterized by the $\mathbb{Z}_2$ coefficients. As for MTI, if the Fermi level is in the surface gap, both the bulk and the surface will be insulating, but there still exists a dissipationless conduction channel along the edge. The topological state is then characterized by the Chern number of ± 1, and thus a QHE like quantized Hall conductance will appear. A significant difference between the the realization of QHE and QAHE is that in QHE, C reaches 1 at high field when only one Landau level is beneath Fermi level. For QAHE, C is 1 at zero field, meaning the Hall conductivity already quantized at zero field. This will be explained in the later section.

Experimentally, this has been realized by doping magnetic atoms into a existing topological insulator. This was first measured through Cr-doped $(Bi/Sb)_2Te_3$ thin films [6] as shown in Fig. 1.4 (c) and (d). The Hall resistance R_{xy} reaches a quantized value of h/e^2 together with a resistivity drop, showing an insulating bulk surface state and a conducting edge state. Achieving this requires a carefully tuned Fermi level within the gap as well as a temperature as low as 30 mK.

1.2 Theory of topology

In this section I will briefly introduce the theory of topology, including concepts of the Berry phase, the Berry connection, and then how different topological invariants are defined. Lastly, I will discuss how symmetry plays an important role in topology.

1.2.1 Berry phase

Let us consider a band insulator described by a Bloch Hamiltonian $\mathcal{H}(\boldsymbol{k})$ with a crystal momentum $\boldsymbol{k}$. The eigenstates can be obtained by solving the Bloch equation,

$$H(\boldsymbol{k})\,|u_n(\boldsymbol{k}\rangle = E_n(\boldsymbol{k})\,|u_n(\boldsymbol{k})\rangle\,. \tag{1.12}$$

We can then define the rate of change in the wave function $|u_n(\boldsymbol{k})\rangle$ in the momentum apace as the Berry connection:

$$\boldsymbol{\mathcal{A}}^{(n)}(\boldsymbol{k}) = \boldsymbol{i}\,\langle u_n(\boldsymbol{k})|\partial_{\boldsymbol{k}} u_n(\boldsymbol{k})\rangle \tag{1.13}$$

Since the Bloch equation does not fix the phase factor of the solution, there remains a gauge degree of freedom,

$$|u_n(\boldsymbol{k})\rangle \to e^{i\phi_n(\boldsymbol{k})}\,|u_n(\boldsymbol{k})\rangle \tag{1.14}$$

that leads to a gauge transformation in $\boldsymbol{\mathcal{A}}^{(n)}(\boldsymbol{k})$ as:

$$\boldsymbol{\mathcal{A}}^{(n)}(\boldsymbol{k}) \to \boldsymbol{\mathcal{A}}^{(n)}(\boldsymbol{k}) - \partial_k \phi_n(\boldsymbol{k}). \tag{1.15}$$

A gauge-invariant quantity $\mathcal{F}_{ij}^{(n)}(\boldsymbol{k})$ denoted as Berry curvature can then be constructed from $\boldsymbol{\mathcal{A}}^{(n)}(\boldsymbol{k})$ as

$$\mathcal{F}_{ij}^{(n)}(\boldsymbol{k}) = \nabla_k \times \boldsymbol{\mathcal{A}}^{(n)}(\boldsymbol{k}). \tag{1.16}$$

In 2D space, this simplifies to

$$\mathcal{F}_{ij}^{(n)}(\boldsymbol{k}) = \partial_{k_i}\mathcal{A}_{k_j}^{(n)}(\boldsymbol{k}) - \partial_{k_j}\mathcal{A}_{k_i}^{(n)}(\boldsymbol{k}). \tag{1.17}$$

This invariant 'field strength' will have a physical meaning that will show later. In the meantime, another gauge invariant quantity constructed form $\boldsymbol{\mathcal{A}}^{(n)}(\boldsymbol{k})$ is the Berry phase, which is the line integral along a closed path C in the momentum space. Take a gauge with which $\boldsymbol{\mathcal{A}}^{(n)}(\boldsymbol{k})$ is non-singular along C, the line integral along the C can be calculated:

$$\oint_C d\boldsymbol{k} \cdot \boldsymbol{\mathcal{A}}^{(n)}(\boldsymbol{k}). \tag{1.18}$$

A gauge transformation changes the line integral as:

$$\oint_C d\boldsymbol{k} \cdot \boldsymbol{\mathcal{A}}^{(n)}(\boldsymbol{k}) \to \oint_C d\boldsymbol{k} \cdot \boldsymbol{\mathcal{A}}^{(n)}(\boldsymbol{k}) - \oint_C d\boldsymbol{k} \cdot \partial_k \phi_n(\boldsymbol{k}). \tag{1.19}$$

Since we are choosing a unique $e^{i\phi_n(\boldsymbol{k})}$ on C, the second integral in the right hand side must give $2\pi N$ with an integer N. Then the expression

$$exp[i \oint_C d\boldsymbol{k} \cdot \boldsymbol{\mathcal{A}}^{(n)}(\boldsymbol{k})] \tag{1.20}$$

is gauge-invariant. The phase factor of this quantity is the Berry phase. Later I will discuss how the Berry phase can be quantized and give a topological invariant when a certain symmetry is imposed with a suitable C.

1.2.2 Chern Number

For a 2D system, the Chern number of the nth band is defined with the field strength of the Berry connection:

$$C_n = \frac{1}{2\pi} \int_{2dBZ} dk_x dk_y \mathcal{F}_{xy}^{(n)}(\boldsymbol{k}). \tag{1.21}$$

Here, the integration is done on the occupied states in 2D Brillouin zone. Due to the periodicity of the Brillouin zone, the integral vanishes if the Berry connection $\boldsymbol{\mathcal{A}}^{(n)}(\boldsymbol{k})$ has no singularity over the Brillouin zone. If it does have a singularity at $\boldsymbol{k}_0$, and with some gauge function $\partial \boldsymbol{k} \phi_n(\boldsymbol{k})$, one can include $\boldsymbol{k}_0$ so that the new Berry connection has no singularity in the new region. The integral can then be written from the gauge function,

$$C_n = \frac{1}{2\pi} \int_{\partial R} dk \cdot \partial \boldsymbol{k} \phi_n(\boldsymbol{k}), \tag{1.22}$$

where ∂R is the boundary of the region that does not have singularity. C_n will have to be an integer number since $e^{i\phi_n(\boldsymbol{k})}$ is a unique function on ∂R. Connected with Hall conductance, one can see the importance of total Chern number of the occupied bands for a 2D insulator, due to the relationship

$$\sigma_{xy} = -\frac{e^2}{h} C. \tag{1.23}$$

Under time-reversal symmetry, the Berry connection of the occupied bands will be even and the field strength will be odd, the total Chern number of the occupied bands will obey

$$C = \frac{1}{2\pi} \int_{2dBZ} dk_x dk_y \sum_{E_n < E_F} \mathcal{F}_{xy}(\boldsymbol{k}) = -\frac{1}{2\pi} \int_{2dBZ} dk_x dk_y \sum_{E_n < E_F} \mathcal{F}_{xy}(-\boldsymbol{k}) = -C, \tag{1.24}$$

Which will lead to a zero Chern number under time reversal symmetry.

In a QAHE system, Hamiltonian can be written as:

$$H = v_F(-k_y\sigma_x + k_x\sigma_y) + m\sigma z = \boldsymbol{R}\cdot\sigma \tag{1.25}$$

when assuming magnetization along lattice z. Here $\boldsymbol{R} = (-v_F k_y, v_F k_x, m)$. Since TRS is broken by magnetism, the Chern number can be defined using $\hat{\boldsymbol{R}} = \boldsymbol{R}/|\boldsymbol{R}|$ as

$$C = 2\int_{BZ} \hat{\boldsymbol{R}}\cdot(\frac{\partial\hat{\boldsymbol{R}}}{\partial k_x}\times\frac{\partial\hat{\boldsymbol{R}}}{\partial k_y})\frac{dk_x dk_y}{4\pi} = sgn(m) \tag{1.26}$$

The 2 in the above equation comes from the top and bottom surfaces, the integration gives a winding number of one-half for the spin texture. The Chern number is thus 1, and it has a sign that depends on the sign of the exchange coupling and on the magnetization direction. When E_F is located within the mass gap, the Hall conductivity is quantized.

1.2.3 $\mathbb{Z}_2$ invariant and topological insulator

A 3D topological insulator that realizes QHE can be described by four $\mathbb{Z}_2$ invariant $(v_0; v_1, v_2, v_3)$, where v_0 is the strong topological invariant and the rest are the weak topological invariants. If $v_0 = 0$, but $v_1 + v_2 + v_3 \neq 0$, then the system is in weak topological state, where protected surface states only exist on certain surface edges. If $v_0 = 1$, the system is a strong topological insulator where all surface states are topologically protected. Otherwise, the system is trivial as a trivial band insulator.

There are several ways to define $\mathbb{Z}_2$. One way is to define $\mathbb{Z}_2$ index in the form of a Pfaffian [18], by defining a unitary matrix:

$$w_{mn}(\boldsymbol{k}) = \langle u_,(-\boldsymbol{k})|\,\Theta\,|u_m(-\boldsymbol{k})\rangle\,, \tag{1.27}$$

where $u_m(-\boldsymbol{k})$ is some Block function, $\Theta = exp(i\pi S_y/\hbar)K$ is the TR. One would expect

$$\omega^T(\boldsymbol{k}) = -\omega(-\boldsymbol{k}) \tag{1.28}$$

at some high symmetry points Γ_a in the Brillouin zone. These points are called TR invariant momentum (TRIM) points and there are 4 and 8 of them in 2D and 3D Brillouin zone. One

can define

$$\delta_a = Pf[\omega(\Gamma_a)]/\sqrt{Det[\omega(\Gamma_a)]} = \pm 1 \tag{1.29}$$

because the determinant of an antisymmetric matrix is the square of its Pfaffinan. The branch of the square root can be specified globally if $u_m(\boldsymbol{k})$ is chosen to be globally continuous in the Brillouin zone. The $\mathbb{Z}_2$ invariant is thus

$$(-1)^{\nu} = \prod_{a=1}^{4 \text{ or } 8} \delta_a. \tag{1.30}$$

In the presence of inversion symmetry, the Bloch states at the TRIM points $w(\Gamma_a)$ are also parity eigenstates with eigenvalues $\xi_m(\Gamma_a) = \pm 1$. Therefore, the process above can be simplified [19]. For each TRIM point one can calculate

$$\delta_a = \prod_m \xi_m(\Gamma_a) \tag{1.31}$$

Here the product is over Kramer's pairs of occupied bands. Thus we can derive

$$(-1)^{\nu} = \prod_{a=1}^{4 \text{ or } 8} \prod_m \xi_m(\Gamma_a). \tag{1.32}$$

One may note that 3D topological insulator has in total four Z_4 invariant. The formulation above describes the strong invariant ν_0. For three weak topological invariant, they can be calculated as Pfaffian over selected four TRIM points

$$(-1)^{\nu_{i=1,2,3}} = \prod_{n_i=1; n_{j\neq i}=0,1} \delta_a \tag{1.33}$$

where $\Gamma_a = \sum_{i=1,2,3} n_i \boldsymbol{b}_i$ marks the location of TRIM points in Brillouin zone and $\boldsymbol{b}_i$ is the primitive reciprocal lattice vectors.

Another way of defining the $\mathbb{Z}_2$ invariant is by using a concept of the spin Chern number $C_\uparrow$ ($C_\downarrow$), which is defined as the Chern number of $H_\uparrow(\boldsymbol{k})$ ($H_\downarrow(\boldsymbol{k})$). In a spin-orbit system, the Chern number is not well-defined since spin conservation is broken, but in the presence of time-reversal symmetry, one can derive an analogous topological number for a spin-orbit coupled system in 2D. Consider a Kramers pairs ($\left\langle u_n^I(\boldsymbol{k})\right| . \left\langle u^I I_n(\boldsymbol{k})\right|$), we can introduce the Chern numbers in those subspaces as C_I and C_{II}. These Chern numbers are not well defined

because in Kramers pairs, the superscripts I and II do not have any physical meaning, but the constraint of $C_I = -C_{II}$ will always hold. As a result, we have a well defined $\mathbb{Z}_2$ index

$$(-1)^{v_{2d}} = (-1)^{C_I} = (-1)^{C_{II}}. \tag{1.34}$$

The $\mathbb{Z}_2$ indices in three dimensions can also be introduced by using the time-reversal invariance.

1.2.4 Majorana Fermion

When band topology is combined with superconductivity, a new class of materials called topological superconductors can form. These are exotic materials that have both bulk superconductivity and nontrivial band topology. This leads to the emergence of gapless surface states that host Majorana fermions. A Majorana fermion is a quasiparticle that is its own antiparticle. Mathematically, the superconductor imposes electron hole symmetry on the quasiparticle excitations, thus binding Majorana fermions to a defect at zero energy. The combined objects are called Majorana bound states or Majorana zero mode (MZM). They can be realized as the superconducting vortices on the surface of a 3D TI coated with a thin s-wave superconductor. A QAH or QH system in proximity with s-wave superconductors can also host MZMs on the ends of the 1D conducting edge. The search for Majorana bound state has pushed the material exploration of topological superconductors.

1.3 Magnetism

One of the focuses of this dissertation is the magnetic properties of topological materials. I will briefly introduce the concept of magnetic orders, different types of magnetic interactions as well as their significance in experimental measurements.

1.3.1 Magnetic orders

Different magnetic orders can be distinguished by observing the response of the material to an external field, or by measuring the magnetization, χ:

$$M = \chi H. \tag{1.35}$$

Here, M is the material's magnetization and H is the external field. The magnetism is induced by the spin of unpaired electrons in metals. When a material is at high temperature, or above its ordering temperature, thermal fluctuation will uncouple the spins so they point in random directions, resulting in paramagnetism (PM). When the material is below its ordering temperature, it will show spontaneous alignments of unpaired electrons due to exchange interactions between spins.

I will focus on two unique magnetic orders now, which are ferromagnetic (FM) and anti-ferromagnetic (AFM). In the former, all the spins align parallel in the same direction leading to net magnetization, while in the latter, the spins order anti-parallel with each other, leading to zero net magnetization. To distinguish between them, one can measure the magnetization dependence on temperature or on external field. Physical properties such as saturation field, saturation moment or effective moment that can be obtained from magnetization measurements will provide important information for us to understand the magnetic order in materials.

The reason that a certain material chooses a certain magnetic order over another will largely depend on different magnetic interactions mentioned below. Overall, the order with the lowest energy will be favored.

1.3.2 Magnetic exchange interaction

A classical dipole-dipole interaction between two moments m_1 and m_2 can be written as

$$E = \frac{mu_0}{e\pi r^3}[\boldsymbol{m_1} \cdot \boldsymbol{m_2} - \frac{3}{r^2}(\boldsymbol{m_1} \cdot \boldsymbol{r})(\boldsymbol{m_2} \cdot r)]. \tag{1.36}$$

In solid-state system, magnetic exchange interaction from a quantum mechanical origin tends to dominate. According to Pauli's exclusion principles, electrons with the same spins experience different repulsion than those with opposite spins. This relationship can be expressed by Hamiltonian,

$$H = -\sum_{i,j} J\boldsymbol{S_i} \cdot \boldsymbol{S_j}. \tag{1.37}$$

When J is positive, the interaction favors the FM order, and when J is negative, the system will tend to be in AFM state.

When the exchange interaction happens between two nearest-neighboring magnetic atoms, it is named direct exchange. When it is over a long range through intermediate atoms, it is called a superexchange.

1.3.3 Magnetic anisotropy

When considering the crystal environment of a magnetic atom, there will be a energetically preferable direction for the moment to align. This is called magnetic anisotropy, which also contributes to the total Hamiltonian. The preferred orientation can be an axis or a plane, leading to easy axis/plane magnetic anisotropy. The magnetic anisotropy energy can have the following phenomenological expression:

$$H = K\sin^2(\theta) = K\boldsymbol{S}_z^2. \tag{1.38}$$

Here θ represents the angle between the spin and the easy axis, and the second expression shows the relationship of the energy term with the z direction. When $K > 0$, the system would prefers a easy axis that is perpendicular to z, thus leading to an easy plane anisotropy. When $K < 0$, the system has an easy z axis.

The major contribution to the anisotropy energy mentioned above comes from the crystal environment, or the magnetocrystalline anisotropy. This results from the coupling between the electron orbit of the magnetic atom and the crystal electric field. Other factors such as shape, stress or exchange interaction can also contribute to the magnetic anisotropy.

1.3.4 Zeeman energy

When a spin is placed in an external field, Zeeman energy tries to align the moment with the field. It is expressed as

$$H_Z = g\mu_B \boldsymbol{H} \cdot \boldsymbol{S}. \tag{1.39}$$

At high field, H_Z will dominate the Hamiontonian and all the spins will align with external field.

1.3.5 Stoner-Wohlfarth model

Developed by Edmund Stoner and Erich Wohlfarth, the Stonor-Wohlfarth (SW) model [20] is used to describe the magnetic behavior of randomly oriented magnets. It can be adapted to a single domain ferromagnet. The total Hamiltonian under an external field will contain the Zeeman and anisotropy term and can be expressed as

$$E(\theta_1) = KS^2 \sin^2(\theta_1) + g\mu_B HS\cos(\theta_1 - \theta_0). \tag{1.40}$$

Here θ_0 is the external field direction with respect to z axis and θ_1 is the moment direction with respect to z axis. By calculating $\partial E/\partial\theta_1 = 0$, or the local energy minimum, we can obtain the moments configuration at each field. This model can help explain the magnetic hysteresis and the relationship between the saturation field and easy/hard axis in magnetic anisotropy.

A similar approach can be used for a simple AFM system. Using A-type AFM structure in $MnBi_2Te_4$ as an example, the magnetic structure can be simplified as a two sub-lattice AFM. The SW model can be adjusted by adding the interlayer exchange coupling term $J_c \boldsymbol{S}_i \boldsymbol{S}_{i+1}$. Considering two layers each having an angle of θ_1 and θ_2 with the easy axis z, the energy can be expressed as:

$$E(\theta_1, \theta_2) = J_c S^2 \cos(\theta_1 - \theta_2) + K_1 S^2(\sin^2\theta_1 + \sin^2\theta_2) = g\mu_B HS(\cos(\theta_1 - \theta_0) + \cos(\theta_2 - \theta_0)). \tag{1.41}$$

One might notice that J_c and K are competing terms since the former tends to align spins opposite to each other while the latter prefers the moment to stay along the easy axis. When

an external field is applied to the system, it can transform from AFM state to a canted AFM state through a spin-flop transition and then to a FM state when the spins reach saturation.

1.4 Superconductivity

In this section, I will provide a basic introduction to superconductivity, discuss unique behaviors in superconductors such as vortex behavior, and its potential competing order the charge density waves.

1.4.1 Macroscopic interpretations

Superconductivity was first discovered when a Hg sample abruptly showed zero resistivity at 4.2 K. After that, a number of compounds were found to become superconducting under a critical temperature T_c. Other than the unusual zero resistivity, superconducting materials also show a complete repulsion of magnetic flux, known as Meissner effect. Classical electrodynamic equations were developed by Heinz and Fritz London, known as the London equations, which describe superconducting phenomena on a macroscopic scale.

The first London equation describes a perfect conductor,

$$\boldsymbol{E} = \frac{\partial}{\partial t}(\frac{m}{n_s e^2}\boldsymbol{J}_s) = \frac{\partial}{\partial t}(\Lambda \boldsymbol{J}_s), \tag{1.42}$$

in which $\boldsymbol{J}_s$ is the superconducting current density, m is the electron mass and n_s is the number of density of superconducting carriers. This equation replaces Ohm's law for a conductor that has no resistance. It describes a dissipationless acceleration under the applied electric field. The second London equation describes the relationship between the magnetic field and the superconducting current density:

$$\boldsymbol{\nabla} \times \boldsymbol{J}_s = -\frac{\boldsymbol{B}}{\Lambda}. \tag{1.43}$$

This could be rewritten as

$$\nabla^2 \boldsymbol{B} = \frac{\mu_0 n_s e^2}{m}\boldsymbol{B} = \frac{1}{\lambda^2}\boldsymbol{B} \tag{1.44}$$

by applying Ampere's law. The solution of this equation shows an exponential decay within a superconductor and the characteristic length λ is known as the penetration depth.

Another important quantity to characterize superconductivity is the coherence length ξ. It describes the length over which two electrons interacted with each other:

$$\xi_0 = a\frac{\hbar v_f}{k_B T_c}, \tag{1.45}$$

in which a is the proportional constant and v_F is the Fermi velocity. The relationship between the penetration depth λ and coherence length ξ can be used to determine the nature of the superconducting system. A dimensionless parameter κ was introduced by Ginzburg and Landau as $\kappa = \lambda/\xi$, which is independent of temperature. When $\kappa < 1/\sqrt{2}$. the material is a type I superconductor, and when $\kappa > 1/\sqrt{2}$, the material is a type II superconductor.

A Type I superconductor completely expels the magnetic field and has only one critical magnetic field (H_c), above which superconductivity is destroyed. Most pure elemental superconductors lie in this category. A Type II superconductor allows the magnetic field to penetrate in a quantized form through vortices, while remaining in the superconducting state. It has two critical fields, H_{c1} and H_{c2}, between which it exhibits a mixed state.

1.4.2 Microscopic picture

Superconductivity can be explained by the Bardeen-Cooper-Shrieffer (BCS) theory. Multiple unconventional phenomena can be well explained by the theory, such as evidence of a superconducting band gap at Fermi level, the isotope effect suggesting lattice interaction and an exponential rise in heat capacity near the critical temperature for some superconductors. The theory pointed out that superconductivity arises when Cooper pair forms due to the attractive interaction between electrons in a solid. In conventional superconductors, Cooper pair forms due to the electron-phonon interaction, which has the following wavefunction:

$$\Psi(\boldsymbol{r}_1, \boldsymbol{r}_2, \sigma_1, \sigma_2) = \psi(\boldsymbol{r}_1 - \boldsymbol{r}_2)\phi(\sigma_1, \sigma_2). \tag{1.46}$$

with the ψ as the spatial part of the wavefunction and ϕ the spin part. Cooper pairs with orbital angular momentum $l = 0, 1, 2, 3$ are called s-wave, p-wave, d-wave, and f-wave,

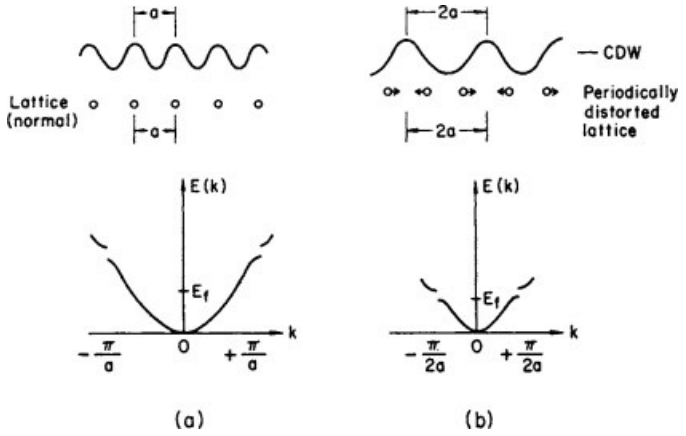

Figure 1.5: Comparison between normal state and charge density wave state of material in terms of real space and band structure. (a) shows the normal state with evenly spaced atoms and electron density with a periodicity of a. Gaps open at the edge of Brillouin zone at $\pm\pi/a$. (b) depictes a distortion of lattice and electron with a periodicity at $2a$. Additional gaps open at $\pm\pi/2a$. Figures are adapted from Ref. [21].

respectively. Since the Cooper pair is formed by pairing two spin-1/2 electrons, the spin angular momentum of a pair is either 0 (spin-singlet) or 1 (spin-triplet). The former has an antisymmetric ϕ in the spin space, while the latter has a symmetric ϕ. Therefore, to make Ψ antisymmetric, for spin-triplet SC, ψ should be antisymmetric (odd-parity, like p-wave) while for spin-singlet SC, ψ should be symmetric (even parity such as s-wave and d-wave).

1.4.3 Charge density wave

The concept of the charge density wave (CDW) was first introduced by Peierls at 1930 [21]. He proposed that when electron instability arises by electron phonon interaction, periodicity in electron density can form and cause an energy gap to open, as shown in Fig. 1.5. The concept is that when the energy 'cost' to distort the lattice is less than the energy 'release' when the gap opens, the system will prefer the CDW state. The reason that CDW frequently serves as the competing phase of superconductivity is that both are closely related to electron-phonon interaction and if realized in the same material, could compete for the same electrons at the Fermi level.

1.5 Introduction to Magnetic topological insulators $MnBi_{2n}Te_{3n+1}$

Since the discovery of TI in the 2000s, predictions have been made regarding novel topological states when other physical aspects are accompanied with the band topology. When TI is combined with magnetism, exotic states such as axion insulators, magnetic Weyl semimetals, Chern insulators and 3D QAH insulators are proposed [3]. These phenomena provide future opportunities for applications in low-energy-dissipate devices, quantum metrology and quantum computing [22]. As mentioned in the previous sections, QAHE was first achieved in an MBE grown Cr-doped $(Bi/Sb)_2Te_3$ thin film at an extremely low temperature of 30 mK [6]. Due to the limitations of very low temperature as well as defects from chemical doping, it remains a material challenge to realize QAHE at elevated temperatures. This led to the development of $MnBi_2Te_4$, an intrinsic magnetic topological insulator that has both magnetism and nontrivial topological band structure. In this section, I will introduce the recent progress on this compound, including the motivations for the work related to my thesis work.

1.5.1 The first intrinsic AFM TI $MnBi_2Te_4$

As the first intrinsic magnetic topological insulator, $MnBi_2Te_4$ has been extensively studied both experimentally and theoretically. Mn layers in $MnBi_2Te_4$ ordered into A-type AFM below 24 K, in which the Mn atoms in the same layer are FM coupled with moments pointing perpendicular with the plane, while Mn between neighboring layers are AFM coupled. This magnetic structure has been confirmed by transport, magnetization and neutron diffraction studies.

A nontrivial topological band structure is realized by the inversion of band between Bi $6p$ and Te $5p$ orbitals with strong spin-orbit coupling. Under the A-type AFM, the (00L) surface is gapped due to the symmetry breaking, leaving a 1D edge state shown in the DFT calculation. ARPES measurements have successfully observed a large bulk gap and gapless Dirac surface states. Device fabrication has yielded fruitful result due to the Van der

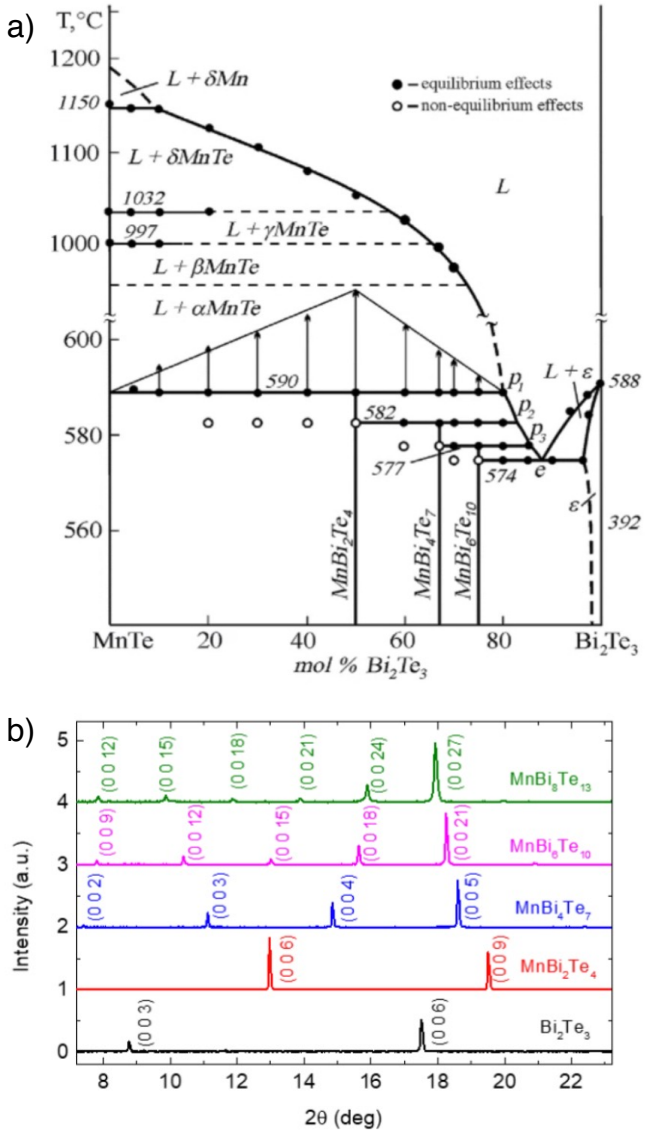

Figure 1.6: Growth and characterization of $MnBi_{2n}Te_{3n+1}$. (a) Phase diagrm of the quasi-binary MnTe-Bi_2Te_3, in which small growth window for compounds can be seen, taken from [23]. (b) XRD data for (00l) surface for $MnBi_{2n}Te_{3n+1}$ family.

Waal nature of $MnBi_2Te_4$. When fabricated into odd-layer device, $MnBi_2Te_4$ contains a net magnetism that helps realize QAHE [24]; even-layer devices host emergent phenomena such as layer Hall effect or quantum metric nonlinear Hall effect [25, 26].

1.5.2 Natural Heterostructures

$MnBi_2Te_4$ belongs to the larger family of XBi_2Te_4, where X can also be nonmagnetic Ge, Sn and Pb. All of these compounds have been well studied in the past as thermometric materials. After Bi_2Te_3 was found to be a TI, their topological properties also started drawing attention [27]. The great structural compatibility makes various heterostructures possible, leading to two major advantages. First, by inserting Bi_2Te_3 between $MnBi_2Te_4$ layers to create $MnBi_{2n}Te_{3n+1}$ ($n \leq 4$), one can increase the Mn-Mn interlayer distance and effectively change the magnetic interactions in the system. Also, the great structural compatibility allows the insertion of MnTe layers into the system creating possible combinations such as $Mn_2Bi_2Te_5$ and $Mn_3Bi_2Te_6$ which are also proposed to be MTIs. Second, these heterostructures can be exfoliated into various combinations of $[Bi_2Te_3]$ and $[MnBi_2Te_4]$, enabling the realization of different topological states such as the Quantum Anomalous Hall (QAH) state and the Quantum Spin Hall (QSH) state, as well as various emerging phenomena associated with axion physics.

1.5.3 Growth and Characterization

Over the last few years, single crystals of the $MnBi_{2n}Te_{3n+1}$ family have been successfully grown up to $n = 4$ [31–33]. These materials contain a $MnBi_2Te_4$ layer that constructed from a monolayer of $MnTe_6$ octahedra sandwiched by two edge-sharing layers of $BiTe_6$. The Bi_2Te_3 layer inserted between is simply two edge-sharing $BiTe_6$ layers stacked together. The distance between the nearest layer is increases with respect to n and shown in Table 1.1.

The single crystal $MnBi_{2n}Te_{3n+1}$ can be made by self-flux using Bi_2Te_3 as the flux. Fig. 1.6 (a) shows the phase diagram for the mix of MnTe and Bi_2Te_3. Experimentally, a ratio between MnTe and flux, or MnTe : $Bi_2Te_3 = x$: 100-x with $10 \leq x \leq 20$ can give the best

Table 1.1: Summary of the chemical, structural, magnetic properties of $MnBi_{2n}Te_{3n+1}$ from $n = 1$ to 4. Here, T_{growth} means the temperature that the growth was finished and flux was spun out. Table adapted from Ref. [28].

	$MnBi_2Te_4$	$MnBi_4Te_7$	$MnBi_6Te_{10}$	$MnBi_8Te_{13}$
n	1	2	3	4
Space Group	R-3m	Pc-3c	R-3m	R-3m
Magnetic Space Group	R_I-3c	Pc-3c1	R_I-3c	R-3m'
Lattice constant a (Å)	4.3336(2) [29]	4.3453(5) [29]	4.361 [30]	4.3749(1) [31]
Lattice constant c (Å)	40.926(3) [29]	23.705(3) [29]	101.300 [30]	132.415(3) [31]
d_{Mn-Mn} (Å)	13.642(1)	23.705(3)	33.995(1)	44.138(1)
Mn : Bi : Te (WDS)	0.90:2.11:4	0.79(2):4.29(8):7	0.79(1):6.30(2):10	0.74(3):8.2(1):13
T_{growth} (°C)	587	585	583	582
Magnetism	AFM	AFM	AFM	FM
T_N/T_C (K)	24	13	11	10.5
SJ_c (meV/Mn)	0.25	0.0086	0.0031	-
SD (meV/Mn)	0.08	0.098	0.098	-

result. The detailed flux growth method will be introduced in the later section, but I would like to emphasize that the most crucial component of the growth is the decanting temperature at which the crystals and flux are separated. The optimal growth temperature, T_{growth} is summarized in Table. 1.1. In general, $MnBi_2Te_4$ has the largest growth temperature window, approximately 4 °C around T_{growth}. For higher n, the growth window decreases, and is only about 1 °C for $n = 4$. Due to the natural temperature gradient in box furnaces, growth aimed for $MnBi_8Te_{13}$ usually produces a mixture of different phases, and careful screening of single-phased pieces is essential during the experimental process.

To determine the phase of single crystals from the growth, we measured X-ray diffraction on their flat (00L) surfaces. Since different n (from 0 to 4) member has very quite different lattice parameter c, their (00L) Bragg reflections are completely different. A comparison between these diffraction patterns is shown in Fig. 1.6 (b). To ensure the phase purity of a selected piece, a portion of the sample is cut and ground into powder. Then, powder X-ray diffraction is used to determine the presence of any embedded impurities and to analyze the detailed crystal structure.

1.5.4 Magnetic and Transport Properties

The magnetism structure, temperature dependent magnetic susceptibility and isothermal magnetization are summarized in Fig. 1.7. The magnetic ordering temperature decreases from 24 K for $MnBi_2Te_4$ to 10 K for $MnBi_8Te_{13}$, with Mn ordering into AFM for $n = 1, 2$ and 3 and FM when $n = 4$. The evolution of magnetism under external field can be captured by the Hamiltonian for the magnetic ground state, written as

$$\begin{aligned} E = &- \sum_{ii'} J_1 S_i \cdot S_{i'} - \sum_{ii'} J_2 S_i \cdot S_{i'} - \sum_{ij} J_c S_i \cdot S_j - \sum_i D {S_{iz}}^2 \\ &- \sum_i g\mu_B \mathbf{H} \cdot \mathbf{S}_{i,z} \end{aligned} \tag{1.47}$$

The terms include FM intraplaner exchange coupling J_1 and J_2, weak nearest neighbor (NN) interplaner coupling J_c, magnetic anisotropy D and Zeeman energy as the last term. Both

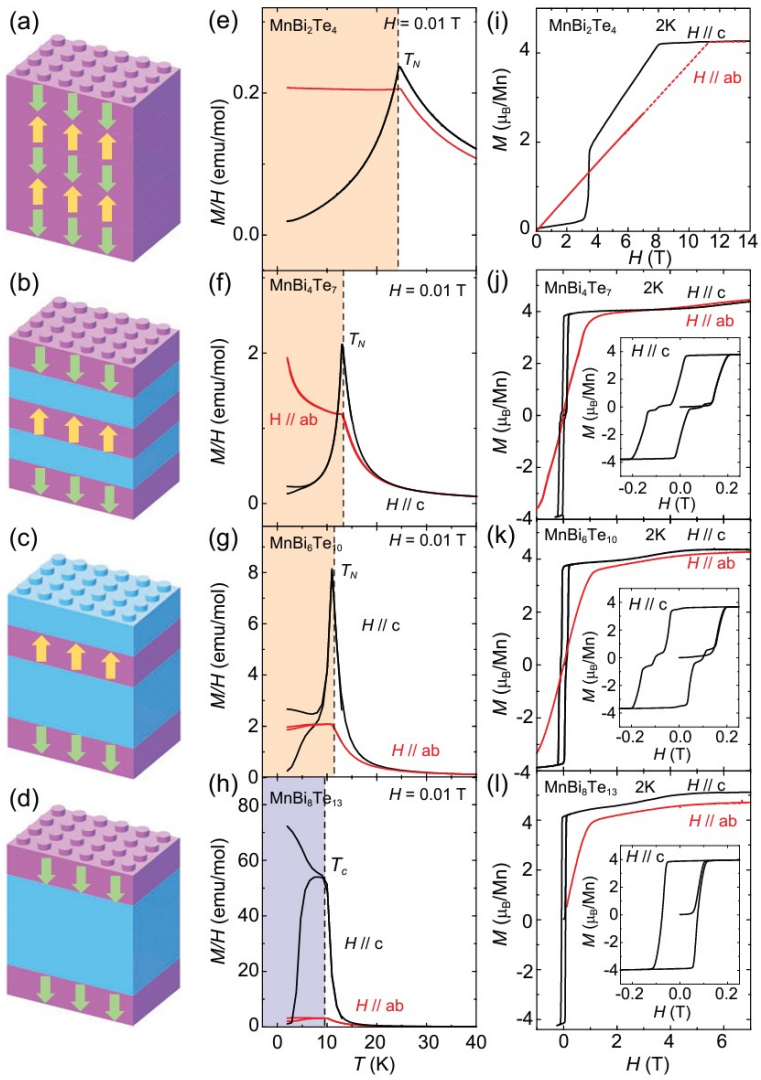

Figure 1.7: Evolution of magnetism in $MnBi_{2n}Te_{3n+1}$. (a-d): Magnetic structure for single crystal $MnBi_2Te_4$, $MnBi_4Te_7$, $MnBi_6Te_{10}$ and $MnBi_8Te_{13}$, respectively. (e-h): The temperature-dependent magnetic susceptibility measured with in-plane and out-of-plane magnetic fields. (i-l): Isothermal magnetization under in-plane and out-of-plane fields at 2 K. Insets of (j-l): The magnetization hysteresis loop near zero field. This figure is taken from Ref. [28].

SD and SJ_c can be estimated by applying the bilayer Stoner-Wohlfarth model as follows:

$$|SD| = (H_s^{//ab} - H_s^{//c})(g\mu_B/4) \tag{1.48}$$

$$|SJ_c| = (H_s^{//ab} + H_s^{//c})(g\mu_B/4z). \tag{1.49}$$

Here $H_s^{//ab}$ denotes the saturation field with $H//ab$. Also, one can estimate the spin gap as $\Delta = 2SD\sqrt{zSJ_c/SD+1}$. The evolution of SD and SJ_c is summarized in Table. 1.1. A decrease in SJ_c can be explained by the increase in distance between Mn layers and a small change in SK shows an almost unchanged lattice environment.

1.5.5 Antisites and Doping

The naturally grown $MnBi_{2n}Te_{3n+1}$ is heavily electron doped. The charge neutrality point of 0.24-0.4eV below the Fermi level is obtained from ARPES. This value is much larger than the bulk or surface gap, leading to difficulties in measuring topological features from the bulk. The main reason for this intrinsic electron doping in the as-grown sample is the existence of antisites and vacancies.

When Mn atoms enter Bi sites, it is denoted as Mn_{Bi}, and when Bi atoms mix into Mn sites, it is written as Bi_{Mn}. For naturally grown $MnBi_2Te_4$ from flux method, Bi_{Mn} is 18% while Mn_{Bi} is only around 1-4%. Since Bi_{Mn} is an electron donor and Mn_{Bi} accepts electron, the system becomes heavily electron doped. Additionally, chemical analysis and neutron diffraction refinement have shown the existence of Mn vacancies, which add more electrons to the as-grown crystal.

In order to tune the carrier concentration, and thus control the Fermi level, doping studies has been performed aiming to reduce the antisite disorders. When doping Sb into $MnBi_2Te_4$ [34], the charge neutrality point can be reached when Bi is replaced by Sb, but the study of the magnetic ground state points to different results from different literature [34–36]. This was later found to be caused by an uncertainty in the amount of Sb_{Mn} and Mn_{Sb} due to slightly different growth profiles in terms of temperature, starting material and growth method.

When n goes higher, there will be more sites where Mn can reside. The main site where Mn naturally exists is written as Mn1 and the Bi site in $MnBi_2Te_4$ is written as Mn2. For higher n compound, the Bi sites in the Bi_2Te_3 layers are noted as Mn3 and so on. The Sb doped $MnBi_4Te_7$ will be further discussed in the later chapter, and the effort to make a doped series without introducing more antisites for this system will also be covered.

CHAPTER 2

Experimental Techniques

2.1 Material Growth

Compared to powder samples, sizable high-quality single crystals offer many advantages in research. For example, they usually contain fewer impurities and chemical disorders which are less likely to obscure the intrinsic properties of the material. A single crystal comes with well-defined surfaces or edges, which allows the surface sensitive measurements such as scanning tunneling microscopy and angle-resolved photoemission spectroscopy, which demand ultra-clean surfaces. A well defined crystal surface can also help to determine the orientation of the crystal, thus making it feasible to perform orientation sensitive characterizations such as magnetic anisotropy or angle-dependent transport measurements.

Three major methods of single crystal growth are used nowadays, the growth from congruent melt, the high-temperature flux growth and the chemical vapor transport. In my thesis work, I have employed the latter two methods, so I will introduce these two with details in the following section.

2.1.1 High-temperature Flux Growth

High-temperature flux growth is the most widely used method in growing single crystals during scientific explorations due to its low cost and fast turnaround time. The "flux" refers to the solvent that can bring the solution containing the constituent elements of the target material into a liquid phase at temperatures well below their individual melting points, promoting single crystal growth under more accessible experiment conditions. The flux is

usually an element with low melting point and low vapor pressure such as Sn, Bi, Sb and Te, etc. Sometimes, the flux can also be binary compounds, for example, in the growth of $MnBi_{2n}Te_{3n+1}$, Bi_2Te_3 is used as the self flux. The principle of the growth is that nucleation and precipitation of the desired phase can occur in a supersaturated solution.

To prepare the growth, elements are carefully weighed according to predetermined recipe, which includes the ratio between the composition of the target material and flux. This ratio may vary and improve over more growth trials. The mixture of raw materials is first loaded into an alumina crucible and then sealed under vacuum or under 1/3 atm of Ar gas in a quartz tube. Within this growth ampule, quartz wool is placed at both the top and bottom of the alumina crucible. The bottom quartz wool acts as a support of the crucible while the top one serves as a filter to separate the single crystals from the solution. The sealed ampule is then placed inside a box furnace and heat up to a high enough temperature T_1 so that the materials enter the liquid phase and stay there for a few hours to ensure good homogeneity. Then the temperature goes through a strictly controlled slow cooling process. This cooling process takes the solution into the supersaturated state where nucleation and precipitation of the desired phase can happen, resulting in the formation of sizable single crystals. Finally, at the so-called decanting temperature T_d, the growth ampule is quickly inverted and moved to a centrifuge. A large centrifugal acceleration of nearly 1000g will then spin out most of the liquid, while the single crystals are blocked by the quartz wool and remain inside the alumina crucible. Here, the selection of flux, the ratio in the recipe, T_1, T_d as well as the ramp rate of the slow cool procedure are important parameters to affect the result of the growth.

The flux growth method has certain limitations. For example, even if a flux is a good solvent for the constituent elements of a target material, there is no guarantee that the target material will precipitate into single crystal form during the cooling process. Additionally, single crystals grown using the flux method inevitably contain embedded flux. Therefore, it is necessary to carefully examine whether the experimental observations are intrinsic or arises from the flux. This is especially important when zero resistivity is observed.

2.1.2 Chemical Vapor Transport Growth

Compared to the flux growth method, single crystals made by the chemical vapor transport method are usually purer and have fewer disorders. This method is widely used to grow van der Waals (vdW) materials, likely because elements like S, Te, Se, Cl, Br and I which are frequently found in vdW materials, readily form vapors with transport agents, making the growth process occur at lab-accessible conditions.

In chemical vapor transport growth, the constituent elements of the target material form intermediate volatile vapors with the transport agent. Halogen and binary halides, such as I_2 and $TeCl_4$, are widely used transport agents. Due to the temperature gradient set along the quartz tube, these vapors slowly diffuse from one end of the sealed growth ampule at temperature T_1 (source end) to the other end at temperature T_2 (sink end) where the vapors decompose and react to form the desire material. This process can continue as long as the transport agent, materials in the source end and temperature gradient are maintained, resulting in sizable single crystals. According to Schäfer's transport equation, the transported mass is proportional to the cross section of the container, the partial pressure difference of the effective transport species, the reaction time and the average temperature, but is inversely proportional to the length of the container and the total pressure. Therefore, the success of the chemical vapor transport growths depends on the selection of the transport agent, T_1, T_2, $T_1 - T_2$, the length and radius of the quartz tube and the growth duration.

The first step of preparing a chemical vapor transport is to estimate the total inner pressure of the tube at growth temperature using the ideal gas law to avoid the breaking of growth ampule due to high pressure. For example, if using I_2 as the transport agent, it is safer to assume the amount of I_2 in the tube all become vapors in the form of I. After calculating the right amount of transport agent needed, both the starting elements and transport agent are sealed in a quartz tube under vacuum. Then this growth ampule is placed inside a furnace and slowly heated up with one end at T_1 and the other at T_2. The locations of the two ends of the quartz ampule in the furnace as well as the temperature and temperature gradient at these two ends need to be carefully examined and calibrated before the growth.

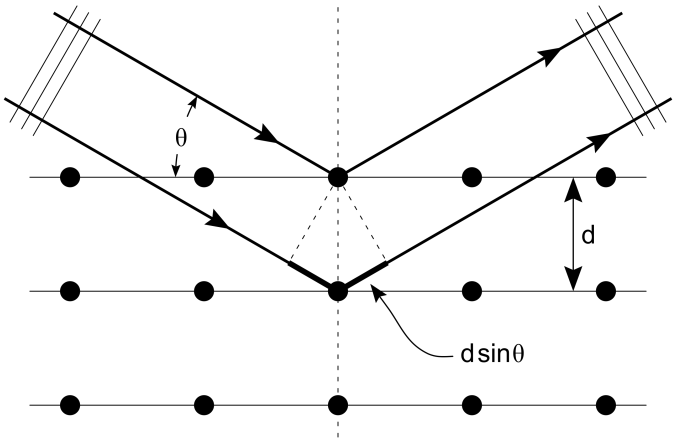

Figure 2.1: Bragg's condition for constructive interference that gives a peak in XRD pattern.

The growth process can be of days, weeks or even months, depending on the growth rate. At the end of the growth, the quartz ampule is slowly pulled out of the furnace. Ethanol followed by distilled water can usually rinse off the halide impurities on the surface.

2.2 Structure Determination and Chemical Analysis

After single crystals are obtained, several techniques are used to determine the phase, purity and chemical composition of the sample before more delicate measurements are performed. In this section I will introduce structural determination techniques of x-ray diffraction and neutron diffraction; I will also introduce energy/wavelength dispersive spectroscopy fore chemical analysis.

2.2.1 X-ray Diffraction

When X-ray is shined to a periodic crystal lattice, at certain specific wavelength λ and angle θ, constructive interference can occur, giving rise to the reflected peaks observed. This is explained by Lawrence Bragg and later known as the Bragg's law 2.1:

$$n\lambda = 2d\sin\theta. \tag{2.1}$$

n is the diffraction order and d is the length of the repeating unit in real space. After single crystals are made, surface X-ray measurement can be used to determine the orientation of each as-grown surface of the crystal while powder X-ray diffraction (PXRD) pattern of the sample can help the purity check as well as the structural determination. With the structural information of the target material, the RXRD pattern is first analyzed using HighScore Plus for phase purity check. If the phase is pure, a Rietveld refinement can be performed using the FULLPROF SUITE software to get the detailed structural information including site occupancy.

2.2.2 Neutron Diffraction

A good comparison can be made between neutron and X-ray scatterings. Both of them obey the Bragg's law when determine the lattice structure of a sample. The major difference is that neutron is a spin-1/2 fermion and photon is a spin-0 boson, so the former will interact with magnetic spins in the material as well. As a result, neutron scattering is a powerful tool to determine the magnetic structure of a sample.

Like XRD, neutron diffraction can be done on both single-crystal and powder samples. For our studies, single-crystal neutron diffraction is performed below the magnetically ordered temperature for the magnetic structure, and high temperature for the crystal structure on the HB-3A DEMAND single-crystal neutron diffractometer located at Oak Ridge National Laboratory [37]. Neutron wavelength of 1.551 Å is selected by a bent perfect Si-220 monochromator. FULLPROF SUITE software [38] is used to refine the data obtained.

2.2.3 Energy- and Wavelength- Dispersive X-ray Spectroscopy

An accurate measurement of the composition of a compound is of great importance. Particularly, for doping studies introduced in this work, it is crucial to obtain the real doping level since physical properties are compared in the unit of per Mn. Although the refinement of both XRD and neutron diffraction patterns may reliably provide information of the site occupancy and thus composition of the material, in cases where complex chemical

disorders exist or in cases where the scattering cross sections of the constituent elements are too similar, a different tool than scattering is needed to provide independent measure. Energy-dispersive X-ray spectroscopy (EDS) and wavelength dispersive X-ray spectroscopy (WDS) are used for chemical analysis of the material, determining the actual atomic ratio for samples.

When high energy electrons interact with atoms in a material, they can excite deeply localized electrons to high energy levels. The electrons then fall back to lower energy levels, causing the emission of X rays. Since each element has its unique atomic orbitals, it has its own characteristic X ray spectrum. Therefore, by analyzing the total spectrum, the types and ratio of various elements in the material can be accurately determined.

EDS measurement is performed using an energy dispersive X-ray spectroscopic analyzer (EDAX; EDAX Inc.) mounted on a scanning electron microscope (JEOL JSM 6700 F). It measures the energy of the characteristic X-ray emitted from the sample. WDS measurement is performed on a JEOL JXA-8200 Superprobe. It measures the wavelength of the characteristic X-ray emitted from the sample. Although EDS makes quicker measurements, WDS provides much higher spectral resolution, which is thus much more sensitive in detecting low-concentration elements and elements with similar X ray energies. Before the WDS measurement, the spectra of "standards" which are well-characterized samples with known concentrations are first measured, creating calibration curve. Then the intensity of the spectra of the material under investigation is compared to the calibration curves to obtain the elemental concentration in the sample.

2.3 Physical Property Measurements

The physical property measurements performed in my thesis work include electrical transport, specific heat and magnetic property measurements. These properties are measured with varying temperatures and magnetic fields. Also, they can be measured when applying uniaxial strain or hydrostatic pressure.

2.3.1 Electrical Transport Measurements

Electrical transport measurements are performed using the Quantum Design Dynacool Physical Properties Measurement System (QD Dynacool PPMS) with standard six-probe configuration. A bar-shaped sample is cut and polished with the dimension and crystal orientation well defined. Resistivity of the crystal is calculated by using $\rho_{xx} = AR/L$, where A is the cross section, R is the resistance and L is the length of the sample while the Hall resistivity is calculated by $\rho_{xy} = R_{xy}d$, where d is the thickness of the sample. Magnetotransport data are collected with field swiping from -9 T to 9 T. In order to get rid of the mixed-channel signal, the data are symmetrized to obtain $\rho_{xx}(B)$ using $\rho_{xx}(B) = \frac{\rho_{xx}(B)+\rho_{xx}(-B)}{2}$ and antisymmetrized to get $\rho_{xy}(B)$ using $\rho_{xy}(B) = \frac{\rho_{xy}(B)-\rho_{xy}(-B)}{2}$. The sign of ρ_{xy} is chosen so that hole carriers lead to positive ρ_{xy}.

2.3.2 Specific Heat Measurements

Specific Heat measurements are also performed using QD Dynacool PPMS. Samples are loaded onto a 2 mm x 2 mm platform and only several thin wires are used to hang the platform. The sample in contact with the platform needs to be flat to ensure a good thermal contact. Apiezon N grease and H grease are used to secure the sample on the platform at the temperature range below 300 K and above 300 K. Vacuum chamber is pumped to high vacuum mode less than 1 mTorr, so least thermal conductivity can apply.

A relaxation technique is used for the measurement. First a heat pulse is applied at a controlled power and time period. After the heat is turned off, it will gradually cool down to the base temperature. The temperature response on the platform T is recorded throughout the process, which follows

$$C\frac{dT}{dt} = -K_w(T - T_0) + P(t) \tag{2.2}$$

The K_w is the thermal conductance of the wires, T_0 is the base PPMS temperature and $P(t)$ is the power by the heater. Fitting of the $T - t$ curve using Eq. (2.2) allows us to obtain C, the total specific heat of both the sample and background. Therefore, two sets of

measurements are taken. The first one is called addenda measurement which measures the specific heat of the background, that is, the platform and the grease, and then a second one with the added sample. Eventually

$$C_{\text{sample}} = C_{\text{total}} - C_{\text{addenda}} \tag{2.3}$$

2.3.3 Magnetic Property Measurements

Magnetic property measurements are performed using the QD Magnetic Properties Measurement System (QD MPMS3). Samples were loaded on a quartz or straw holder with GE varnish. For temperature-dependent susceptibility measurement, two cooling modes are used, zero-field-cooled (ZFC) and field-cooled (FC). Both are taken from low temperature to high temperature under a magentic field. In the former mode, the sample was first cooled under no field before the field is switched on. In the latter case, the field is always on before and after the measurement.

2.3.4 Uniaxial Strain Measurements

Uniaxial strain strain measurements are done to modify the lattice parameter of the crystal or break crystalline symmetries. A home made three-piezostack strain apparatus is used to control the in-situ uniaxial strain applied to the sample in QD PPMS. A piece of single crystal is carefully selected and pasted with stycast across the gap on the apparatus where strain will be applied. A strain gauge is pasted on one of the piezostack to measure the actual strain applied to the sample. Calibration is done at each temperature, where the strain gauge measures ϵ_{piezo} when the voltage applied to the piezostacks varies, then the strain on the sample can be calculated as $\epsilon_{sample} = 1\frac{L}{l}\epsilon_{piezo}$. Here L is the length of the piezostack and l is the size of the gap. A more delicate simulation is done with finite element analysis to get the exact strain value on the measured portion. A schematic plot and a photo of the strain apparatus are shown in Fig. 2.2 (a) and (b).

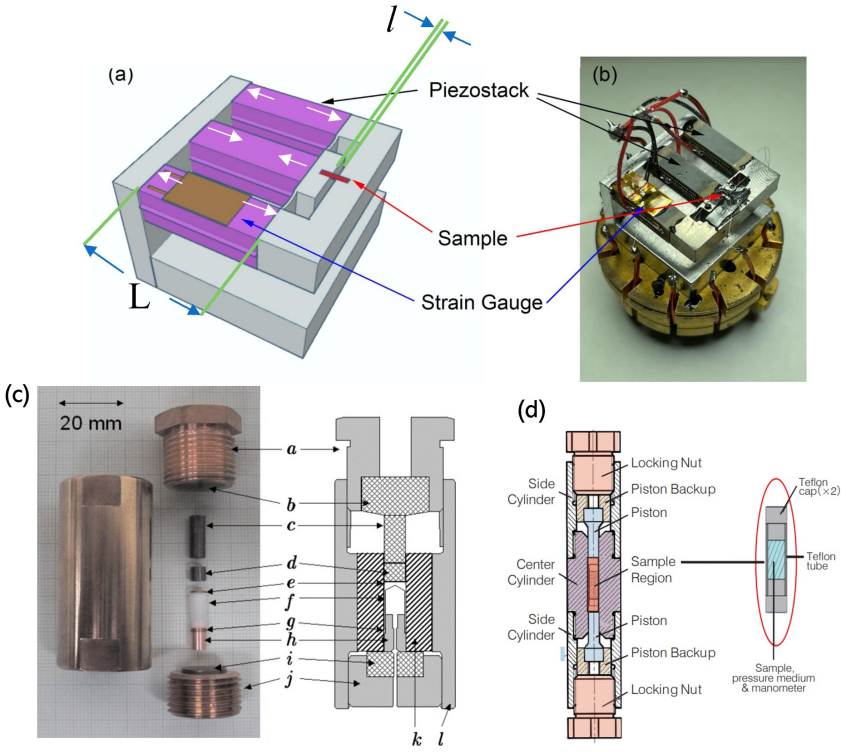

Figure 2.2: Schematic of uniaxial strain and hydrostatic pressure measurement. (a) and (b) show the home built three-piezostack strain apparatus, L and l marks the length of piezostack and width of the gap that the sample is strained. White arrows show the movement of the piezostack when tensile strain is applied to the sample. (c) and (d) show the hydrostatic pressure apparatus that measures transport and magnetization properties. The major difference is that a channel is needed at the bottom of (c) so conducting wire can be passed through to measure electric signals, while no contacts are needed for magnetization measurement.

2.3.5 Hydrostatic Pressure Measurements

For the transport properties under pressure, a C&T Factory commercial piston pressure cell compatible with a QD PPMS is used; for the magnetic properties under pressure, a HMD pressure cell compatible with a QD MPMS3 is emplyed. Daphne Oil 7373 [39] is used as the hydrostatic pressure medium. A Pb piece is used as a manometer by tracking the pressure dependence of its superconducting transition, which is described by $dT_c/dP = -0.361(5)$ K/GPa [40]. The magnetic signal from Pb is subtracted from the total magnetic signal to obtain the magnetic data of the samples. Both apparatuses are shown in Fig. 2.2 (c) and (d).

CHAPTER 3

Magnetic dilution effect and topological phase transitions in magnetic topological insulator $(Mn_{1-x}Pb_x)Bi_2Te_4$

This chapter is adapted from [41]. This work was done in collaboration with Dr. Huibo Cao's group from Oak Ridge National Laboratory on neutron diffraction measurement, Prof. Igor Mazin from George Mason University on the theoretical understanding of the magnetic dilution effect and Prof. Tay-Rong Chang from National Cheng Kung University on DFT calculation.

3.1 Introduction

Intrinsic magnetic topological insulators provide a great playground for discovering new topological states of matter such as the quantum anomalous Hall insulators, Chern insulators and axion insulators [3]. Recently, $MnBi_2Te_4$ with the van der Waals bonding was discovered to be the first example of an intrinsic antiferromagnetic (AFM) TI [42–46], which has triggered extensive theoretical and experimental studies to explore the emergent phenomena arising from the interplay of magnetism and non-trivial band topology. Soon quantum anomalous Hall effect, Chern insulator state and layer-Hall effect were realized in the two-dimensional (2D) limit of $MnBi_2Te_4$ [24, 25, 47, 48], opening up great opportunities in low-energy-consumption devices, quantum metrology and quantum computing.

$MnBi_2Te_4$ has a rhombohedral crystal structure with the stacking of Te-Bi-Te-Mn-Te-Bi-Te. The Mn^{2+} ions adopt a high-spin $S = 5/2$ state and order into the A-type AFM structure

below 24 K with spins ferromagnetically aligned in-plane and coupled antiferromagnetically along the c-axis. It is of particular interest to tune the magnetism and band topology in $MnBi_2Te_4$ so that new magnetic topological states and novel functionalities can be realized. Such tuning has been effected by three means.

One is through the structural engineering. Following this line, $MnBi_{2n}Te_{3n+1}$ ($n = 2, 3, 4$) consisting of alternating $(n-1)$ [Bi_2Te_3] quintuple layers and one [$MnBi_2Te_4$] septuple layer were synthesized [23, 29, 31, 32, 49–55]. With increasing n, the interlayer Mn-Mn distance increases and thus the AFM interlayer exchange interaction decreases. Consequently, $MnBi_2Te_4$, $MnBi_4Te_7$ and $MnBi_6Te_{10}$ are Z_2 AFM topological insulators while $MnBi_8Te_{13}$ becomes a ferromagnetic axion insulator [31]. Layered structure layout of the $MnBi_{2n}Te_{3n+1}$ is shown in Fig. 3.1.

Other ways of tuning the magnetism and band structure including external pressure and chemical doping. Pressure studies have been done to actively tune the interlayer distance of the $MnBi_{2n}Te_{3n+1}$ family [56–58], where pressure-activated metamagnetic transitions [58] were reported. In case of chemical doping studies, when Sb is doped in $MnBi_2Te_4$ [34, 59], Sb not only substitutes Bi, but also leads to complex chemical disorders. Due to the similar ionic radius between Mn^{2+} and Sb^{3+}, the amount of Mn on the Mn site (Mn1 sublattice) decreases while the amount of the $Mn_{Bi,Sb}$ antisites, that is, the amount of the Mn on the Bi/Sb site (Mn2 sublattice) increases [35, 60]. Consequently, holes are doped into the system, and the ground state becomes ferrimagnetic with decreasing saturation moment and saturation field [61,62]. Therefore, the uncontrollable and complex chemical disorders caused by Sb doping make it challenging to differentiate the effect caused by the dilution of the Mn1 sublattice and the growing of the Mn2 sublattice.

In this chapter, I will introduce how we investigate the effect of magnetic dilution of the Mn1 sublattice on the magnetism and band topology. First I will present the growth and characterization of $(Mn_{1-x}Pb_x)Bi_2Te_4$ ($0 \leq x \leq 0.82$) single crystals. Then I will show that the Mn_{Bi} antisites remain negligible and the dilution of the Mn1 sublattice leads to linearly decreasing with doping Néel temperature and saturation field. We further reveal a

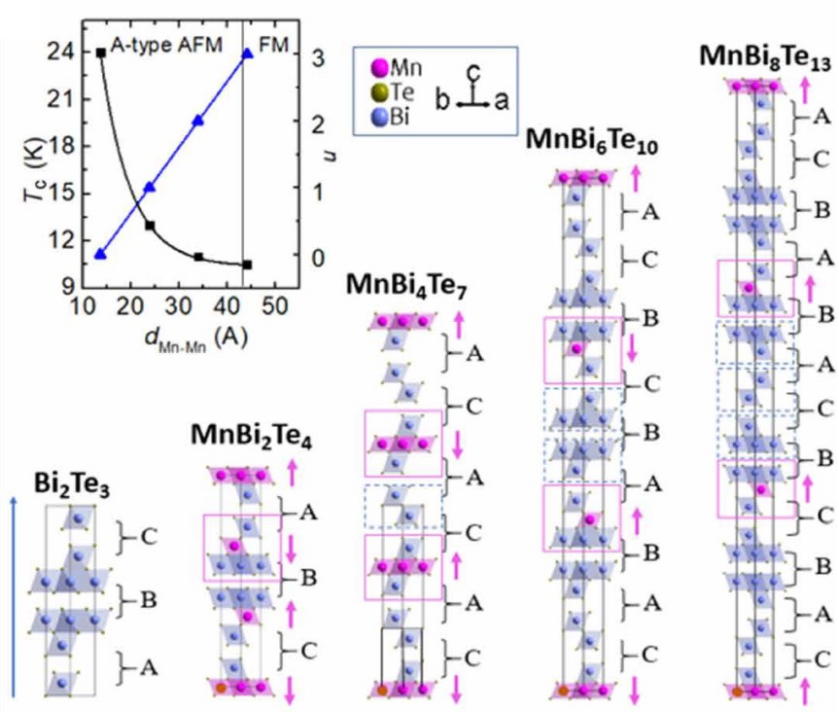

Figure 3.1: Schematic drawing of the crystal and magnetic structure of $MnBi_{2n}Te_{3n+1}$ ($n = 0, 1, 2, 3$ and 4) with the stacking sequence listed. Purple arrows indicate the spin direction for Mn atoms in different layers. Inset: Manetic ordering temperature T_c verses interlayer distance between the adjacent Mn-Mn layers d_{Mn-Mn} and n versus d_{Mn-MN}. Figures are adapted from Ref. [31].

complicated band inversion evolution upon doping, where two gapless points appear when doping concentration achieves x =0.44 and 0.66.

3.2 Obtaining $(Mn_{1-x}Pb_x)Bi_2Te_4$ single crystals

Single crystals of $(Mn_{1-x}Pb_x)Bi_2Te_4$ were grown using the self flux method [63]. Pb shots, Mn pieces, Bi and Te chunks were mixed with a ratio of $[x_{\text{nominal}}\text{Pb}+(1-x_{\text{nominal}})\ \text{Mn}]\text{Te} : Bi_2Te_3$ varying from 15 : 85, 21 : 79, 29 : 71, 31 : 69, 37 : 63 and 30 : 70 for $x_{nominal}$ = 0, 0.36, 0.5, 0.6, 0.7 and 0.85. The mixture was loaded into an alumina crucible and vacuum sealed inside a quartz tube. It was then heated to 900 °C in 4 hours and cooled to 598 °C in 0.5 hours. Then the ampule was cooled from 598°C to 592 °C in a duration of 3 days and stayed at 592 °C for 3 more days. The ampule was then centrifuged and shiny single crystals with lateral sizes $\sim 3{\times}3\ mm^2$ can be obtained. $PbBi_2Te_4$ single crystals can also be grown by this method, its physical properties are consistent with the previous report [64].

3.3 Results

Both WDS and PXRD measurements indicate that Pb successfully substitutes Mn in $MnBi_2Te_4$. The results are summarized in Fig. 3.2 and Table 3.1. Figure 3.2(a) shows the PDXR for various doping levels. All the peaks can be indexed by the $MnBi_2Te_4$ phase. If there is Bi_2Te_3 impurity, an additional hump can be seen on the right shoulder of the (107) peak. As shown in the inset of Fig.3.2(a), the Bi_2Te_3 phase is almost indiscernible. According to Table. 3.1, the doping variation in each growth batch is small. In $MnBi_2Te_4$, the molar concentration of (Mn+Pb) is 0.88(1) while the molar concentration of Bi is 2.08(1). This is consistent with the neutron and x-ray studies which reveal the partial occupancy of Bi atoms on the Mn sites. Upon doping, the amount of (Mn+Pb) stays around 0.80 while the amount of Bi is between 2.1 and 2.2, providing strong evidence that indeed Pb substitutes Mn atoms, not Bi. As plotted in Fig. 3.2(b), the real doping level x defined as Pb/(Pb+Mn) from the WDS data increases with the nominal doping level $x_{nominal}$. From 0.2 to 0.82, a

Table 3.1: Data summary of $(Mn_{1-x}Pb_x)Bi_2Te_4$. x refers to the molar ratio of Pb/(Pb+Mn) obtained by the WDS measurements. The lattice parameters obtained by PDXR refinement (a and c in Å). The effective magnetic momentum (μ_{eff} in μ_B/Mn) and Curie-Weiss temperature (T_{CW} in K) are calculated from Fig. 3.3 (see text), effective magnetic anisotropy (SK in meV) and effective interlayer magnetic interaction (SJ_c in meV) are obtained from magnetization measurements shown in the first row of Fig. 3.4 (see text), charge carrier density (n in $10^{20}cm^{-3}$) is calculated from Hall measurements shown in the third row of Fig. 3.4 (see text).

x_{nominal}	WDS	x	a	c	T_N	T_{CW}	SK	SJ_c	n
0	$Mn_{0.88(1)}Bi_{2.08(1)}Te_4$	0	4.33	40.91	23.0	5.0	0.080	0.090	1.3
0.36	$Mn_{0.64(1)}Pb_{0.16(1)}Bi_{2.16(2)}Te_4$	0.20(1)	4.35	41.05	18.0	5.0	0.035	0.065	2.8
0.5	$Mn_{0.55(4)}Pb_{0.33(4)}Bi_{2.10(2)}Te_4$	0.37(3)	4.37	41.20	14.5	6.5	0.030	0.055	3.5
0.6	$Mn_{0.38(1)}Pb_{0.43(1)}Bi_{2.19(1)}Te_4$	0.53(2)	4.39	41.33	9.5	4.0	0.030	0.040	4.1
0.7	$Mn_{0.24(1)}Pb_{0.55(4)}Bi_{2.15(1)}Te_4$	0.69(4)	4.40	41.44	4.5	2.5	0.025	0.025	12.9
0.85	$Mn_{0.14(1)}Pb_{0.67(1)}Bi_{2.20(1)}Te_4$	0.82(4)	4.42	41.56	2.0	0	–	–	24.6

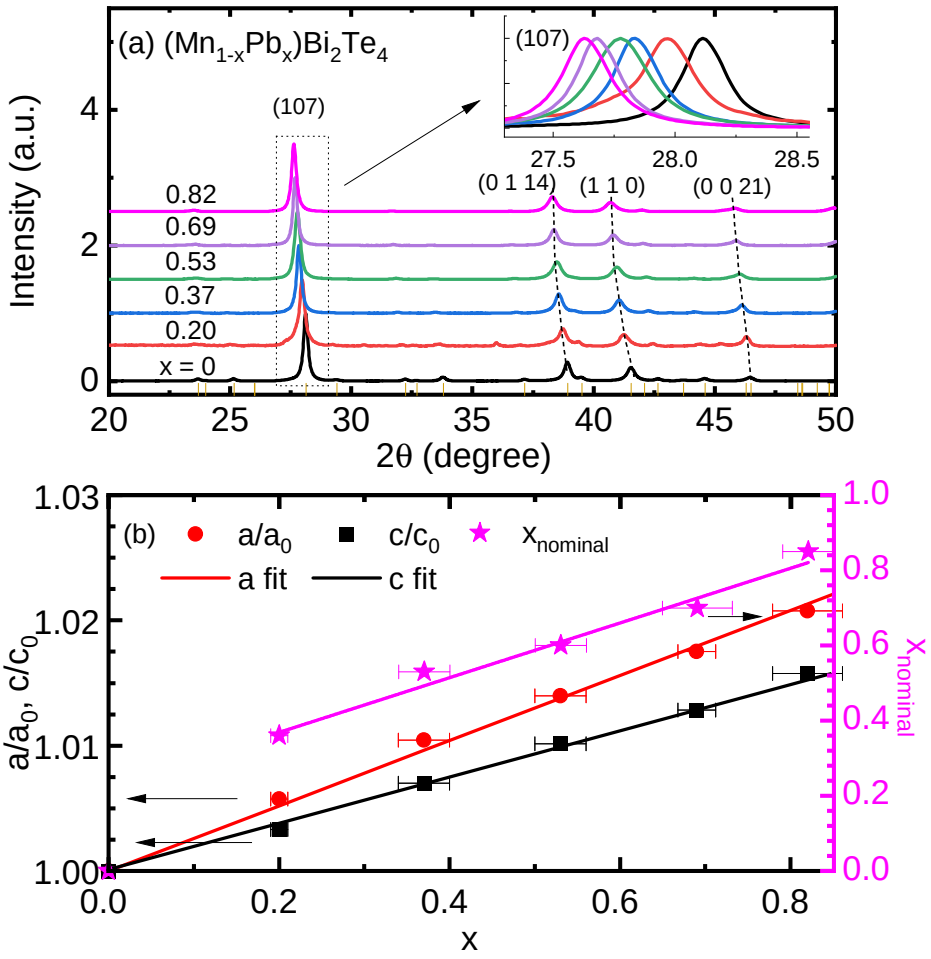

Figure 3.2: X-ray diffraction of $(Mn_{1-x}Pb_x)Bi_2Te_4$. (a) PXRDs for various concentrations. Inset: the zoom-in plot of the (1 0 7) PXRD peak. (b) The doping-dependent relative lattice parameters a/a_0, c/c_0 and nominal concentration used in growth. a_0 and c_0 are the lattice parameters of $MnBi_2Te_4$.

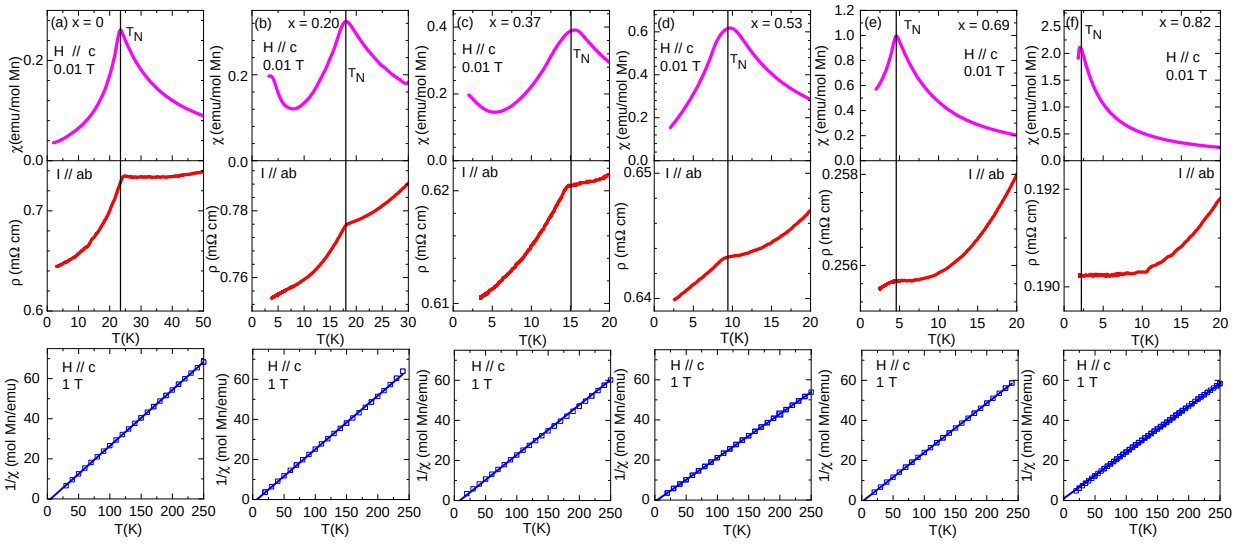

Figure 3.3: The evolution of temperature-dependent properties of $(Mn_{1-x}Pb_x)Bi_2Te_4$. Top row: $\chi(T)$, the temperature-dependent magnetic susceptibility under 0.01 T with $H \parallel$ c. Middle row: $\rho_{xx}(T)$, the temperature-dependent electrical resistivity with the current along the ab plane. Ordering temperature T_N for each concentration is marked and a correlation between two measurements can be observed. Bottom row: $1/\chi(T)$, the inverse magnetic susceptibility measured at 1 T above T_N. Curie-Weiss fits are shown in solid lines.

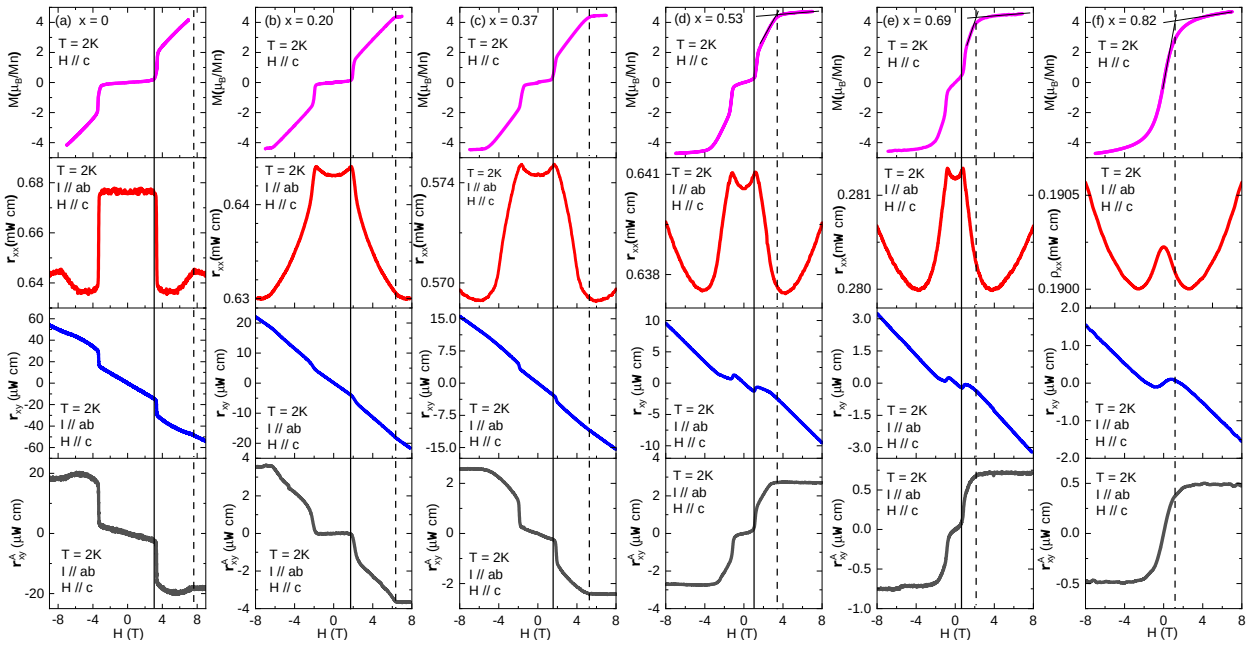

Figure 3.4: The evolution of magnetic-field-dependent properties of $(Mn_{1-x}Pb_x)Bi_2Te_4$. First row: $M(H)$, the isothermal magnetization at 2 K with $H \parallel c$. The reflection-point criterion used to determine the H_s is shown for $x \geq 0.53$. Second row: $\rho_{xx}(H)$, the magnetic field dependence of electrical resistivity with the current along the ab plane and $H \parallel c$. Third row: $\rho_{xy}(H)$, the Hall resistivity with the current along ab plane and $H \parallel c$. Fourth row: $\rho^A_{xy}(H)$, the anomalous Hall resistivity calculated by subtracting linear Hall background in $\rho_{xy}(H)$.

linear fitting results in $x = -0.28 + 1.34x_{nominal}$. Figure 3.2(b) also shows the evolution of lattice parameters with respect to x. The lattice parameters a and c increase linearly by 2.2% and 1.8% respectively from $x = 0$ to 0.82, consistent with Vegard's law. This is different from the Sb-doped $MnBi_2Te_4$ where c remains unchanged but a decreases with doping.

3.3.1 Magnetic and electrical transport properties

Magnetic and electrical transport properties of this doping series are shown in Figs. 3.3 and 3.4. The evolution of the magnetism throughout the doping process can be well traced in the temperature-dependent susceptibility with $H \parallel c$ ($\chi(T)$) and the temperature-dependent resistivity with $I \parallel ab$ ($\rho_{xx}(T)$) in Fig. 3.3. For $x = 0$, a sharp cusp in $\chi(T)$ and a drop in ρ_{xx} agree with the previous reports, indicating a paramagnetic (PM) to A-type AFM phase transition at $T_N = 24$ K. The cusp feature in $\chi(T)$ persists for $x \leq 0.82$ while the drop in ρ_{xx} can be observed up to $x = 0.69$. Together with the small magnitude of $\chi(T)$ across the whole doping series, these observations indicate the A-type AFM ground state with T_N decreasing from 24 K for $x = 0$ to 2 K for $x = 0.82$. We note the drop in ρ_{xx} at T_N becomes less dramatic upon doping (indiscernible at $x = 0.82$), which is consistent with the fact that the fewer the magnetic scattering centers, the weaker the spin disorder scattering.

The bottom panel of Fig. 3.3 presents the inverse magnetic susceptibility, $1/\chi$, with $H \parallel c$ and $H = 1$ T. As one can see, $1/\chi$ is rather linear in essentially entire range between 40 K to 250 K. The Curie-Weiss fitting results in the effective moment μ_{eff} of 5.7±0.3 μ_B/Mn with no clear doping-dependence (Table I). This is consistent with the theoretical value of 5.9 μ_B/Mn for high-spin Mn^{2+}. The Curie-Weiss temperature T_{CW} is positive for $x \leq 0.69$, consistent with the strong in-plane FM fluctuation; T_{CW} becomes zero at $x = 0.82$, suggesting AFM spin fluctuation in the paramagnetic state, likely due to the Mn lattice being very dilute.

Figure 3.4 presents the $M(H)$ (isothermal magnetization), $\rho_{xx}(H)$, $\rho_{xy}(H)$ (Hall resistivity) and $\rho^A_{xy}(H)$ (anomalous Hall resistivity) with $H \parallel c$ at 2 K. Except for the $x = 0.82$ sample, where no spin-flop feature appears at 2 K, all other samples with $x \leq 0.69$, a spin-flop transition can be well resolved in $M(H)$. The spin-flop transition field H_{sf} marked by the

vertical line decreases with increasing Pb doping, from 3.3 T for $x = 0$ to 0.92 T for $x = 0.69$. Meanwhile, the saturation field H_s marked by the vertical dash line also decreases with x, from 7.7 T [34] for $x = 0$ to 2.1 T for $x = 0.69$ and 1.2 T for $x = 0.82$. Furthermore, unlike Sb-doped $MnBi_2Te_4$ where the saturation moment decreases to 2.0 μ_B/Mn for $MnSb_2Te_4$ due to the formation of $\sim 16\%$ of Mn_{Bi} antisites [34,65], in all Pb-doped $MnBi_2Te_4$ samples, the magnetic moment at 7 T and 2 K remains around 4.5 μ_B/Mn (Table. I). This provides strong evidence that the amount of such antisites remains minimal during Pb doing.

Despite Bi and Te dominating the band characters at the Fermi level and the Mn band being a few eV away from the Fermi level, charge transport strongly couples to the magnetism. As shown in the second row in Fig. 3.4, at $x = 0$, upon increasing the field, a sharp decrease of ρ_{xx} happens at H_{sf} due to the loss of spin-disorder scattering when the system goes from the AFM state to the canted AFM state; ρ_{xx} then slightly increases in the canted AFM state and reaches a kink feature at H_s. A negative slope of ρ_{xy} indicates the electrons dominate the charge transport while the $\rho^A_{xy}(H)$ shows a sharp drop at H_{sf} and becomes independent to the $M(H)$ in the canted AFM state. Upon doping, electrons remain the dominant carrier in charge transport, which is in stark contrast with the Sb-doped $MnBi_2Te_4$, again suggesting the amount of the Mn_{Bi} antisites remains few. The sharp drop from both ρ_{xx} and ρ_{xy} continues to appear at H_{sf} for $x \leq 0.69$. As shown by the solid lines, the H_{sf} from three measurements corresponds well with each other. We can determine H_s using $M(H)$ and $\rho^A_{xy}(H)$, indicated by the dash lines. For $x = 0.82$, at 2 K where it just orders, no feature signaling H_{sf} can be observed while the H_s can be consistently determined by both $M(H)$ and ρ^A_{xy} using the criterion shown in the first row of Fig. 3.4.

To further investigate the crystal and magnetic structures, single-crystal neutron diffraction was performed on the $x = 0.37$ sample at 4.85 K. The refined structural parameters are summarized in Table II. Since Mn, Bi and Pb co-occupy the Mn site (3a site), which complicates the refinement, to make the refinement work, we confined the Pb concentration as the one obtained from the WDS measurement. Meanwhile, if we allow the $(Mn, Pb)_{Bi}$ antisite formation, that is, if we allow Mn and Pb to partially occupy the Bi site (6c site) in the refine-

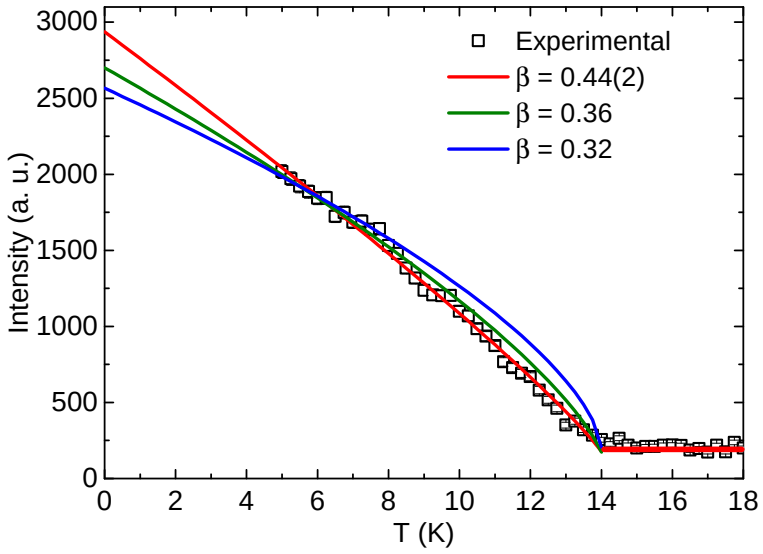

Figure 3.5: The temperature-dependent neutron peak intensity at magnetic reflection (1 0 -0.5) for the $x = 0.37$ sample. Order parameter fit results in a value of $\beta = 0.44(2)$. Curves with $\beta = 0.36$ (3D Heisenberg case) and $\beta = 0.32$ (3D Ising case) are also shown for comparison.

ment, the obtained Bi concentration is too low to agree with the WDS measurement, suggesting that the amount of (Mn, Pb)$_{Bi}$ antisites is negligible within the neutron measurement resolution. Our refinement leads to the chemical formula of $Mn_{0.50(1)}Pb_{0.33(1)}Bi_{2.17(1)}Te_4$, which agrees well with the WDS values. Using the crystal structural information, the refinement of the magnetic Bragg peaks results in an ordered moment of 4.3(1) μ_B/Mn at 4.85 K.

Figure 3.5 shows the peak intensity of the magnetic reflection (1 0 -0.5). It follows an empirical power law behavior,

$$I = A\left(\frac{T_N - T}{T_N}\right)^{2\beta} + B \tag{3.1}$$

where A is a proportional constant, β is the critical exponent of the order parameter, and B is the background. Unlike the undoped sample whose order parameter can be fitted by the 3D Heisenberg model near the critical temperature [30], from 5 to 20 K, the best fit is shown as the red curve, which yields $T_N = 14.1$ K and the critical exponent $\beta = 0.44(2)$,

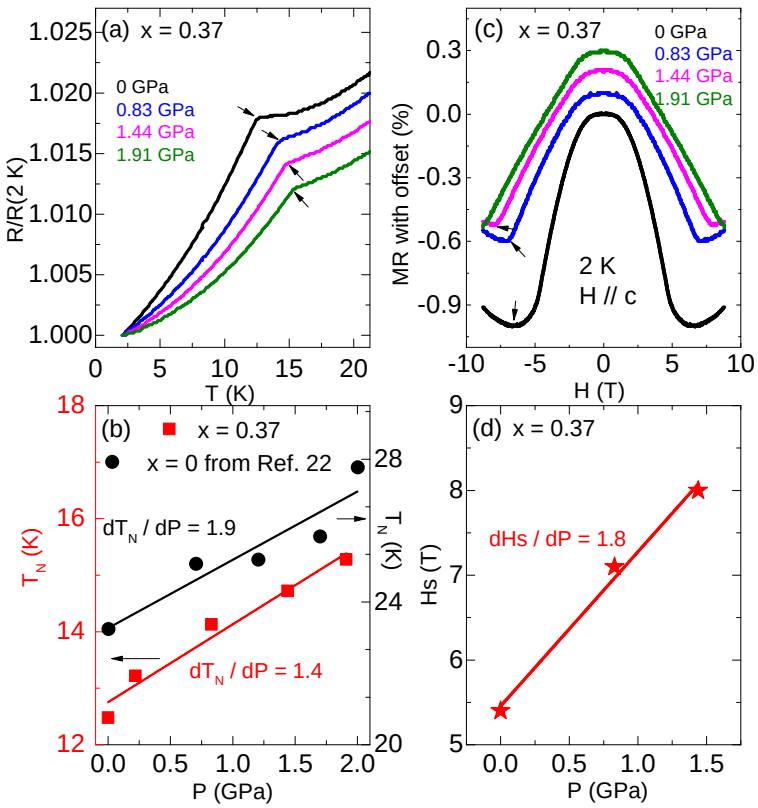

Figure 3.6: Pressure measurement of the $x = 0.37$ sample. (a) The temperature dependence of ρ_{xx} at different pressures. T_N is marked by black arrows. (b) The evolution of T_N with pressure. Linear fits of both data were shown in lines. (c) The field dependence of ρ_{xx} at different pressures with offset. H_s is marked by black arrows. (d) The evolution of H_s with pressure. Linear fit is shown in line.

considerably larger than that in $MnBi_2Te_4$ (0.36) [30]. We also show the curves with $\beta = 0.36$ (3D Heisenberg case) and $\beta = 0.32$ (3D Ising case), which clearly deviate from the data. Note that $\beta = 0.44$ is very close to the mean-field value, 0.5, and cannot represent the true criticality in any sensible Hamiltonian (nor do we expect the Hamiltonian class to change with doping). On the other hand, this number is rather close to critical exponents expected in various percolation models [66]. Thus, the temperature evolution of the observable order parameter may reflect static percolation, expected in this strongly disordered medium, rather than dynamic fluctuations.

Table 3.2: Refined structural parameters for the x =0.37 sample based on the single crystal neutron diffraction data. (number of reflections: 192; R_F = 3.83%; χ^2 = 28.7). χ^2 here is large because the experimental error bars are smaller than the standard deviation from merging equivalent reflections.

Atom	site	x	y	z	occ.	Moment at 4.85 K
Mn1	3a	0	0	0	0.50(1)	4.3(1) μ_B/Mn
Bi1	3a	0	0	0	0.17(1)	
Pb1	3a	0	0	0	0.33(1)	
Bi2	6c	0	0	0.42645(4)	1	
Te1	6c	0	0	0.13459(6)	1	
Te2	6c	0	0	0.29202(5)	1	

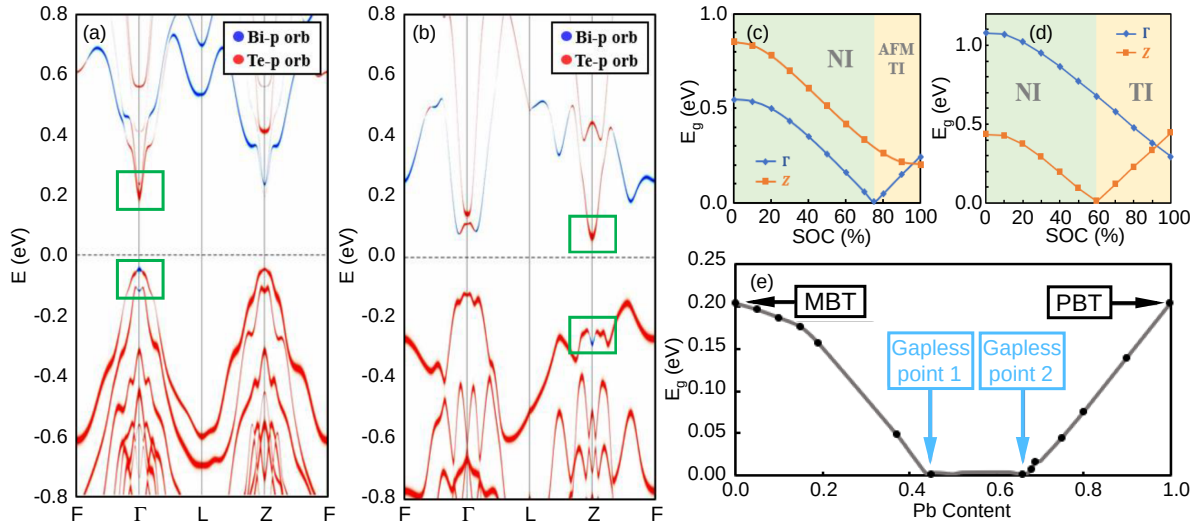

Figure 3.7: (a) The bulk band structure of $MnBi_2Te_4$ and (b) $PbBi_2Te_4$. The blue and red dots indicate the weight of the Bi-p orbitals and Te-p orbitals, respectively. (c) The gap value at Γ and Z point as a function of SOC strength for $MnBi_2Te_4$ and (d) $PbBi_2Te_4$. (e) The minimum bulk band gap along Γ - Z as function of Pb content.

To further study how interlayer and intralayer interactions will affect the magnetism in the doped samples, we measured the $x = 0.37$ sample under different hydrostatic pressure. Figure 3.6 shows the transport measurements for $x = 0.37$ under pressure. The sample remains in the AFM state for the pressure range we applied while the $\rho_{xx}(T)$ anomaly at T_N moves to higher temperatures under pressure. As summarized in Fig. 3.6 (b), T_N linearly increases with pressure at a rate of 1.4 K/GPa, which is smaller than 1.9 K/GPa for $x = 0$ [56]. Figure 3.6 (c) presents the pressure dependence of MR at 2 K. The $\sim 1\%$ drop in MR again suggests the ground state remains AFM. H_s marked with the arrows increases gradually with increasing pressure. The pressure dependence of H_s is summarized in Fig. 3.6 (d), which suggests a linear increase of H_s at the rate of 1.8 T/GPa. Both the increase of T_N and H_s under pressure indicate that the external pressure enhances the AFM interlayer coupling, which is expected due to the decreasing lattice parameter c under external pressure.

3.3.2 Band topology engineering

To understand the evolution of band structures as a function of Pb doping, we performed first-principle calculations on the bulk band structures of $(Mn_{1-x}Pb_x)Bi_2Te_4$ using the generalized gradient approximation (GGA) plus correlation parameter U (GGA+U) with spin-orbit coupling (SOC). The results are summarized in Fig. 3.7. Our calculations reveal an insulating ground state for both $MnBi_2Te_4$ and $PbBi_2Te_4$, the two end materials. The orbital projection shows that the Bi-p orbitals and the Te-p orbitals dominate around the Fermi level (E_F), while the Mn-d orbitals and the Pb-p orbitals are far away from the E_F (Fig. 3.7 (a) and (b)). As shown in Fig. 3.7 (a), for $MnBi_2Te_4$, there are clear band inversion features between the Bi-p and Te-p states at the Γ point, supporting a magnetic topological insulator state which is consistent with the literature. For $PbBi_2Te_4$, contrary to $MnBi_2Te_4$ whose band inversion appears at the Γ point, the band inversion of $PbBi_2Te_4$ occurs at the Z point, resulting in a strong topological insulator phase due to the preservation of spatial inversion and time-reversal symmetry (Fig. 3.7 (b)). Our calculation is consistent with the previous research on $PbBi_2Te_4$ [67, 68].

We now investigate the evolution of the band gap via the fine-tuning of the strength of SOC (Fig. 3.7 (c)). We found that for both $MnBi_2Te_4$ and $PbBi_2Te_4$, the band gaps at the Γ and Z points decrease rapidly when increasing the strength of SOC. In particular, for $MnBi_2Te_4$, the bulk gap at the Γ point first decreases to zero and then reopens as the SOC is larger than 75%. On the other hand, for $PbBi_2Te_4$, we find the bulk gap at Z point is the one that closes first and then reopens at SOC $\sim$ 60% (Fig. 3.7 (d)). Therefore, topological phase transitions can appear when the SOC increases for both compounds.

Following the line of reasoning, will the Pb doping on $MnBi_2Te_4$ induce topological phase transitions? To shed light on this, we calculate the band structures of $(Mn_{1-x}Pb_x)Bi_2Te_4$. Figure 3.7 (e) shows the minimum gap value between the valence band and conduction band as a function x. Generally, topological phase transition between magnetic and nonmagnetic states do not induce additional band inversion, because the two end of states possess different symmetry. However, this concept has its limitations, it is only valid to the trivial to nontrivial

phase transition that occurs at the same time-reversal symmetry momenta in the two end systems. As we have shown that the band inversion in $MnBi_2Te_4$ and $PbBi_2Te_4$ appear at Γ or Z point, respectively. Thus complicated band inversion diagram is expected. Indeed, our results display two gapless points when doping concentration achieves $x = 0.44$ and $x = 0.66$. Since the band inversion may exist at Γ and Z simultaneously between these two ratios, we expect that there might be a new topological phase in this doping regime. Detailed DFT and angle-resolved photoemission spectroscopy (ARPES) study of the effect of doping in this material are left as an open question for future studies.

3.4 Discussion

Figures 3.8 (a)-(f) summarize the doping-dependent magnetic properties. The doping-dependence and the magnitudes of T_{CW} (Fig. 3.8(a)) are not trivial. The system is very 2D and one expects the T_{CW} to be set by strong intraplanar ferromagnetic interactions and scale with the average number of Mn neighbors, *i.e.*, as $1 - x$, which is not the case here, especially in the Mn-rich side. We argue this is because at 40–250 K we may not be in the true Curie-Weiss regime due to the strong FM in-plane fluctuations, as indicated by the μ_{eff} (Fig. 3.8(b)) being slightly smaller than the expected 5.9 μ_B/Mn. Indeed, neutron scattering experiments indicate strong FM in-plane correlations even at room temperature for $MnBi_2Te_4$ [69]. Furthermore, in a 2D system where strong fluctuation always exists, one would expect the T_N to be strongly suppressed compared to the mean-field limit value, T_{MFT}; indeed, even in the least-fluctuating square Ising model, T_N is nearly smaller than half of T_{MFT}. On the contrary, T_{CW} we obtained using the Curie-Weiss fit of our data for 40-250 K listed in Table I is much smaller than T_N. This may be partially because we are not in the true Curie-Weiss regime as aforementioned. But interestingly, similarly odd behavior was observed in some other quasi-2D ferromagnet or A-type antiferromagnets. For instance, $T_N = 14$ K and high-temperature $T_{CW} = 11(1)$ K for $CrCl_3$ [70]; $T_N = 61$ K and $T_{CW} = 71(1)$ K for CrI_3 [71]. These large T_N/T_{CW} ratio, to the best of our knowledge, was never explained, since a quantitative theory of spin-susceptibility in Mermin-Wagner systems

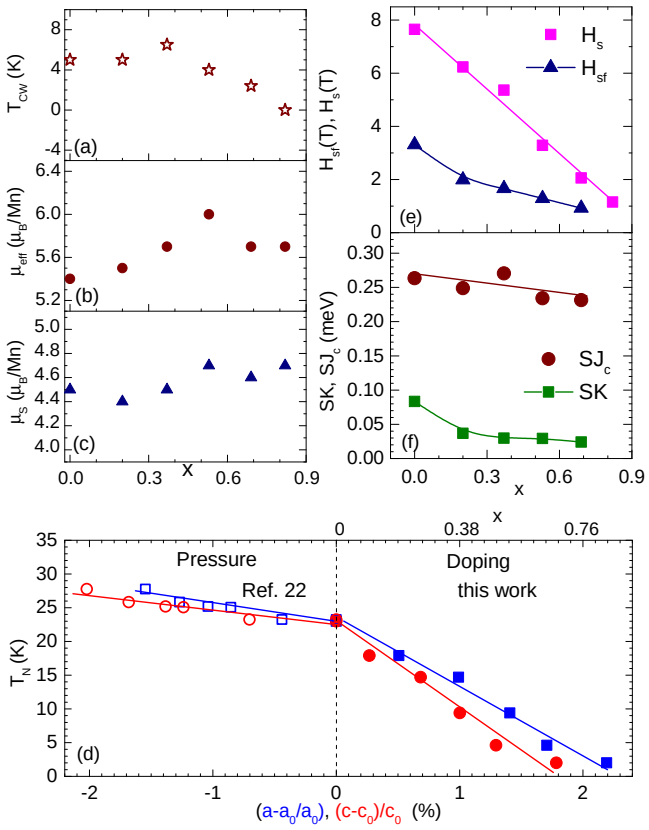

Figure 3.8: (a) The doping dependence of the Curie-Weiss temperature, (b) The doping dependence of the Curie-Weiss effective moment per Mn, (c) The doping dependence of the magnetic moment per Mn for $x = 0$ (2 K, 7.7 T) and $x > 0$ (2 K, 7 T), (d) Néel temperature vs. x, Néel temperature vs. $(a-a_0)/a_0$ and Néel temperature vs. $(c-c_0)/c_0$ for the pressure work (Ref. [56]) and this doping work, (e) Spin-flop field and saturation field determined from magnetic and transport measurements with $H \parallel c$, (f) The doping dependence of the $effective$ (see the main text) interlayer plane-plane coupling per Mn site SJ_c and the $effective$ magnetic anisotropy per Mn SK. All lines are guides to the eye.

has never been worked out.

Upon doping, μ_s per Mn slightly increases (Fig. 7(c)), suggesting possible reduction in the number of the Mn_{Bi} antisites, consistent with our neutron scattering refinement. Figure 7(d) shows a comparison of the pressure work [56] and our doping work. Apparently, dT_N/da or dT_N/dc is much larger in Pb-doped $MnBi_2Te_4$ than that in the pressurized $MnBi_2Te_4$. This is reasonable since the former comes from both the magnetic dilution and lattice expansion while the latter is only caused by lattice expansion. Furthermore, comparing with $(Mn_{1-x}Sn_x)Bi_2Te_4$ [72] where $T_N \sim 18$ K and $H_s \sim 6$ T at $x = 0.5$, Pb doping shows a much stronger suppression of magnetism with $T_N \sim 9$ K and $H_s \sim 3$ T at $x = 0.5$ (Fig. 7(d) and (e)). Due to the larger atomic radius difference between Pb and Mn, Pb doping can cause a faster lattice parameter increase than Sn, it is thus reasonable to expect a faster suppression of the AFM coupling, T_N and H_s.

Unlike the nonlinear decrease of T_N and H_s in Sb-doped $MnBi_2Te_4$ where the Mn1 sublattice is diluted and the Mn2 sublattice gets enhanced upon doping [34], here T_N and H_s decrease rather linearly as shown in Fig. 3.8(d) and (e), leading to $T_N = 24 - 27.4x$ and $H_s = 7.70 - 7.98x$ up to $x = 0.82$. The clear difference between these two doping series indicates that indeed the Pb-doping series is ideal to investigate the unadulterated magnetic dilution effect in $MnBi_2Te_4$.

So now let us understand these behaviors accounting for the dilution effect when a nonmagnetic Pb replaces a magnetic Mn so that the fraction of magnetic site is $\delta = 1 - x$. In a quasi-2D AFM system, long-range order is impossible without either interlayer coupling, J_c, or uniaxial magnetic anisotropy, K. We define the former as the effective coupling strength between two neighboring planes per Mn site and the latter as magnetic anisotropy parameter per Mn site. That is to say, the effective interplanar coupling J_c includes all possible Mn-Mn exchange paths between the planes, and the effective anisotropy K includes both single-ion and exchange anisotropies.

We can write the full Hamiltonian as:

$$E = E_0 + \delta^2 J_c S_i \cdot S_{i+1} - \delta K (S_i^z)^2 - \delta g \mu_B S_i \cdot H, \tag{3.2}$$

where g is the Lande factor, i labels Mn planes, $J_c > 0$ for AFM and $K > 0$ to ensure z is the easy axis. Since a magnetic bond needs to have Mn on both ends, δ^2 arises for the two-site exchange term. Meanwhile, δ arises for the single-ion magnetic anisotropy and Zeeman terms. Thus the energy in the spin-flop phase is,

$$\begin{aligned} E(H,\phi) =& (E_1 \mp \delta K S^2/2) + \delta^2 J_c S^2 \cos(\pi - 2\phi) \\ & \pm \delta K S^2 \cos^2\phi - \delta g \mu_B S H \sin\phi, \end{aligned} \tag{3.3}$$

where $E_1 = E_0 - \delta K S^2/2$, the upper (lower) sign corresponds to the angle between H and S as $\pi/2 - \phi$ with H along the easy axis c (H along the hard ab plane). By minimizing Eq.3.3 at $\phi = \pi/2$, we can get the saturation fields,

$$H_s^{\parallel c} = 2(2\delta J_c - K)S/g\mu_B \tag{3.4}$$

$$H_s^{\parallel ab} = 2(2\delta J_c + K)S/g\mu_B, \tag{3.5}$$

Similarly, one can estimate the spin-flop threshold:

$$H_{sf} = \sqrt{K(2\delta J_c - K)}(2S/g\mu_B), \tag{3.6}$$

from Eq.3.4 and 3.6:

$$SK = (g\mu_B/2)(H_{sf}^2/H_s^{\parallel c}) \tag{3.7}$$

$$SJ_c = (g\mu_B/4\delta)\left(H_s^{\parallel c} + H_{sf}^2/\, H_s^{\parallel c}\right). \tag{3.8}$$

Note that this scaling is only true if magnetic anisotropy is of a single-ion origin. If there is a contribution from the exchange anisotropy, that contribution will be scaled as δ^2, and our K in Eq.4-6 will be replaced as $K_1 + \delta K_2$ where K_1 is the single-ion anisotropy parameter and K_2 is the exchange anisotropy parameter.

Using Eq.7 and 8, we estimate the effective SK and SJ_c, as shown in Fig. 3.8 (f). SJ_c slightly decreases from 0.26 meV at $x = 0$ to 0.23 meV at $x = 0.69$, being consistent with the small change in lattice parameter c. Meanwhile SK shows a monotonic decrease with a sharp drop from 0.08 meV at $x = 0$ to 0.04 meV at $x = 0.20$ and then a slow decrease

to 0.02 meV at $x = 0.69$. We thus readily see that H_s is linear in δ, as seen in Fig. 3.8 (e), because it is defined mostly by δJ_c. But the behavior of H_{sf} is harder to understand: naively, it can behave either sublinearly, or, in the extreme case of the dominating exchange anisotropy, linearly with δ. Figure 3.8 (e) shows that for $x0.2$ the behavior is indeed linear, suggesting that the anisotropy there is dominated by the exchange anisotropy. But there is an additional contribution at $x = 0$, of about 0.05 meV, which mostly disappears at $x = 0.2$. The only plausible explanation is that this contribution comes from the single-ion anisotropy which is strongly affected by the local environment, and only appears if all or nearly all of the nearest neighbors of a given Mn ion are also Mn. It is easy to see that the probability of having a Mn at a given site, *and* having all its neighbors Mn, is δ^7, and is only 100% at $x = 0$, 20% at $x = 0.2$, and 8% at $x = 0.3$.

We can try to understand the linear doping dependence of T_N by studying the magnetic dilution effect in the mean-field limit (*i.e.*, in the Weiss molecular field theory). We consider an individual Mn ion with the spin S and 6 nearest sites. Under doping, the mean-field-theory temperature T_{MFT} (we use this notation to distinguish it from the T_{CW} extracted experimentally from $1/\chi(T)$ for 40–250 K, which, as discussed above, does not represent the true MFT limit) is given by $T_{\mathrm{MFT}} \propto \delta\mu_{eff}^2$, which linearly decreases with x. Given that T_N is, generally speaking, nothing but fluctuations-renormalized mean-field-theory temperature, $T_N \approx T_{\mathrm{MFT}}/(a + b\log(\bar{J}/\bar{J}_c))$, where a and b are not supposed to change much with doping, J is the intraplanar magnetic coupling and $J \gg J_c$, bars means spacial average. As discussed above, $\bar{J} \sim \delta^2 J$, and $\bar{J}_c \sim \delta^2 J_c$, so $\log(\bar{J}/\bar{J}_c) \sim \log(J/J_c)$. Since T_N depends on J and J_c logarithmically weakly, we conclude that T_N should roughly follow T_{MFT} and thus linearly decreases with x.

Lastly, the bottom row of Fig. 3.4 shows that a sign change of the anomalous Hall resistivity $\rho_{xy}^A(H)$ occurs between $x = 0.37$ and $x = 0.53$, may suggesting possible band structure changed in this regime. Thus we call ARPES experiments to investigate the band structures of this doping series to address this question.

3.5 Summary and Outlook

In summary, we have grown high-quality single crystals of $(Mn_{1-x}Pb_x)Bi_2Te_4$ with x ranging from 0 to 0.82. We find that this doping series provides a great platform to investigate the magnetic dilution effect in van der Waals magnets. The Néel temperature and saturation field decrease linearly with doping, which can be well understood in a simple model considering the dilution effects. Moreover, our DFT calculations reveal two gapless points appearing at $x = 0.44$ and $x = 0.66$. Together with the sign change of the anomalous Hall resistivity between $x = 0.37$ and $x = 0.53$, this may suggest possible topological phase transitions in this doping series.

CHAPTER 4

Unconventional Pressure-Driven Metamagnetic Transitions in Topological van der Waals Magnets

This chapter is adapted from [58]. This work was done in collaboration with Prof. Igor Mazin from George Mason University on theoretical understanding.

4.1 Introduction

Van der Waals (vdW) magnets have laid the material foundation for engineering two-dimensional (2D) thin-film devices and heterostructures with intrinsic magnetism. Triggering metamagnetic transitions between ordered states and understanding how such manipulations are driven open up unprecedented opportunities in magneto-electronics, spintronics and topotronics [73–86]. Versatile means, including layer-thickness engineering, electro-gating, chemical doping, strain, pressure, etc. have been actively explored to modify the three major interactions including magnetic anisotropy, interlayer and intralayer magnetic couplings, with the aim of tuning the competing magnetic states. However, due to the lack of vdW magnets with comparable ferromagnetic (FM) and antiferromagnetic (AFM) energies, despite extensive efforts, the activation of the metamagnetic transitions between these two states has only been unambiguously experimentally realized in CrI_3 and CrSBr insulators [80–88], and there they are likely triggered by the structural changes. This has hindered progress in understanding the roles that these disparate magnetic interactions play in driving such transitions.

Recently, the $MnBi_{2n}Te_{3n+1}$ (MBT) family has been discovered to be intrinsic vdW mag-

nets with non-trivial band topology [23, 31, 32, 42–46, 49–51, 53–55]. They are composed of alternating $(n-1)$ [Bi_2Te_3] quintuple layers (QLs) and one [$MnBi_2Te_4$] septuple layer (SL). In the 2D limit of $MnBi_2Te_4$, due to the interplay of magnetism and band topology, emergent phenomena including the quantized Hall conductance, Chern insulator state and large layer Hall effect have been observed [24,25,47,48]. Besides their fascinating non-trivial band topology, this is a family with great structural and magnetic tunability. With increasing n, $MnBi_2Te_4$, $MnBi_4Te_7$ and $MnBi_6Te_{10}$ become A-type antiferromagnets, while $MnBi_8Te_{13}$ becomes FM. Particularly, the as-grown $MnBi_4Te_7$ and $MnBi_6Te_{10}$ may become FM under certain growth conditions [49,89], indicating close proximity of FM and AFM energy scales in this family. Chemical doping has been used to tune the magnetism in MBT [34,35,59,60,90]. The effect can be best seen in $Mn(Bi_{1-x}Sb_x)_4Te_7$, where a doping-dependent metamagnetic transition between the FM and AFM states is observed [60]. However, the vacancies and antisite disorder introduced by doping are uncontrollable, making the delineation of the effects of the three major magnetic interactions challenging. Meanwhile, external pressure serves as a tuning knob without changing chemical disorder [56, 91]. However, it has been seldom applied to the MBT family where the understanding of these magnetic interactions still remain elusive [56, 57, 91]. In this letter, using electrical transport and magnetometry measurements, we discover the extremely sensitive, non-trivial and even re-entrant pressure-driven activation and manipulation of the metamagnetic transitions in $Mn(Bi_{1-x}Sb_x)_4Te_7$.

In $Mn(Bi_{1-x}Sb_x)_4Te_7$, Sb atoms not only replace Bi atoms but also promote site mixing between Sb and Mn. The presence of $Mn_{(Bi,Sb)}$ antisites leads to Mn1, Mn2 and Mn3 sublattices (Fig. 4.1 (a)) [60]. Since the Mn2 spins are always antiferromagnetically coupled with the Mn1, we will, for simplicity, focus on the Mn1 sublattice. In MBT, magnetism strongly couples with the charge carriers. Take $x = 0.48$ for example, upon cooling, $\rho(T)$ decreases with two slope changes (Fig. 4.1 (b)). One is at $T_N = 13.3$ K, associated with the PM to AFM transition of the Mn1 lattice. The other is a sharp resistivity drop at $T_{M1} = 9.7$ K, arising from the AFM to FM metamagnetic transition of the Mn1 spins. The sharp transition suggests the uniform doping of the sample, which is consistent with our

WDS measurements [60]. With $H//c$, at 10 K, a sudden decrease of MR appears at around 0.4 kOe by $\sim$ 5% due to the loss of spin disorder scattering from the AFM to forced FM state [60]. In contrast, at 2 K, where the Mn1 spins are in the FM state, a weak monotonic decrease in MR occurs across the coercive field. In this chapter, together with the magnetic data, the distinct MR behaviors discussed above will be used to differentiate if the Mn1 spins are AFM or FM.

In this chapter, I will introduce how we used electrical transport and magnetometry measurements to show the extremely sensitive pressure-driven activation and manipulation of the metamagnetic transitions in Sb-doped MnBi4Te7, which are non-trivial and even re-entrant. By systematic investigations of the temperature-pressure (T P) phase diagrams, we further demonstrate that our experiment provides a rare platform to distin- guish and understand the effects of magnetic anisotropy, interlayer and intralayer couplings on vdW magnetism.

4.2 Result

Five different doping levels were selected for the pressure study (Fig. 4.2). For $x = 0$, at 0 GPa, $Mn(Bi_{1-x}Sb_x)_4Te_7$ is AFM below $T_N = 12.2$ K. T_N decreases slightly with pressure, similar to a previous study [57]. All MR curves at $P \leq 1.1$ GPa show a clear sudden drop, indicating that the system remains in the AFM state under pressure. For $x = 0.48$, T_N is essentially unaffected by pressure up to 1.97 GPa, the highest pressure we applied. In contrast, the FM to AFM metamagnetic transition at T_{M1} is extremely sensitive and becomes first-order like under pressure. At 0.89 GPa, T_{M1} is completely suppressed, leaving the ground state as AFM. Indeed, our MR data at 2 K (Fig. 4.2(g)) shows a weak monotonic decrease for $P \leq 0.55$ GPa that is consistent with a FM ground state, while for $P \geq 0.89$ GPa, the sharp drop in MR reveals the AFM ground state. For $x = 0.57$, at 0 GPa, the PM to FM transition is revealed by the single resistivity anomaly at T_C and the weak monotonic MR decrease at 2 K. At 0.39 GPa, $\rho(T)$ shows two slope changes, suggesting the emergence of a pressure-induced AFM phase between $T_N = 14.4$ K and $T_{M1} = 8.0$ K. T_N

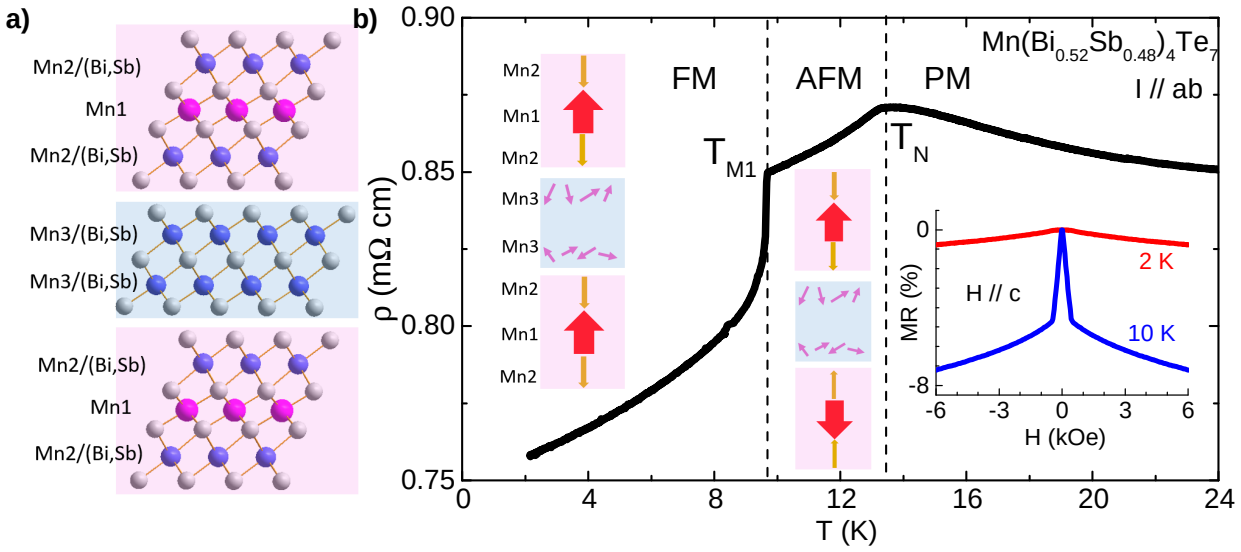

Figure 4.1: (a): The crystal structure of $Mn(Bi_{1-x}Sb_x)_4Te_7$. Sb doping can introduce $Mn_{(Bi,Sb)}$ antisites. Mn1 represents the Mn atoms on the Mn site; Mn2 labels the Mn atoms on the (Bi, Sb) site in the SLs; Mn3 denotes the Mn atoms on the (Bi, Sb) site in the QLs. (b) The temperature-dependent resistivity, $\rho(T)$ of $x = 0.48$ sample under ambient pressure, with schematics of the magnetic structures [60]. Upon cooling, Mn1 sublattice undergoes PM $\rightarrow$ AFM $\rightarrow$ FM transitions. In these ordered states, Mn1 and Mn2 sublattices are always AFM to each other along the c axis while Mn3 spins are paramagnetic. Right inset: its magnetoresistance MR(H) in the FM state (2 K) and AFM state (10 K).

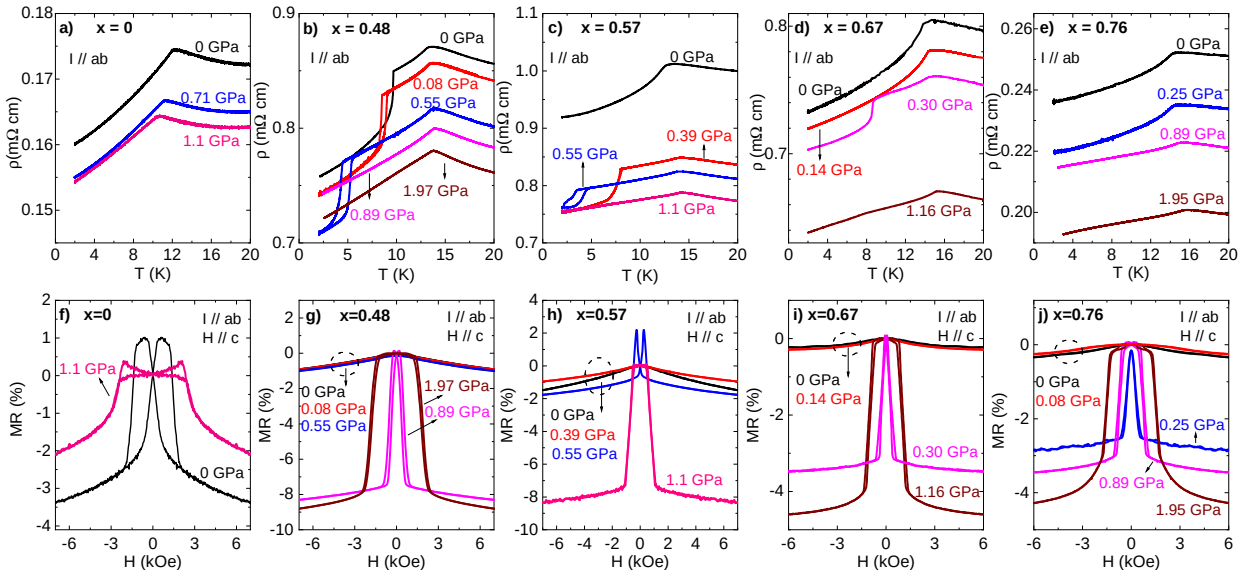

Figure 4.2: The effect of external pressures on the electrical properties of $Mn(Bi_{1-x}Sb_x)_4Te_7$ ($x = 0$, 0.48, 0.57, 0.67 and 0.76). (a)-(e) $\rho(T)$ at different pressures with the current $I//ab$ plane. (f)-(j): MR(H) at 2 K under pressures with $I//ab$ and $H//c$. The sharp drop in MR indicates the Mn1 spins are at the AFM state while the MR showing weak field dependence suggests FM state of the Mn1 spins.

slightly increases with pressure while T_{M1} is completely suppressed above 0.55 GPa. MR measurements confirm that the ground state is AFM for $P \leq 0.55$ GPa and FM for $P \geq 1.1$ GPa. For $x = 0.67$, although the pressure effect seems similar to that of $x = 0.57$, the ground state at 0.30 GPa is a puzzle. The $\rho(T)$ data implies PM $\rightarrow$ AFM $\rightarrow$ FM transitions and thus a FM ground state; however, the MR at 2 K shows a sharp drop, indicating an AFM ground state. These contradicting observations may suggest the re-entrance of AFM state, which will be discussed later. For $x = 0.76$, despite the envelope of $\rho(T)$ barely changing under pressure (Fig. 4.2(e)), remarkably, the MR data suggests that this compound is the most sensitive to pressure among all, with the ground state being FM below 0.08 GPa and AFM above 0.25 GPa.

To further investigate the puzzling ground states, magnetic susceptibility $\chi(T)$ and isothermal magnetization $M(H)$ were measured with $H||c$ and shown in Fig. 4.3. For $x = 0.57$, at ambient pressure, $\chi(T)$ shows a steep upturn plateau at T_C and a large bi-

furcation between the field-cooled (FC) and zero-field-cooled (ZFC) data; together with the typical hysteresis loop in $M(H)$ at 2 K, this indicates a FM ground state. At 0.34 GPa, the envelope of $\chi(T)$ evolves to show two anomalies. A cusp (PM to AFM) at T_N and a steep upturn plateau (AFM to FM) at T_{M1}. Under higher pressures, T_N slightly moves to higher temperature, while T_{M1} is completely suppressed above 0.64 GPa, where the $M(H)$ at 2 K shows the spin-flip feature, consistent with an AFM ground state. For $x = 0.67$, $\chi(T)$ resembles that of $x = 0.57$. However, closer examination of the 0.33 GPa data reveals that upon cooling, following the broad maximum, an additional "kink" feature highlighted by the circle in Fig. 4.3(c) emerges in the FC $\chi(T)$, suggesting three sequential magnetic transitions. Indeed, the $M(H)$ data shown in Figs. 4.3(d-e) indicate complex phase transitions. In particular, at 0.33 GPa, it goes from PM to AFM at T_N, then the first metamagnetic transition from the AFM state to the FM state at T_{M1}, and then the second metamagnetic transition from the FM state to the AFM state at T_{M2}. For $x = 0.76$, at 0.13 GPa, following the broad maximum, a kink feature in FC $\chi(T)$ sets in at $T_{M2} = 4.2$ K which, together with Fig. 4.3(g), suggests a metamagnetic transition from a FM state to an AFM state at T_{M2}. T_{M2} increases under pressure, which manifests as a sharp drop in $\chi(T)$ at 0.29 GPa and then becomes a cusp feature at 0.45 GPa. The sequence of these phase transitions can also be inferred from the $M(H)$ data (Fig. 4.3(h)). Upon cooling, at 0 GPa, it stays FM; at 0.13 and 0.29 GPa, it is FM $\rightarrow$ AFM; above 0.45 GPa, it remains AFM.

Figures. 4.4 (a)-(e) summarize the temperature-pressure ($T - P$) phase diagrams. The upper phase line represents the ordering transition from the PM state to the ordered state while the lower phase line marks the metamagnetic transitions between ordered states.

4.3 Discussion

Several aspects are particularly unexpected, if not counterintuitive. First, as represented by the upper phase line, at sufficiently high doping levels (Fig. 4.4(d,e)), the magnetic order switches suddenly from FM to AFM with pressure, yet the ordering temperature (T_C or T_N, respectively) is basically unchanged (a very tiny notch is barely discernible at the triple

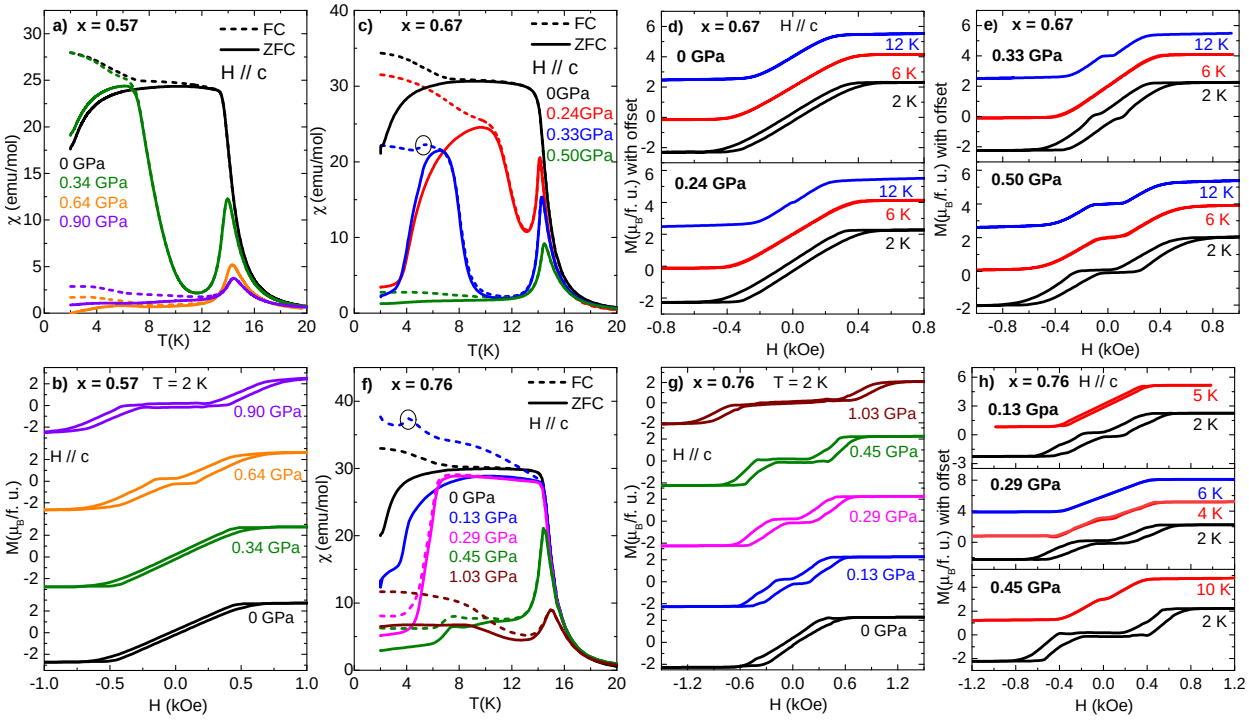

Figure 4.3: The effect of external pressures on the magnetic properties of $Mn(Bi_{1-x}Sb_x)_4Te_7$ ($x = 0.57$, 0.67 and 0.76): (a), (c), (f) The temperature dependant ZFC and FC magnetic susceptibility $\chi(T)$ with $H//c$. (b), (g): The isothermal magnetization $M(H)$ at 2 K at different pressures for $x = 0.57$ (b), and 0.76 (g). (d), (e) and (h): at fixed pressures, the $M(H)$ curves at different temperatures for $x = 0.67$ ((d) and (e)), and $x = 0.76$ (h). $M(H)$ data are analyzed to remove the lead signal, so slight discontinuity in data are induced.

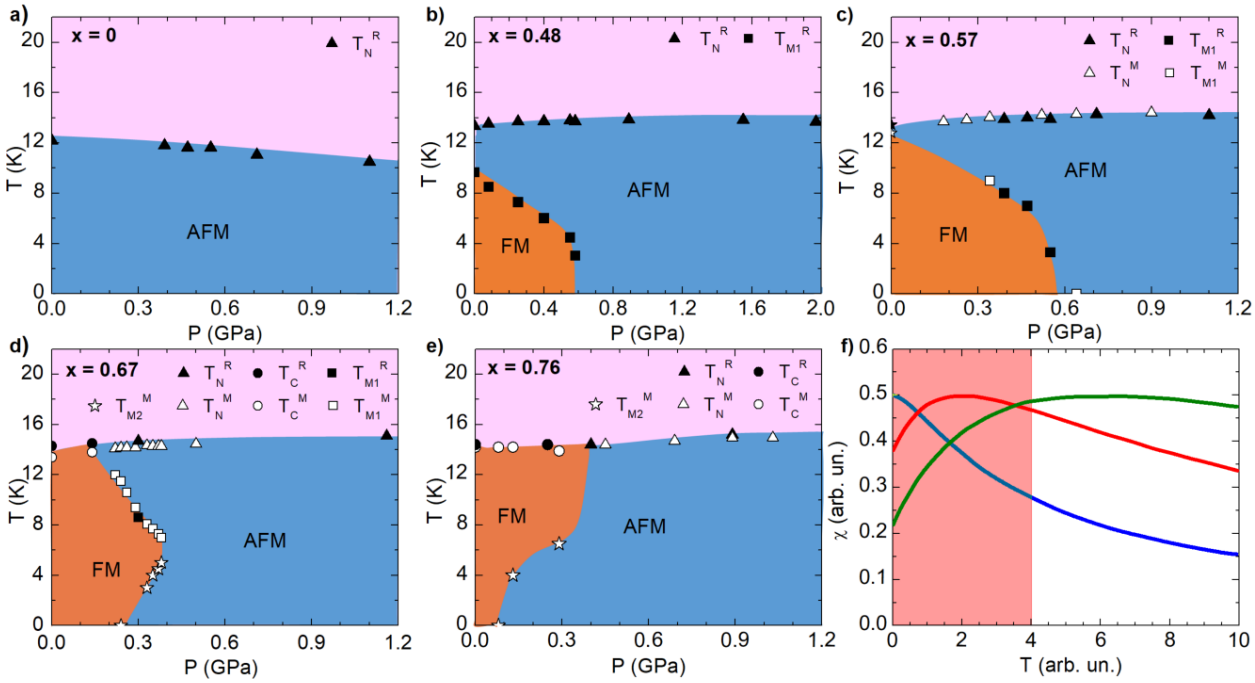

Figure 4.4: (a)-(e) Temperature-pressure ($T - P$) phase diagrams for $Mn(Bi_{1-x}Sb_x)_4Te_7$ (x = 0, 0.48, 0.57, 0.67 and 0.76) under pressures. T_C and T_N are the magnetic ordering temperatures of a PM to FM or AFM transition, respectively. T_{M1} and T_{M2} are the metamagnetic temperatures where an AFM $\rightarrow$ FM transition or a FM $\rightarrow$ AFM transition appears upon cooling, respectively. T_N^R, T_C^R and T_{M1}^R were extracted by taking the first derivative of resistivity data. T_N^M, T_C^M, T_{M1}^M and T_{M2}^M are determined by the first derivative of magnetic susceptibility data and then confirmed with isothermal magnetization measurements across critical temperatures. Note: the □/■ phase line representing the AFM to FM metamagnetic transition upon cooling is a first-order phase line while the others are all second-order phase lines. (f) Typical behavior of susceptibility in a system with antiferromagnetic or spin-glass type correlations. The blue/red/green lines correspond to $T_{CW} \approx 3, 7$ and 15. note that in a limited temperature range shown by pink shading, χ can either grow, decay, or show non-monotonic behavior.

point at $x = 0.76$). Naïvely speaking, one would expect that at the triple point where the magnetic order is fully frustrated, the transition temperature, if at all existed, should be much lower. Second, pressure induces ferromagnetism at low temperatures, but the order switches back to AFM upon cooling. Such FM to AFM metamagnetic transitions are rare (the best-known example is FeRh) [92, 93], and usually driven by the large volume effect at the metamagnetic transition (Clausius-Clapeyron theorem). This does not seem to be the case in our material, especially in view of the fact that the metamagnetic transitions marked with stars in Fig. 4.4(d,e) are second-order and are unlikely to be due to the volume effect. Finally, the sign of the pressure coefficient of the metamagnetic transitions, dT_M/dP, varies with doping: $dT_M/dP < 0$ for $x \lesssim 0.6$, $dT_M/dP > 0$ for $x \gtrsim 0.7$, and for $x = 0.67$ it is positive at low, and negative at higher temperatures.

These seemingly perplexing observations are all rooted in the unique separation of magnetic interaction in $Mn(Bi_{1-x}Sb_x)_4Te_7$. Indeed, it can be viewed, in a first approximation, as two overlapping magnetic subsystems, shaded in Fig. 4.1(a) as pink and blue. In the discussion below, for simplicity, the former shall be referred to as Mn1 and the latter as Mn3.

Let us first consider Mn1. A single Mn1 layer forms a 2D magnetic system with strong FM intraplanar coupling $J > 0$ and weak interplanar coupling of varying sign $|J_\perp| \ll J$. In addition, it may have intraplanar magnetic anisotropy, which can, without loss of generality, be absorbed into a single-site term, so that the total magnetic Hamiltonian looks like

$$H_{11} = \sum_{ii'} J S_i \cdot S_{i'} + \sum_{ij} J_\perp S_i \cdot S_j + \sum_i K {S_{iz}}^2. \tag{4.1}$$

Here i, i' denote sites in the same layer, and i, j in the neighboring layers. For our system, $J < 0$ and $J_\perp > 0$.

Per Mermin-Wagner theorem, in the 2D limit, a system does not order at any finite temperature if the exchange coupling is isotropic or if it has an easy-plane anisotropy ($K > 0$). On the other hand, a 2D easy-axis system with $K < 0$ and/or nonzero $J_\perp$ orders at a

temperature generally determined as

$$T_c = \frac{a|J|}{b + \log(J/J_{eff})} \tag{4.2}$$

where a, b and c are constants of the order of 1, and J_{eff} is a combination of $J_\perp$ and K that reduces to K in the $J_\perp \to 0$ limit. For instance, in Ref. [94] , an expression for J_{eff} was derived as $J_{eff} = K + J_\perp + \sqrt{K^2 + 2KJ_\perp}$.

According to the Stoner-Wohlfarth model [20], for the $x = 0$ sample with the spin-flip transition, $|SJ_\perp| = g\mu_B H_c/z$ and $|SK| = g\mu_B(H_{ab} - 2H_c)/2$, where $H_{ab} = 1.2$ T is the field for the Mn1 spins to saturate along the ab plane and $H_c = 0.14$ T is the spin-flip field along the c axis, $g = 2$, $S = 5/2$ and $z = 2$ is the number of nearest Mn interlayer neighbors. The calculated $|SK| = 0.053$ meV and $|SJ_\perp| = 0.008$ meV. So, we conclude that our materials are in the regime where $K^2 \gg J_\perp^2$., where the ordering temperature (T_N or T_C) can be approximated as

$$T_c \approx \frac{a|J|}{b + \log(J/K)} \tag{4.3}$$

So T_c is only controlled by J and K, which characterize the intralayer magnetic dynamics. Specifically, T_c depends logarithmically weakly on the ratio of J/K. Thus, the ordering temperature is expected to be weakly pressure dependent, with maybe a tiny notch right at the triple point where $J_\perp$ is fully compensated. Indeed, in our experiment, T_N or T_C varies little in the entire set of experiments, between ~ 11 K and ~ 15 K.

Therefore, as a material system in the $K^2 \gg J_\perp^2$ regime, although the sign of $J_\perp$ defines the long-range order in the c direction, the ordering temperature depends logarithmically weakly on J/K. Consequently, neither T_N nor T_C is sensitive to the external pressures we applied (only up to 2 GPa) and is oblivious to the metamagnetic transitions under pressure.

Let us now turn to the pressure dependence of the metamagnetic transition. To understand it, we observe that a FM ordered Mn1 plane induces an exchange bias field H_{ex} in a magnetically disordered Mn3 layer. Assuming that the magnetic susceptibility of the latter is $\chi_3(T)$, we can add the fourth term to the Hamiltonian in Eq. 4.1, namely

$$H_{13} = \pm\chi_3(T)H_{ex}^2, \tag{4.4}$$

where the plus sign corresponds to AFM stacking of the Mn1 plane, and the minus to the FM stacking. Obviously, this Mn3-mediated interaction is always ferromagnetic, and competes with the standard Mn1-Mn1 superexchange [60].

Let us now estimate the pressure dependence of both interlayer terms using a simple Hubbard model. To this end, we consider two possible exchange paths. One is the "standard" superexchange, when an electron virtually hops from the effective Mn1 layer (which includes the entire pink region in Fig. 4.1(a)) to anions in the effective Mn3 layer (Bi, Sb or Te), and then to the next Mn1 layer. We will assign to Mn one effective d level, E_d, and to all anions one effective p level, E_p, with the charge transfer energy $\Delta E = E_d - E_p$, and a Hubbard repulsion U. The second exchange path is from the effective Mn1 to individual Mn3 ions. Importantly, E_p, E_d and U are atomic parameters and are not sensitive to pressure. On the contrary, the hopping amplitudes, t_{pd} for the former path and t_{dd} for the latter are very sensitive to the interlayer distance.

The first path defines the standard AFM superexchange,

$$J_{\perp}^{afm} \propto t_{pd}^4/\Delta E^2 U. \tag{4.5}$$

The second determines the exchange bias parameter in Eq. 4.4,

$$H_{ex} \propto t_{dd}. \tag{4.6}$$

Per Eq. 4.4, this generates

$$J_{\perp}^{fm} \propto t_{dd}^2 \chi_3(T). \tag{4.7}$$

Note that the same conclusion can be achieved by diagonalizing a three site Hubbard model with half-filling under an assumption that all sites have the same U and hopping $t_{12} = t_{13} = t_{dd}$.

Therefore, while both $J_{\perp}^{afm}$ and $J_{\perp}^{fm}$ are expected to increase with pressure, the former grows as the forth power of the effective hopping, and the latter only as the second power, making the AFM more favored under pressure. Since T_{M1} or T_{M2} is defined by $J_{\perp}$ (the transition occurs when it is fully compensated, $J_{\perp} = 0$), it is very sensitive to pressure because the AFM part grows much faster with pressure.

The most intriguing part is the exotic temperature dependence of the metamagnetic transition, with at least one concentration ($x = 0.67$) with the recurrent behavior. In order to understand that, recall that the only temperature-dependent parameter in Eqs. 4.5 and 4.7 is $\chi_3(T)$. Let us estimate its temperature dependence. For small doping levels we can neglect the internal interactions inside the Mn3 layer, so that $\chi_3(T)$ is described by the Curie law, $\chi_3(T) \propto 1/T$. At higher concentrations it is reasonable to assume (and this is also supported by neutron data) that the interactions in the Mn3 layer are random in sign and amplitude [60], so on the mean field level they would freeze into a spin glass state with the net magnetization $\langle M_3 \rangle = 0$. While fluctuations beyond the mean field can completely destroy the spin-glass transition, or drive it to extremely low temperatures, the magnetic susceptibility of such systems would behave similar to that in a usual antiferromagnet. That is to say, the susceptibility will decay at high T as $\chi_3(T) \propto 1/(T + T_{CW})$ (we are using the convention where $T_{CW} > 0$ for the antiferromagnetic response), and has a maximum at some temperature $T_0 < T_{CW}$, and T_{CW} is on the order of the average interaction strength in the Mn3 plane. A typical $\chi_3(T)$ is shown in Fig. 4.4(f), where the approximate behavior of $\chi_3(T)$ for $T_{CW} = 3$, 7 and 15 is plotted (in arbitrary units). Note that T_{CW} is growing with the concentration, first very weakly, then rapidly. Therefore the temperature range of interest (the shaded region in Fig. 4.4) may fall either entirely in the range of $\chi_3(T)$ decreasing with temperature (small concentration of Mn3), or entirely in the range of increasing $\chi_3(T)$ (large concentrations), or even span both regimes (intermediate concentrations).

Now we summarize the microscopic explanation of all nontrivial behaviors we observed. For $x = 0$, the Mn3 concentration is very low, so $J_\perp^{afm} > J_\perp^{fm}$ holds below T_N for all pressures. For $x = 0.48$ and 0.57, the relatively larger Mn3 concentration (still low concentration case) makes $J_\perp^{fm}$ strong enough to compete with $J_\perp^{afm}$. Since χ_3 and thus $J_\perp^{fm}$ increase upon cooling, below the ordering temperature, an AFM to FM transition appears at T_{M1}. Upon compressing, $J_\perp^{afm}$ increases faster than $J_\perp^{fm}$, so T_{M1} decreases with pressure. For $x = 0.67$ (intermediate concentration case), at low pressures, $J_\perp^{fm} > J_\perp^{afm}$ holds for $T < T_C$. But above a threshold pressure, $J_\perp^{afm}$ is favored over $J_\perp^{fm}$ at T_N. Then upon cooling, χ_3 and $J_\perp^{fm}$

first rise and then decrease, so an AFM to FM transition appears at T_{M1} and then a FM to AFM transition shows up at T_{M2}. Finally, with increasing pressure, the faster growing $J_{\perp}^{afm}$ leads to decreasing T_{M1} and increasing T_{M2}. For $x = 0.76$, χ_3 decreases upon cooling (large concentration case), as well as $J_{\perp}^{fm}$. Therefore the FM to AFM transition occurs at $T_{M2} < T_C$. With increasing pressure, $J_{\perp}^{afm}$ grows faster, thus T_{M2} increases with pressure.

4.4 Summary and outlook

In summary, in $Mn(Bi_{1-x}Sb_x)_4Te_7$ where the antiferromagnetic superexchange interaction through anions and the Mn3-mediated ferromagnetic exchange interaction compete, we discover rare pressure-activated metamagnetic transitions with non-trivial pressure- and temperature- dependence and even re-entrance. These unconventional behaviors are attributed to the distinct pressure and temperature dependence of the two competing interlayer exchange interactions. Moreover, we find the pressure effect on the ordering temperature from the PM to ordered state is weak, which we further show to be due to its logarithmically weakly dependence on the ratio of the intralayer coupling and magnetic anisotropy. Therefore, our study provides independent probing of the interlayer coupling, intralayer coupling and magnetic anisotropy and the role that they play in van der Waals magnetism.

CHAPTER 5

Single crystal growth, chemical defects, magnetic and transport properties of antiferromagnetic topological insulators $(Ge_{1-\delta-x}Mn_x)_2Bi_2Te_5$ $(x \leq 0.47,\ 0.11 \leq \delta \leq 0.20)$

The majority of this chapter has been adapted from [95]. This work was done in collaboration with Dr. Huibo Cao from Oak Ridge National Lab for single crystal neutron diffraction measurement.

5.1 Introduction

The discovery of magnetic topological insulators (TIs) marks an important breakthrough in condensed matter physics in the past decade. When magnetism is introduced in TIs and breaks the time-reversal symmetry that protects the gapless Dirac surface states, a gapped surface state and dissipationless quantized edge conduction may appear. Therefore magnetic TIs can host a set of emergent phenomena such as quantum anomalous Hall effect, Axion insulating state and quantum magnetoelectric effect [3, 22, 96, 97]. Among the magnetic TIs, $MnBi_{2n}Te_{3n+1}$ family with alternating $[MnBi_2Te_4]$ septuple layer (SL), and $(n-1)[Bi_2Te_3]$ quintuple layer (QL) is the first family that hosts intrinsic magnetism rather than introduced by doping [23, 29, 32, 42–46, 49, 51, 53–55, 98–103]. $MnBi_{2n}Te_{3n+1}$ goes from an A-type antiferromagnetic (AFM) state ($n \leq 3$) to a ferromagnetic state ($n \geq 4$), with magnetic moment pointing out-of-plane. The van der Waals nature makes it easy to exfoliate a bulk crystal into a thin-film device, in which quantized anomalous Hall conductance [24, 47] and electric-field tuned Layer Hall effect [25] are experimentally achieved in odd-layer and even-layer

$MnBi_2Te_4$ devices, respectively.

The discovery of $MnBi_{2n}Te_{3n+1}$ was inspired by the existence of the nonmagnetic $XBi_{2n}Te_{3n+1}$ (X = Ge, Sn, Pb) series which have already been synthesized for decades [104]. $XBi_{2n}Te_{3n+1}$ are previously known thermoelectric materials, and recently attracted research interest due to their non-trivial band topology [27, 68, 105]. When nonmagnetic X atoms are replaced by Mn, the quasi-metastable $MnBi_{2n}Te_{3n+1}$ compounds can be made in a very narrow temperature region [31]. To the XTe-rich end of the XTe-Bi_2Te_3 phase diagram, besides $XBi_{2n}Te_{3n+1}$, thicker layered structures with more X in one building block exist. For example, $X_2Bi_2Te_5$ (X = Ge, Sn, Pb), abbreviated as the 225 phase, is made of nonuple layers (NL) while $X_3Bi_2Te_6$ (X = Ge, Sn, Pb) phase consists of undecuple layers [104, 106–108]. The NL of $X_2Bi_2Te_5$ can be seen as inserting an additional XTe layer into XBi_2Te_4 SL, as shown in Fig. 1(a). Given the close structural correspondence between $MnBi_2Te_4$ and XBi_2Te_4, one may suspect $Mn_2Bi_2Te_5$ (Mn225) and $Mn_3Bi_2Te_6$ to exist, being potential candidates of intrinsic magnetic topological insulators. Indeed theoretical calculation has indicated Mn225 to be an intrinsic magnetic topological insulator that could host dynamical axion field [109–113]. However, the successful growth of pure Mn225 phase is very challenging, hindering the investigation of its intrinsic physical properties [114, 115]. For example, only a few layers of Mn225 phase were found embedded inside the $MnBi_2Te_4$ pieces in chemical vapor transport (CVT) growths while the Mn225 single crystals obtained via the self-flux growth might show significant contamination from the $MnBi_2Te_4$ phase.

In this chapter, I will introduce the growth, crystal and magnetic structures, as well as the transport and thermodynamic properties of high quality $(Ge_{1-\delta-x}Mn_x)_2Bi_2Te_5$ ($x \leq 0.47$, $0.11 \leq \delta \leq 0.20$) single crystals. While our attempt to grow pure Mn225 single crystals is not successful using both the CVT and flux growth methods, pure $(Ge_{1-\delta})_2Bi_2Te_5$ (Ge225) single crystals were made by the flux method using Te as the self flux while $(Ge_{1-\delta-x}Mn_x)_2Bi_2Te_5$ (GeMn225) with $x \leq 0.47$ can be grown by the CVT method [114, 116]. I will show that wavelength-dispersive X- ray spectroscopy (WDS) measurements as well as the refinements of the powder X-ray diffraction (PXRD) and single-crystal neutron diffraction data indicate

the presence of significant Ge vacancies of $0.11 \leq \delta \leq 0.20$, leading to holes dominating the electrical transport. We find that GeMn225 shows a $T_N = 10.8$ K at $x = 0.47$ with a spin flop transition at 2.0 T when $H \parallel c$. Our neutron analysis of the $x = 0.47$ compound suggests negligible amount of Mn_{Bi} antisite formation and a bilayer A-type AFM with a refined Mn moment of 3.0(3) μ_B at 5 K.

5.2 Experimental methods

Ge225 single crystals were grown using the self-flux method with Te as the flux. Ge chunks, Bi chunks and Te chunks were mixed at the ratio of Ge : Bi : Te = 2 : 2 : 8 in an alumina crucible and sealed in an evacuated quartz tube. The ampule was first heated to 1000 °C overnight, then quickly cooled to 600 °C before it was slowly cooled to 520 °C in 3 days. At last, single crystals were separated from the flux by a centrifuge. Large and shiny mm-sized single crystals were obtained using this method.

Our flux-growth trials of the Mn-doping series using Te self flux did not yield the 225 phase. However, our CVT growth trials using MnI_2 as the transport agent resulted in high quality GeMn225 single crystals. Mn pieces, Ge chunks, Bi chunks, Te chunks and I_2 pieces were mixed at the ratio given in Table I, loaded and sealed in a quartz tube under vacuum. The tube was placed vertically in a box furnace and slowly heated to 1000 °C overnight. It was then moved to a horizontal tube furnace where the low-temperature and high-temperature were set to be 520°C and 540°C, with the starting material on the high-temperature end. The cold-end temperature was selected as 520 °C since it was the synthesis temperature reported for pure Ge225 in solid-state reaction [106]. After two weeks, GeMn225 single crystals were taken out and rinsed with distilled water to remove the iodide impurities.

To identify the pieces of the 225 phase, (0 0 L) reflections were collected on both the top and bottom surfaces of single crystals using a PANalytical Empyrean diffractometer equipped with Cu Kα radiation. Following this, we performed PXRD for further impurity checking and structural refinement. Then WDS measurements were conducted to obtain the elemental

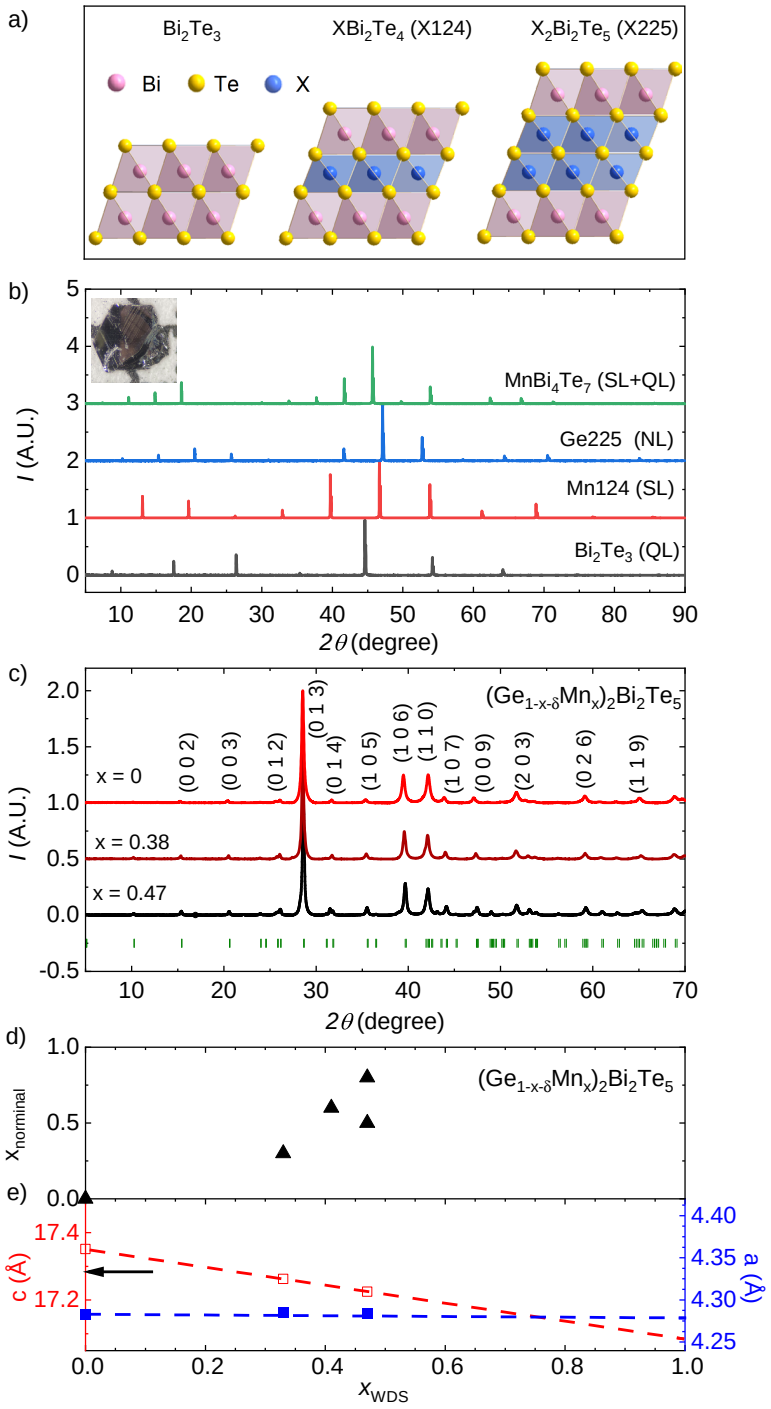

Figure 5.1: (a) Crystal structures of Bi_2Te_3 QL, XBi_2Te_4 SL and $X_2Bi_2Te_5$ NL. (b) (0 0 L) Bragg peaks of different X-Bi-Te series. Inset: an as-grown hexagonal single crystal of GeMn225 ($x = 0.47$) against a mm-grid. (c) PXRD of $(Ge_{1-\delta-x}Mn_x)_2Bi_2Te_5$. (d) $x_{nominal}$ vs. x_{WDS} when growing GeMn225. (e) Lattice parameters a and c of $(Ge_{1-\delta-x}Mn_x)_2Bi_2Te_5$, dashed line shows the linear fit of lattice parameters.

Table 5.1: Summary of the $(Ge_{1-\delta-x}Mn_x)_2Bi_2Te_5$ series. All doped compounds are grown by the CVT method with MnI_2 as the transport agent while the parent compound is made by the flux method as discussed in the text. *: the ratio of $Ge_{1-x}Mn_xTe$: Bi_2Te_3 : MnI_2. a and c are the lattice parameters. T_N is the AFM transition temperature. p_1 is the charge carrier density calculated from Hall measurements via $p_1 = B/e\rho_{yx}$, p_2 is the charge carrier density estimated by $p_2 = 2\delta/A$, where A is the unit cell volume in cm^3. Both p_1 and p_2 has the unit of $\times 10^{20} cm^{-3}$

$x_{nominal}$	ratio*	WDS	x	δ	a (Å)	c (Å)	T_N (K)	p_1	p_2
0	(Flux)	$Ge_{1.59(3)}Bi_{1.94(2)}Te_5$	0	0.20(2)	4.28	17.35	NA	9.2	29
0.3	2:1:1	$Mn_{0.65(1)}Ge_{1.07(1)}Bi_{1.99(2)}Te_5$	0.33(1)	0.14(1)	4.28	17.26	6.0	4.7	17
0.5	2:1:1	$Mn_{0.94(1)}Ge_{0.82(3)}Bi_{2.02(2)}Te_5$	0.47(1)	0.12(2)	4.28	17.22	10.8	1.6	13
0.6	3:1:1	$Mn_{0.83(1)}Ge_{0.93(2)}Bi_{1.99(2)}Te_5$	0.41(1)	0.12(1)	4.28	17.22	10.0		
0.8	5:1:1	$Mn_{0.94(3)}Ge_{0.85(1)}Bi_{1.99(2)}Te_5$	0.47(1)	0.11(2)	4.28	17.23	11.0		

analysis of the samples, specifically the Mn level x. Magnetization data were collected in a Quantum Design (QD) Magnetic Properties Measurement System (MPMS). Specific heat and electrical transport measurements were made inside a QD DynaCool Physical Properties Measurement System (PPMS). Electrical contacts were made to the sample using Dupont 4922N silver paste to attach Pt wires in a six-probe configuration. To eliminate unwanted contributions from mixed transport channels, electrical resistivity (ρ_{xx}) and Hall (ρ_{yx}) data were collected while sweeping the magnetic field from -9 T to 9 T. The data were then symmetrized to obtain $\rho_{xx}(H)$ using $\rho_{xx}(H) = (\rho_{xx}(H) + \rho_{xx}(-H))/2$ and antisymmetrized to get $\rho_{yx}(H)$ using $\rho_{yx}(H) = (\rho_{yx}(H) - \rho_{yx}(-H))/2$. The magnetoresistance is defined as MR $= (\rho_{xx}(H) - \rho_{xx}(0))/\rho_{xx}(0)$. In our measurement geometry, the positive slope of $\rho_{yx}(H)$ suggests hole carriers dominate the transport. Single-crystal neutron diffraction was performed for the $x = 0.47$ sample at 5 K and 0 T on the HB-3A DEMAND single-crystal neutron diffractometer located at Oak Ridge National Laboratory [37]. Both the neutron and X-ray diffraction data were refined using the Fullprof suit [38].

5.3 Experimental Results

5.3.1 Growth optimization and phase characterization

Our CVT growth trials of the GeMn225 phase started with an elemental ratio such that XTe : Bi_2Te_3 : MnI_2 = m : 1 : 1, where X = $(Ge_{1-x}Mn_x)$. As we increased the Mn concentration in X, higher m for extra XTe became necessary to yield the 225 phase. Our optimal trials that gave high quality GeMn225 single crystals are listed in Table 5.1. Ge225 and GeMn225 crystals can grow up to a lateral size of several mm with a thickness about a hundred micron in two weeks. All crystals obtained from the CVT growth process exhibit a hexagonal-plate shape, with clearly defined edges indicating the as-grown a and b axes. In the inset of Fig. 5.1 (b), an image of a $(Mn_{0.47}Ge_{0.41})_2Bi_2Te_5$ single crystal against the mm-grid is shown .

The GeMn225 phase was first confirmed by checking the (0 0 L) reflections in the surface XRD patterns. Because the (0 0 L) spectrum depends solely on the periodic unit along c axis, *i.e.*, the thickness of the NL layer, it can be well distinguished from that of [$MnBi_2Te_4$] SL, [Bi_2Te_3] QL or their combinations. A comparison of the (0 0 L) reflections of various materials is shown in Fig. 5.1(b), revealing the increasing thickness of the repeating layer(s) from QL, SL, NL to QL+SL. The PXRD patterns are shown and indexed in Fig. 5.1(c). No clear impurity phases were identified.

The Mn doping levels obtained via the WDS measurements are summarized in Table I. These values suggest the highest doping level of Mn remains to be around $x = 0.47$ in GeMn225 despite the nominal x in the starting materials being much higher than 0.47. Based on the experience stated above, we also attempted pure Mn225 growth with extra MnTe. High-m trials such as Mn : Bi : Te : I = 11 : 2 : 13 : 2 at various growth temperatures yield only $MnBi_2Te_4$ and/or Bi_2Te_3. Via both flux and CVT methods, we were unable to obtain pure Mn225 single crystals. So for this GeMn225 phase to appear stably in CVT growth, we conclude that there exists a substitution limit of Mn on Ge as indicated in Fig. 5.1(d).

The refined lattice parameters a and c are plotted in Fig. 5.1(e) against the x values

that are determined by WDS. The lattice parameter a remains almost unchanged while the lattice parameter c decreases by 0.8% from $x = 0$ to $x = 0.47$. Assuming the Vegard's law, the extrapolation of the lattice parameters with x allows us to predict the lattice parameters for pure Mn225. The data suggest Mn225 has $a = 4.27\mathring{A}$ and $c = 17.1\mathring{A}$, which is consistent with the previous report [115].

5.3.2 Magnetic and Transport properties of $(Ge_{1-\delta-x}Mn_x)_2Bi_2Te_5$ single crystals

To investigate the effect of Mn doping, we conducted thermodynamic and transport measurements. The Mn concentrations measured via WDS are utilized in the analysis of the magnetic and specific heat data and will be referenced throughout this chapter. In Fig. 5.2 (a), the temperature-dependent magnetic susceptibility, $\chi(T)$, measured at 0.1 T, reveals a kink feature at 6.0 K and 10.8 K for the $x = 0.33$ and $x = 0.47$ samples, respectively, indicating magnetic ordering at low temperatures. As the temperature decreases, $\chi(T)$ continues to rise below the ordering temperature for $H \parallel ab$, while it decreases for $H \parallel c$, indicating AFM ordering with the easy axis along the c direction. The Curie-Weiss fit of the inverse susceptibility measured at 1 T (inset of Fig. 5.2 (a)) yields a Curie temperature of -12 K that suggests strong in-plane ferromagnetic fluctuation and an effective moment of 6.0 μ_B/Mn that is consistent with Mn^{2+}'s effective moment. Figure 5.2 (b) presents the normalized temperature-dependent longitudinal resistivity with the current along the ab plane, $\rho_{xx}(T)/\rho_{xx}(2\text{ K})$. While the resistivity in the undoped one exhibits a monotonic decrease upon cooling, the sharp drop in resistivity for the $x = 0.33$ and 0.47 samples suggests suppressed spin scattering upon entering the ordered state, implying parallel in-plane spin alignment. The inset of Fig. 5.2 (b) presents the specific heat data of the $x = 0.47$ compound, revealing an anomaly associates with the AFM transition emerging at 10.8 K, in line with other measurements.

The evolution of magnetism under external fields and its coupling with charge carriers are presented in Fig. 5.3. Figure 5.3 (a) shows their isothermal magnetization for $H \parallel c$. While both curves exhibit AFM behavior, a clear spin-flop transition feature appears in the

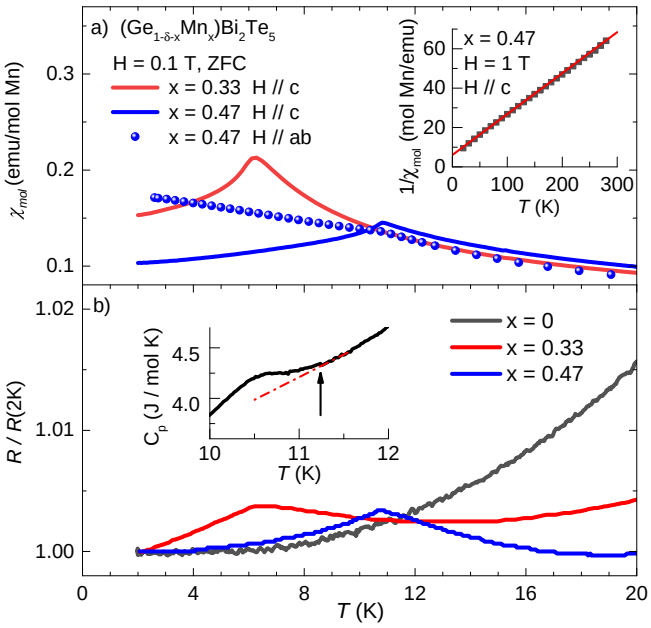

Figure 5.2: Thermodynamic and transport properties of GeMn225. (a) Temperature dependent magnetic susceptibility under 0.1 T for different doping levels and direction. Inset: inverse magnetic susceptibility measured at 1 T above T_N. Curie-Weiss fit is shown in solid line. (b) Normalized temperature-dependent electrical resistivity with current along the ab plane for different doping levels. Inset: temperature-dependence of specific heat of the $x = 0.47$ sample with the criterion to determine T_N.

$x = 0.47$ sample at about $H_{sf} = 2.0$ T. This value is lower than that of 3.3 T in $MnBi_2Te_4$, yet significantly higher than the 0.2 T observed in $MnBi_4Te_7$. No sign of spin-flop transition is observed for $H \parallel ab$ (Fig. 5.3 (b)), indicating the c-axis as the easy axis. Magnetization in both doped samples is about 1.8 μ_B/Mn at 7 T. For the $x = 0.47$ sample, M reaches to 2.4 μ_B/Mn at 14 T with no sign of saturation, as shown in Fig. 5.3(b). This value is less than half of the expected Mn moment of 5 μ_B/Mn, suggesting that the saturation field is much higher than 14 T.

Figures 5.3 (c) and (d) depict the MR data. The MR of the $x = 0$ sample exhibits a parabolic field dependence while it peaks at $H_{sf} = 0.7$ T and $H_{sf} = 2.0$ T for the $x = 0.33$ and 0.47 compounds, respectively. Above H_{sf}, the MR displays a negative slope as the

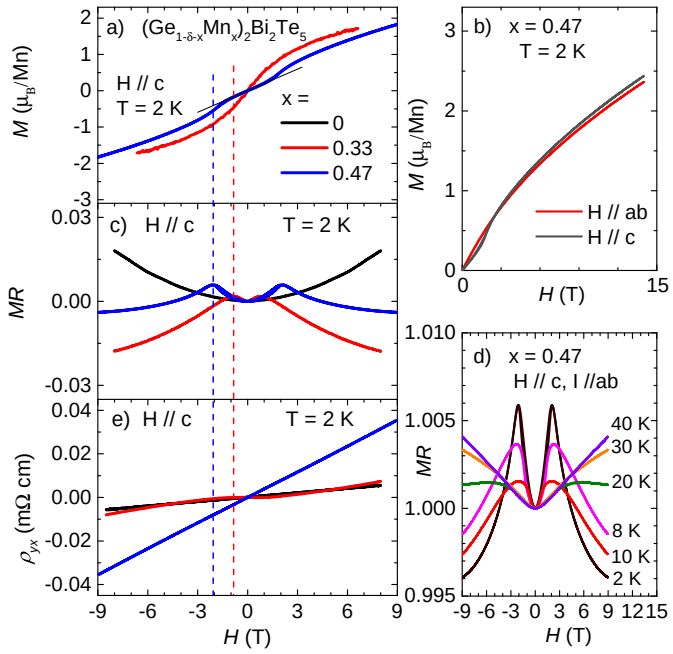

Figure 5.3: (a) Isothermal magnetization at 2 K of GeMn225 with $H \parallel c$. (b) Isothermal magnetization measured at 2 K up to 14 T for the $x = 0.47$ sample with $H \parallel ab$ and $H \parallel c$. (c) Field-dependence of MR of GeMn225. (d) MR at various temperatures for the $x = 0.47$ sample. (e) Field-dependence of Hall resistivity. Dotted lines refer to H_{sf} in the $x = 0.33$ and 0.47 samples.

spin disorder scattering gradually diminishes with increasing field. This negative slope in MR persists at elevated temperatures up to 30 K, as illustrated in Fig. 5.3 (d), suggesting significant spin fluctuation above the ordering temperature in this doping series. Figure 5.3 (e) presents the field-dependent Hall resistivity. Its positive slope with magnetic field suggests holes dominate the transport. The carrier concentrations are in the order of 10^{20} cm^{-3} and decrease with higher Mn doping, as summarized in Table I. This is in sharp contrast with the previous report on Mn225 where electrons dominate the transport [115].

5.3.3 Crystal and Magnetic Structure

If free of defects, the stoichiometry of Ge : Bi : Te would be 2 : 2 : 5 for Ge225. However, as indicated in Table I, WDS measurements reveal a deficiency of Ge, with only 1.59 Ge atoms present in Ge225. Meanwhile, a (Ge+Mn) deficiency in Mn-doped samples also exists, where (Ge+Mn) $\sim$ 1.7. In order to better understand the crystal and magnetic structure of this family, particularly regrading the types of defects present and the specific sites where Mn is doped, we have performed both single crystal neutron diffraction for the $x = 0.47$ sample and PXRD for the Ge225 sample. The $2d$ and $2c$ sites are where (Mn/Ge/Bi) cations can reside, forming four cation layers. In each NL, atoms on the $2d$ site make the inner two cation layers, while those on the $2c$ site constitute the outer two cation layers.

5.3.3.1 Magnetic structure revealed through Neutron Diffraction Analysis

Since neutron diffraction is quite sensitive to Mn atoms in the Mn-Bi-Te systems due to the negative scattering length of Mn [29, 30], we first measure the $x = 0.47$ crystal using neutron diffraction to determine the magnetic structure and whether Mn is doped onto the $2d$ or $2c$ site.

No additional Bragg peaks are observed below T_N, indicating a magnetic propagation vector of (0 0 0). The right inset of Fig. 4 shows the intensity of the (0 1 0) and (0 0 4) peaks below and above T_N. Upon entering the ordered state, the (0 1 0) peak increases, indicating formation of spin order perpendicular to b axis. An unchanged intensity in (0 0

4) peak, on the other hand, indicates likely no spin component perpendicular to c axis. This points to an easy axis along c axis without spin tilting, consistent with our magnetic property measurements. So given its AFM nature and the crystal space group $P\bar{3}m1$ (No. 164), the highest magnetic symmetry $P\bar{3}'m'1$ with the ordered moment along c can be concluded and used to fit the collected neutron data. Because Ge and Bi have similar scattering lengths for neutrons, it is difficult to differentiate Ge and Bi on the same site. For simplicity, in our refinement, we assume Ge and Bi each occupy either $2d$ or $2c$ site, with our primary focus being on Mn distributions. Note in reality Ge and Bi mixing is expected, which we will discuss later through X-ray diffraction analysis. We examine three possible scenarios, stacking A with Mn on the $2d$ site, stacking B with Mn on the $2c$ site, and a mixed stacking where Mn can go into either site (Table A1 - A3) (Appendix A). In all three scenarios, we refine the occupancy of Ge and Mn, as well as the moment of Mn. Our refinement demonstrates that the scenario where all Mn atoms reside on the $2d$ site yields the highest goodness-of-fit value. Therefore, within the resolution of our measurement, we conclude that Mn is doped onto the $2d$ site, with Mn residing on the inner two layers, as shown in the left inset of Fig. 4. Our refinement indicates parallel alignment of spins within the ab plane, with spins in adjacent layers being antiparallel to each other (Appendix A).

5.3.3.2 Vacancies and Bi/Ge site mixing in Ge225

According to the WDS measurements, Ge225 samples may exhibit vacancies. If we assume the presence of vacancies and Bi/Ge site mixing, we can write down:

$$f_{2d} = \mathrm{Ge}_{2d}^{occ} f_{Ge} + \mathrm{Bi}_{2d}^{occ} f_{Bi} + V_{2d} \times 0 \tag{5.1}$$

$$f_{2c} = \mathrm{Ge}_{2c}^{occ} f_{Ge} + \mathrm{Bi}_{2c}^{occ} f_{Bi} + V_{2c} \times 0. \tag{5.2}$$

Here, f is the atomic scattering factor, ^{occ} refers to the element occupancy, V is the amount of vacancy.

Two extreme structural models are used on powder XRD to obtain f_{2d} and f_{2c}. In model 1, Ge occupies both $2d$ and $2c$ sites while in model 2, Bi occupies both. The refinements

Table 5.2: Refined crystal structural parameters for the parent compound Ge225 based on the PXRD data measured at 300 K. The refinement is constrained by the WDS result. Number of reflections: 6474; $R_F = 8.42\%$; $\chi^2 = 46.4$.

Atom	site	x	y	z	occ.
Ge1	$2d$	1/3	2/3	0.1043(3)	0.640(6)
Bi1	$2d$	1/3	2/3	0.1043(3)	0.361(6)
Ge2	$2c$	0	0	0.3260(2)	0.161(6)
Bi2	$2c$	0	0	0.3260(2)	0.639(6)
Te1	$1a$	0	0	0	1
Te2	$2d$	1/3	2/3	0.2037(3)	1
Te3	$2d$	1/3	2/3	0.4243(2)	1

Table 5.3: Refined magnetic and crystal structural parameters for the x =0.47 sample based on the single crystal neutron diffraction measurement at 5 K constrained by WDS result. Number of reflections: 38; $R_F = 12.8\%$; $\chi^2 = 7.12$.

Atom	site	x	y	z	occ.	Moment at 5 K
Ge1	2d	1/3	2/3	0.099(6)	0.17	
Mn1	2d	1/3	2/3	0.099(6)	0.47	3.0(3) μ_B/Mn
Bi1	2d	1/3	2/3	0.099(6)	0.36	
Ge2	2c	0	0	0.316(2)	0.23	
Bi2	2c	0	0	0.316(2)	0.64	
Te1	1a	0	0	0	1	
Te2	2d	1/3	2/3	0.792(3)	1	
Te3	2d	1/3	2/3	0.426(3)	1	

show that in model 1, Ge_{2d}^{occ1} and Ge_{2c}^{occ1} equals 1.59 and 1.79, and in model 2, Bi_{2d}^{occ2} and Bi_{2c}^{occ2} equals 0.58 and 0.66 (Appendix A). Since regardless of the occupancy model employed, the scattering cross section of an individual site should be the same, we can write down:

$$\text{Site } 2d : f_{2d} = 1.59 f_{Ge} = 0.58 f_{Bi} \tag{5.3}$$

$$\text{Site } 2c : f_{2c} = 1.79 f_{Ge} = 0.66 f_{Bi}, \tag{5.4}$$

which lead to $f_{Bi}/f_{Ge} = 2.7$. This number is close to the atomic number ratio between Bi and Ge, 2.6. By plugging this ratio into Eq. (1), we obtain :

$$\mathrm{Ge}_{2d}^{occ} + 2.7\mathrm{Bi}_{2d}^{occ} = 1.59 \tag{5.5}$$

By plugging the ratio into Eq. (2) and with $\mathrm{Ge}_{2c}^{occ} = 1 - V_{Ge} - \mathrm{Ge}_{2d}^{occ}$ and $\mathrm{Bi}_{2c}^{occ} = 1 - V_{Bi} - \mathrm{Bi}_{2d}^{occ}$ where V_{Ge} and V_{Bi} refer to the amount of vacancies for Ge or Bi, we get:

$$(1 - V_{Ge} - \mathrm{Ge}_{2d}^{occ}) + 2.7(1 - V_{Bi} - \mathrm{Bi}_{2d}^{occ}) = 1.79, \tag{5.6}$$

From Eqs. (5) and (6), we get :

$$V_{Ge} + 2.7 V_{Bi} = 0.32 \tag{5.7}$$

Therefore, PXRD also suggests vacancies in the compound. WDS measurements show V_{Ge} to be 0.20(2) and V_{Bi} is 0.03(1), which is consistent with Eq. (7).

Utilizing the aforementioned constraint and with the total amount of Ge and Bi set to their WDS values, the occupancy of Ge and Bi on each site is refined. The refinement returns the same goodnss-of-fit when assuming all vacancies on the $2d$ site (Table A6), $2c$ site (Table II), or distributed on both $2d$ and $2c$ sites (Table A7) (Appendix A). Based on the refinement of our neutron diffraction data, which suggests that Mn is doped on the $2d$ site, and considering the WDS measurements indicating that Mn atoms solely substitute Ge atoms, it is reasonable to infer that most Ge atoms occupy the $2d$ site. Our refinement shows that Ge atoms predominantly occupy site $2d$ when vacancies concentrate on site $2c$. The refined crystal structure is thus finalized in Table II.

Table 5.4: Comparison in Mn-Bi-Te family. SJ_c is the interlayer exchange coupling per Mn and SK is the uniaxial magnetic anisotropy. L_1 and L_2 refer to the nearest-neighbor Mn-Mn interlayer distances shown in Fig. 5.5 (b). α and β are the bond angles of the distorted $MnTe_6$ octahedron shown in the inset of Fig 5.5 (c).

Component	SJ_{c1} (meV)	SK (meV)	L_1 (Å)	L_2 (Å)	α (°)	β (°)
$(Mn_{0.47}Ge_{0.41})_2Bi_2Te_5$	1.8	0.008	13.96	4.39	86.7/90.5	52.4/55.1
$(Mn_{0.6}Pb_{0.4})Bi_2Te_4$ [41]	0.24	0.03	13.93	4.53	93.5	57.3
$MnBi_2Te_4$ [62]	0.26	0.09	13.64	4.51	93.5	57.3
$MnBi_4Te_7$ [28]	0.03	0.10	23.71		93.5	57.3
$MnBi_6Te_{10}$ [28]	0.01	0.10	34.00		93.2	57.0

5.3.3.3 Neutron Refinement of the $x = 0.47$ Sample

With a better understanding of the crystal structure of Ge225, we turn back to the neutron diffraction data to work out the crystal and magnetic structure for the doped sample. Now we force the WDS values of Mn with Mn only replacing Ge on site $2d$, and set the distribution of Bi on both sites identical to that of the parent compound with all vacancies concentrating on site $2c$. The refined structure is shown in Table III. The ordered Mn moment at 5 K is refined to be 3.0(3) μ_B.

Figure 5.4 shows the magnetic order parameter, measured on the (0 1 1) refection up to 15 K for $(Mn_{0.47}Ge_{0.41})_2Bi_2Te_5$. The solid line represents the fit to the mean-field power-law,

$$I = A\left(\frac{T_N - T}{T_N}\right)^{2\beta} + B \tag{5.8}$$

where A is a constant, B is the background and β is the order parameter critical exponent. The best fit yields a Neél temperature of $T_N = 9.5$ K and a critical exponent of $\beta = 0.32(7)$, which is similar to that of $MnBi_2Te_4$ [29]. Based on the fitting, we estimate the ordered moment at 0 K to be 4.5(7) μ_B per Mn, close to the expected value for Mn^{2+}.

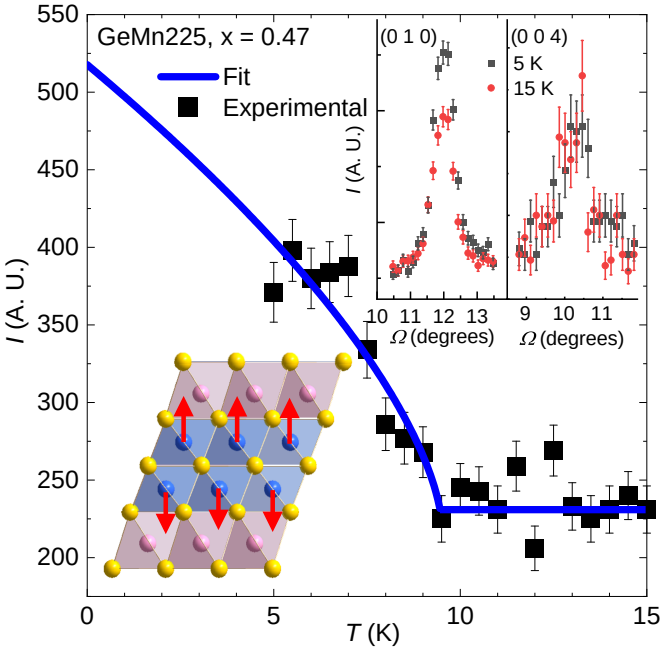

Figure 5.4: Magnetic order parameter at magnetic reflection (0 1 1) for the $x = 0.47$ sample measured at DEMAND. The blue line depicts the best fit using the mean-field power law, see text. Left inset: the magnetic structure. Right inset: the intensity of the (0 1 0) and (0 0 4) peak above and below T_N.

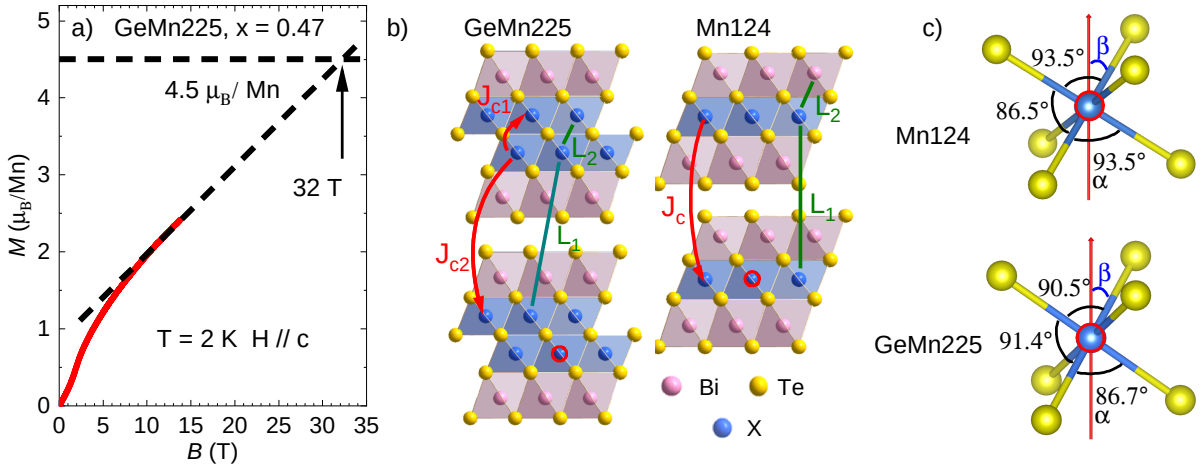

Figure 5.5: (a) Isothermal magnetization of the $x = 0.47$ sample at 2 K. The red line is the experimental curve and the black dashed line is a linear extrapolation of the magnetization at 2 K, it reaches to 4.5 μ_B/Mn at around 30 T. (b) Crystal structure of X225 (X = GeMn) and X124 (X = Mn). The superexchanges are indicated with red arrows, the nearest-neighbor Mn-Mn distances are highlighted with olive lines. (c) Distorted $MnTe_6$ octahedron, the building blocks of the magnetic layer in the 124 and 225 phases. The Mn atom in the center refers to the circled one in (b). Different Te-Mn-Te bond angels are shown, the asymmetry in GeMn225 arises from its asymmetric next-nearest-neighbor environment.

5.4 Discussion

The presence of vacancies has profound impact in the transport properties of the 225 compounds. Research on Mn-Bi-Te systems indicates that defect-free compounds are charge-neutral, with carriers in actual samples being contributed by various defects [63]. Mainly, electron carriers are contributed by $\mathrm{Bi}_{Mn/Ge}$ and Te vacancies, whereas hole carriers are contributed by $(\mathrm{Mn/Ge})_{Bi}$ and cation vacancies. This can be seen in the following defect chemistry for native Ge225:

$$Ge_2Bi_2Te_5 \rightleftharpoons Ge'_{Bi} + h^{\bullet} + Bi^{\bullet}_{Ge} + e' \tag{5.9}$$

Indeed one Ge_{Bi} produces one hole while one Bi_{Ge} creates one electron. In the presence of Ge vacancies, we can write

$$(Ge_{1-\delta})_2Bi_2Te_4 \rightleftharpoons \delta V''_{Ge} + 2\delta h^{\bullet} \tag{5.10}$$

Therefore, the hole carrier density can be estimated by calculating $2\delta/A$, where A represents the unit cell volume with cm^3 as the unit. The carrier densities calculated through this defect analysis are denoted as p_2 and are summarized in Table I. As observed, the correspondence between p_1 and p_2 is reasonably good, especially for the $x = 0$ and 0.33 samples.

We may tentatively estimate the saturation field of the $x = 0.47$ sample by assuming linear field dependence of M above 14 T. The interpolation is shown in Fig. 5.5 (a). When the magnetization at 2 K reaches 4.5 μ_B/Mn, the saturation field is estimated to be around 30 T. For a uniaxial antiferromagnet, long-range order requires either interlayer coupling, or uniaxial magnetic anisotropy. Due to the bilayer nature of 225, there exist two interlayer exchange couplings, as depicted in Fig. 5.5(b): one is J_{c1}, representing the interlayer AFM coupling within each NL per Mn, the other is J_{c2}, denoting the interlayer coupling between adjacent NL per Mn. We can write down the full Hamiltonian in the ordered state, per Mn, as [41]:

$$\begin{aligned} E = E_0 + \frac{1}{2}x^2 J_{c1}\mathbf{S}_i \cdot \mathbf{S}_{i+1} + \frac{1}{2}x^2 J_{c2}\mathbf{S}_i \cdot \mathbf{S}_{i-1} \\ - xKS_z^2 - xg\mu_B \mathbf{S}_i \cdot \mathbf{H}, \end{aligned} \tag{5.11}$$

where g is the Lande factor, $\mathbf{S}_i$ represents the Mn spin under investigation, $\mathbf{S}_{i+1}$ is the Mn in the same NL as $\mathbf{S}_i$ while $\mathbf{S}_{i-1}$ is the Mn in the adjacent NL, K is the magnetic anisotropy parameter per Mn and $S = 5/2$. Since $\mathbf{S}_{i+1}$ and $\mathbf{S}_{i-1}$ represent identical spin, we can combine two exchange coupling as $J_c = 1/2(J_{c1} + J_{c2})$. The relationship between J_c and K is then,

$$SK = (g\mu_B/2)(H_{sf}^2/H_s^{\|c}) \tag{5.12}$$

$$SJ_c = (g\mu_B/4x)\left(H_s^{\|c} + H_{sf}^2/\, H_s^{\|c}\right), \tag{5.13}$$

Where H_{sf} and H_s is the spin flop field and saturation field. Using critical fields obtained above, we can get $SK = 8.0$ μeV and $SJ_c = 1.8$ meV. Table IV summarizes SJ_c, K, Mn-Mn distances and bond angles in Mn-Bi-Te family for comparison. Since $J_{c1} \gg J_{c2}$ owing to the much shorter superexchange path of J_{c1} compared to J_{c2}, J_{c1} can be approximated as J_c. J_{c1} of $(Mn_{0.47}Ge_{0.41})_2Bi_2Te_5$ is much larger than that of the $MnBi_{2n}Te_{3n+1}$ series. This is reasonable, given the much shorter Mn-Mn nearest-neighbor interlayer distance of 4.39 $\mathring{A}$ in GeMn225 (L_2) compared to 13.86 $\mathring{A}$ in $MnBi_2Te_4$ (L_1) or other Mn-Bi-Te compounds. Meanwhile, owing to a similar exchange path, J_{c1} should be comparable to the coupling between the primary Mn site and the Mn_{Bi} antisite in $MnBi_2Te_4$. Indeed, the latter is responsible for the high full saturation field in $MnBi_2Te_4$ [62]. A much smaller magnetic anisotropy is obtained for $(Mn_{0.47}Ge_{0.41})_2Bi_2Te_5$, compared to $(Mn_{0.6}Pb_{0.4})Bi_2Te_4$, despite both have similar Mn occupancy and ordering temperature. This can be understood qualitatively by the bond angle analysis. As depicted in Table IV, both the Te-Mn-Te (α) and Te-Mn-z (β) angles exhibit a significant decrease in $(Mn_{0.47}Ge_{0.41})_2Bi_2Te_5$ compared to $MnBi_{2n}Te_{3n+1}$. When the bond angles decrease, the ligand-field splitting will also become smaller due to a less overlap of wavefunctions, leading to a reduced magnetic anisotropy [117, 118]. This also explains why SK remains similar across the $MnBi_{2n}Te_{3n+1}$ series (refer to Table IV), as the lattice environment of Mn remains consistent in these compounds.

When GeMn225 is exfoliated into even-NL or odd-NL thin flakes, both the inversion symmetry $\mathcal{P}$ and time reversal symmetry $\mathcal{T}$ are broken, while the combined $\mathcal{PT}$ symmetry is preserved. This symmetry condition is the same as the even-layer $MnBi_2Te_4$ device, where the Layer Hall effect [25] and quantum metric nonlinear Hall effect [26] are discovered. Therefore,

the bilayer A-type AFM and the non-trivial band topology nature of GeMn225 [110, 112] make it an excellent system for probing these emergent phenomena, eliminating the need to differentiate between even-NL or odd-NL devices.

5.5 Summary and Outlook

In summary, we have grown high-quality single crystals of $(Ge_{1-\delta-x}Mn_x)_2Bi_2Te_5$ with the doping level x up to 0.47. Elemental analysis and diffraction techniques not only suggest Ge/Bi mixing, but also reveal the presence of significant Ge vacancies of $0.11 \leq \delta \leq 0.20$, being responsible for the holes dominating the charge transport. As x increases, long-range AFM order with the easy axis along c emerges at 6.0 K for the $x = 0.33$ sample and at 10.8 K for the $x = 0.47$ sample. Spin-flop transitions observed at 0.7 T for $x = 0.33$ and 2.0 T for $x = 0.47$. Our refinement of the neutron diffraction data of the $x = 0.47$ sample suggests a bilayer A-type AFM structure with the ordered moment of 3.0(3) μ_B/Mn at 5 K. Our analysis of the magnetization data reveals a much stronger interlayer AFM exchange interaction and a much reduced uniaxial magnetic anisotropy when contrasted with $MnBi_2Te_4$. We argue the former arises from the shorter superexchange path and the latter to be linked to the smaller ligand-field splitting in $(Ge_{1-\delta-x}Mn_x)_2Bi_2Te_5$. Our study illustrates that this series of materials always exhibit broken $\mathcal{P}$ and broken $\mathcal{T}$ symmetries yet preserved $\mathcal{PT}$ symmetry upon exfoliation into thin flakes, providing a platform to explore the Layer Hall effect and quantum metric nonlinear Hall effect.

CHAPTER 6

Revealing the competition between charge-density wave and superconductivity in CsV_3Sb_5 through uniaxial strain

The majority of this chapter has been adapted from [119]. This work was done in collaboration with Turan Birol from University of Minnesota on DFT calculation, Rafael Fernandes from University of Minnesota and Brian from University of Copenhagen on phenomenological analysis.

6.1 Introduction

The interplay between superconductivity (SC) and charge-density waves (CDW) has a long history spanning several different classes of materials [120, 121]. In metals, while SC is a Fermi surface instability, CDW can arise due to nesting of the Fermi surface, lattice instabilities, or the electron-phonon interaction. As a result, the nature of the coupling between SC and CDW, from competing to cooperative, can be quite rich. For instance, in Cu_xTiSe_2 or pressurized $TiSe_2$, the superconducting transition temperature (T_c) reaches its maximum when the CDW state is suppressed completely [122, 123], suggesting a possible link between CDW fluctuations and the formation of Cooper pairs. In cuprates, CDW fluctuations are observed to be suppressed below the onset of SC, indicative of competition between the two phases [124, 125]. On the other hand, in materials such as pressurized 1T-TaS_2 and 2H-$NbSe_2$ [126, 127], SC seems to be little affected by the suppression of CDW.

Recently, a family of quasi-two-dimensional kagome materials, AV_3Sb_5 (A = K, Rb,

and Cs), has been discovered [128], sparking the interest of the community due to the presence of SC, CDW and non-trivial band structure [129, 130, 130–135]. As shown in the inset of Fig. 6.1(a), at room temperature, CsV_3Sb_5 crystallizes in the hexagonal space group $P6/mmm$ with alternating Cs layers and V_3Sb_5 layers made of face-sharing VSb_6 octahedra. Of particular importance, the V atoms form a kagome lattice, which has been proposed to be the major structural ingredient responsible for the emergent phenomena of CDW, with transition temperature $T_{CDW} \sim 94$ K, and of SC, with $T_c \sim 3$ K. The structure of the CDW phase remains widely debated, with studies reporting unidirectional CDW [132, 133, 136], a three-dimensional CDW with a 2×2×2 superstructure [137] or a 2×2×4 superstructure [133], a chiral CDW [138–140], and a CDW that breaks the sixfold rotational symmetry of the kagome lattice [136, 141].

A rich interplay between CDW and SC was observed in CsV_3Sb_5 under external hydrostatic pressure [142–147]. Upon increasing the pressure up to 10 GPa, T_c and T_{CDW} were found to compete with each other, leading to a SC dome in the temperature-pressure phase diagram, with the maximum $T_c \sim 8$ K occurring at a pressure of 2 GPa, where the CDW order is completely suppressed. Furthermore, a dip in the SC dome was observed at ~ 1 GPa, concurrent with a possible commensurate to nearly-commensurate CDW transition [144]. When the pressure was further increased, an additional SC dome with a maximum T_c of 5 K appears and persists up to 100 GPa, the maximum pressure measured. Despite the rapidly-evolving understanding of the CDW and the competition between CDW and SC, the nature of the SC state remains unsettled. While thermal conductivity measurements suggest nodal SC [142], penetration depth measurements indicate nodeless SC [148].

In this chapter I will introduce our investigation on Sc and CDW's responses to uniaxial strain applied along the a axis in CsV_3Sb_5. Comparing to hydrostatic pressure, which equally compresses the lattice along all directions, uniaxial strain not only explicitly breaks the sixfold rotational symmetry of the lattice, but it can both compress and stretch the lattice along a certain direction. It has been employed previously as a powerful tool to tune and detect exotic phases in both topological [149, 150] and strongly correlated systems [151–153].

The linear-dominated monotonic dependence of T_{CDW} with strain reveals that the symmetry-breaking effect on the CDW is negligible. Instead, the T_{CDW} and T_c data for tensile a-axis strain quantitatively agree with the hydrostatic pressure data when both are plotted as a function of the c-axis compression. This strongly suggests that the structural parameter to which CsV_3Sb_5 is most sensitive is the c-axis lattice parameter. Moreover, the ratio of change of T_c with respect to T_{CDW} is almost identical to that seen in the pressure experiments.

Combined with first-principles calculations and a phenomenological analysis, we conclude that the enhancement of T_c with the tensile a-axis strain is likely entirely due to the suppression of the competing CDW order, rather than an independent change in the bare superconducting parameters, like the density of states. Such a strong competition between CDW and SC is indicative of phases competing for similar electronic states. We further propose that the suppression of T_{CDW} with the tensile a-axis strain is associated with a c-axis induced change in the trilinear coupling between the CDW order parameters with wave-vectors at the M and L points of the Brillouin zone.

6.2 Methods

CsV_3Sb_5 was synthesized with the Cs-Sb flux method [128]. Cs, V, and Sb elements were loaded into an alumina crucible at the molar ratio of 20:16.7:63.3 and subsequently sealed in a quartz ampule under 1/3 atm of argon. The quartz was heated to 1000 °C in 10 hours, where it dwelled for 20 hours, and then cooled to 800 °C in 20 hours, followed by a further cooling to 600 °C in one week. Finally, the furnace was turned off at 600 °C and the tube was taken out at room temperature. Millimeter-sized plate-like crystals can be separated once the product is immersed in water for hours in the fume hood to remove the flux.

The phase and purity of the single crystals were confirmed by the X-ray diffractions via a PANalytical Empyrean diffractometer (Cu Kα). The electrical resistivity and magnetic properties were measured in a Quantum Design DynaCool Physical Properties Measurement System and Magnetic Properties Measurement System, respectively. Uniaxial strain was

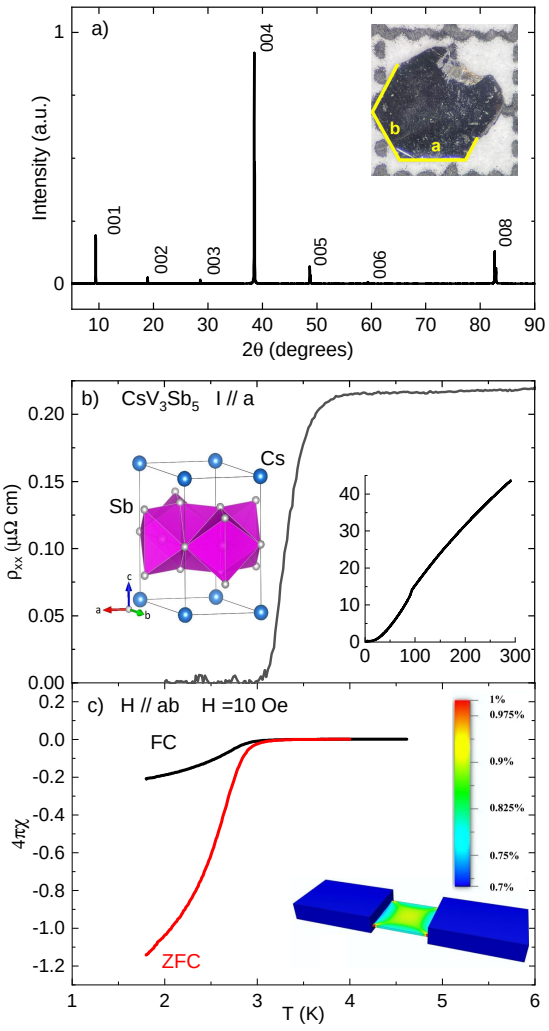

Figure 6.1: a) The $(00l)$ x-ray diffraction peaks of the cleaved ab plane for CsV_3Sb_5. Inset: a piece of single crystal against a 1-mm scale with the a and b axes labeled. b) The zoomed-in temperature-dependent electrical resistivity $\rho_{xx}(T)$ near the superconducting transition with the current along the a axis. Left inset: The crystal structure of CsV_3Sb_5. Right inset: $\rho_{xx}(T)$ from 2 K to 300 K. c) The ZFC and FC susceptibilities measured at 10 Oe with $H||ab$. To minimize the demagnetization factor, a thin plate with a thickness ~0.05mm was selected for the measurement and H was applied to be parallel to the sample plate. Inset: the mapping of the actual strain on the sample, see text for more details.

applied along the a-axis using a home-built three-piezostack strain apparatus [154]. A single crystal was carefully cut into a rectangular resistivity bar with the a-axis as the long side. This bar was then glued across the gap of the strain apparatus using Stycast. To minimize the strain gradients between the top and the bottom surfaces, extra care was made so that both ends of the bar were completely submerged in Stycast (Henkel Loctite STYCAST 2850FT with Catalyst 9). A foil strain gauge glued on one of the piezostacks was used to determine the value of strain, ε_{piezo}. Then the total strain induced by the apparatus was estimated as $\varepsilon_{total} = 2 \times \frac{L}{l} \times \varepsilon_{piezo}$, where L is the length of the piezo stack (9 mm) and l is the width of the apparatus gap (0.25 mm). Finally, ε, the actual average strain induced on the samples can be written as $A\varepsilon_{total}$ where A is a constant and determined via the Finite Element Analysis (FEA) using Autodesk Fusion 360. We modelled a 1 mm $\times$ 0.23 mm $\times$ 0.01 mm crystal glued by Stycast across our apparatus with a gap size of 0.25 mm. The Stycast glue is modeled as 0.02 mm between the sample and the strain apparatus and 0.05 mm above the sample. A was calculated to be 0.9 ± 0.01 on the portion of sample that is measured when 1% of expansion was applied to the gap, as shown in the inset of Fig. 1(c).

To calculate the density of states and phonon frequencies, first principles density functional theory calculations were performed using the Vienna Ab Initio Software Package (VASP) and the projector augmented waves formalism [155–157]. The exchange-correlation energy was approximated using the PBEsol functional and without a +U correction [158]. Reciprocal space k-grids with a density of a point per $\sim 0.012 \times 2\pi\text{Å}^{-1}$ were used in all calculations. The plane wave cutoff of 350 eV, and Cs and V potentials with s semi-core states treated as valence states were employed. Phonon calculations were performed using the frozen phonons technique. Since Fermi surface smearing is found to have an effect on the phonon frequencies, a Gaussian smearing with 1 meV width was used. The smearing does not make a qualitative difference in the densities of states, however, the phonon frequencies are dependent on the smearing as discussed in Ref. [159].

Uniaxial strain along the a-direction was simulated by fixing the magnitude of the lattice parameter a, and relaxing both the ionic positions and the other two lattice parameters. For

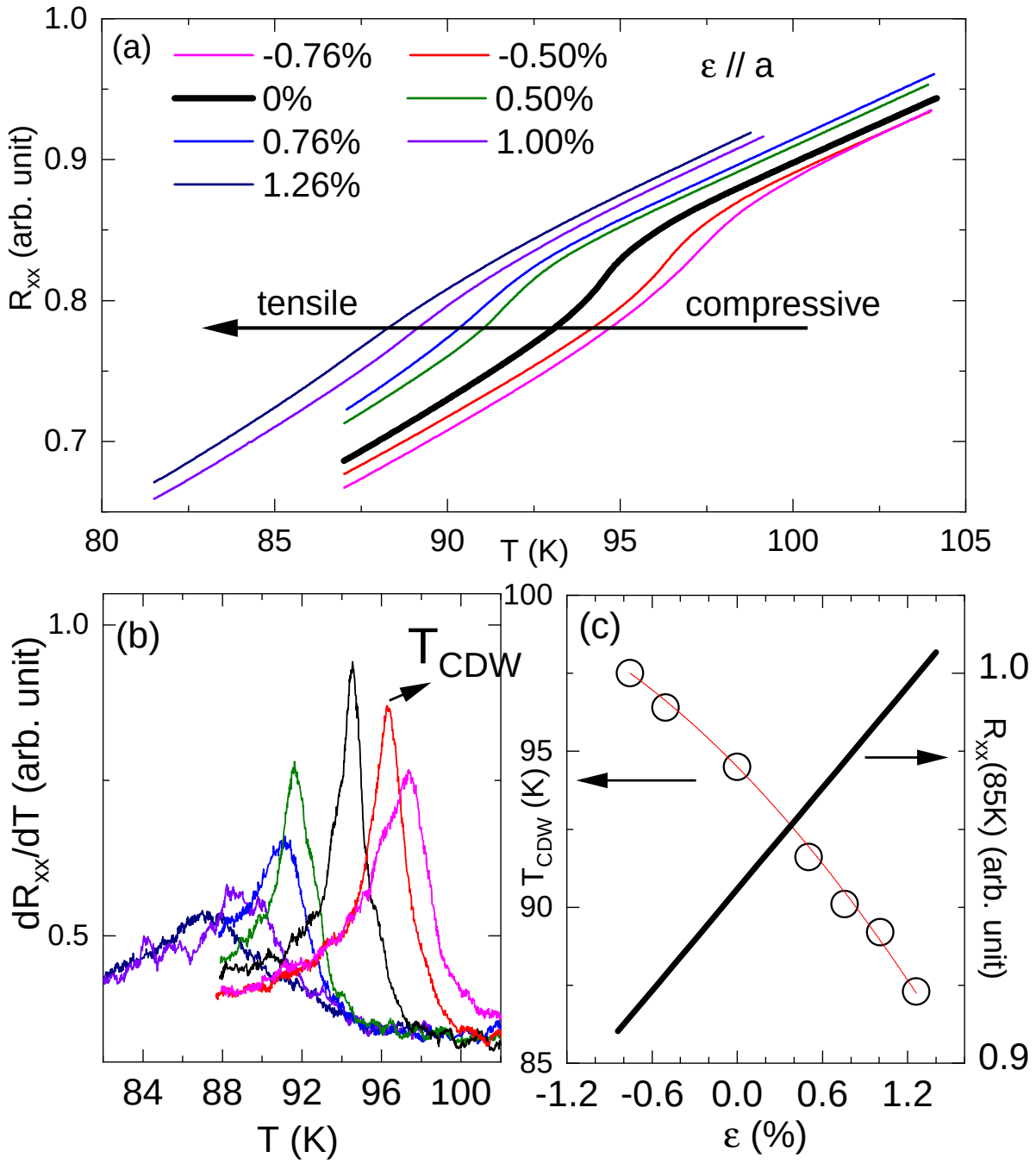

Figure 6.2: Strain dependence of T_{CDW} of a single crystal of CsV_3Sb_5. (a) Temperature dependence of the in-plane resistance of CsV_3Sb_5 near the CDW transition measured at different strain values. Negative values denote compressive strain, whereas positive values, tensile strain. (b) The temperature-derivative of the resistance, dR_{xx}/dT, whose peaks determine T_{CDW}. (c) T_{CDW} and resistance as a function of strain applied along the a-axis. Resistance is linearly proportional to the strain applied.

results presented in Fig. 6.5, which shows the trends of the phonons under decreasing c, only the internal coordinates of the atoms were relaxed.

6.3 Experimental results

Samples grew in hexagonal plates with clear as-grown edges, as shown in the inset of Fig. 1(a). The X-ray pattern taken on the surface of the plate can be indexed by the $(00l)$ reflections, shown in Fig. 1(a), indicating that the as-grown edges marked by the yellow lines are the crystalline a and b axes.

The temperature-dependent resistivity $\rho_{xx}(T)$ at ambient conditions is shown in the right inset of Fig. 1(b). Following a resistivity drop at 94.5 K, the sample enters the superconducting state below 3.4 K. These features are consistent with the values provided in the literature for the temperatures where the CDW and SC transitions are observed. The SC transition can be seen more clearly in the low-field susceptibility data presented in Fig. 1(c). The black curve is the field-cooled (FC) data while the red curve is the zero-field-cooled (ZFC) data. The large diamagnetic signal can be seen in both the ZFC and FC case, suggesting a large shielding fraction implying bulk superconductivity.

The right inset of Fig. 1(c) shows the map of the actual strain applied on the sample via FEA. Based on it, the average strain applied in the measured sample portion is $\varepsilon = 0.9\varepsilon_{total}$. In our experiment, before the resistivity bar cracked due to the applied strain, the setup successfully applied uniaxial strain from -0.90% (i.e. compressive strain) to 0.90% (i.e. tensile strain) around 2 K and from -0.76% to 1.26% around 85 K.

Figure 2(a) shows the resistance data $R_{xx}(T)$ around the CDW transition under various uniaxial strain values. As one can see, the resistance drop associated with the CDW transition moves to lower temperatures upon the application of tensile strain whereas it goes to higher temperatures when the sample is compressed. To determine T_{CDW} under strain, we use the peak position of the derivative dR_{xx}/dT, as shown in Fig. 2(b). Figure 2(c) shows the results for the strain-dependent $T_{CDW}(\varepsilon)$. It monotonically decreases when the sample

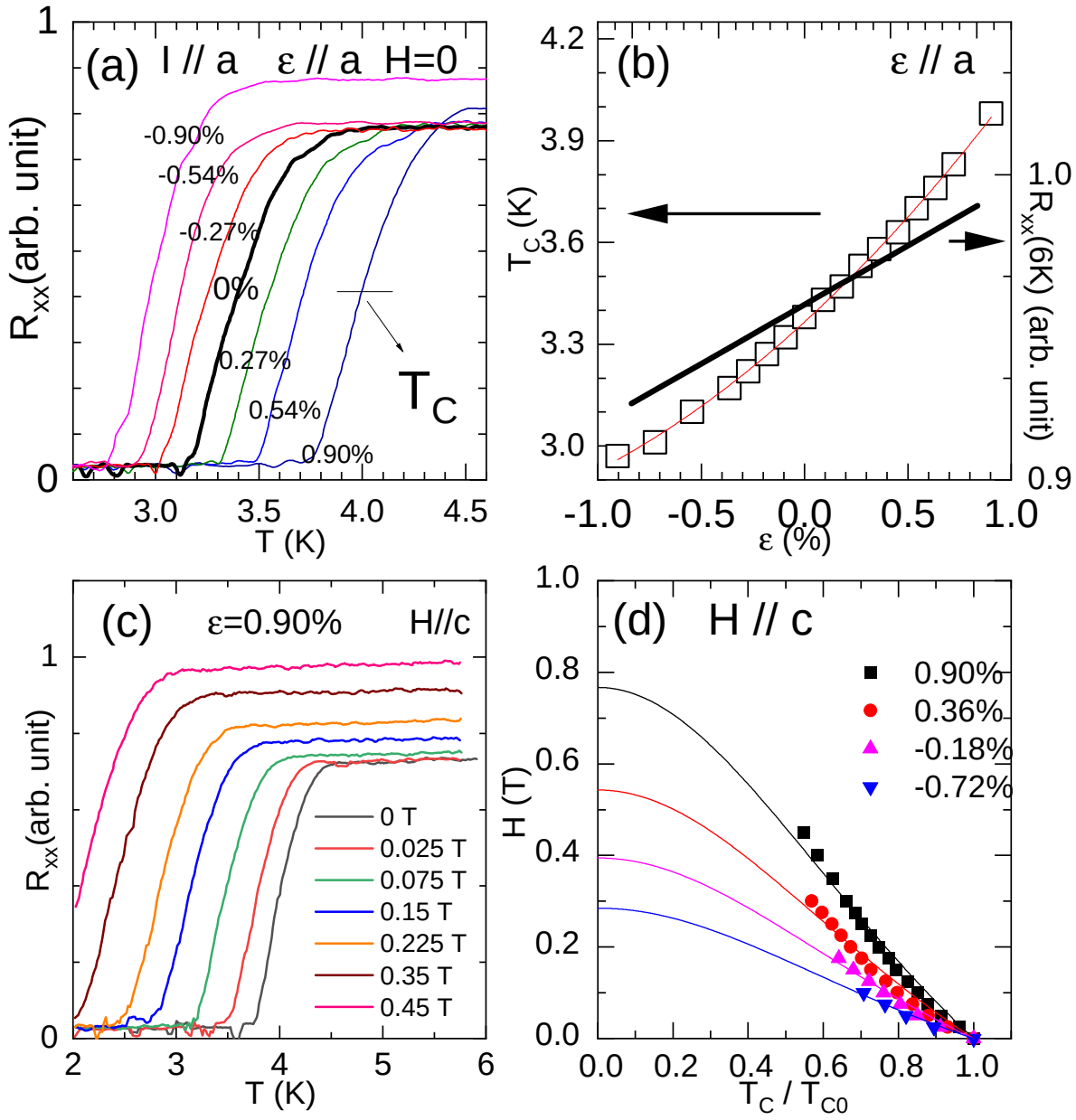

Figure 6.3: Strain dependence of T_c of CsV_3Sb_5. (a) Temperature dependence of the in-plane resistance R_{xx} of CsV_3Sb_5 near the superconducting transition. (b) Strain dependence of the resistance at 6 K and of T_c, which is determined by the 50%-resistance criterion. Resistance is linearly proportional to the strain applied. (c) Magnetic field dependence of the in-plane resistance in the presence of an applied 0.90% tensile strain. (d) H_{c2} diagram of CsV_3Sb_5 subjected to different strain values. Solid lines are fittings to the Ginzburg-Landau model.

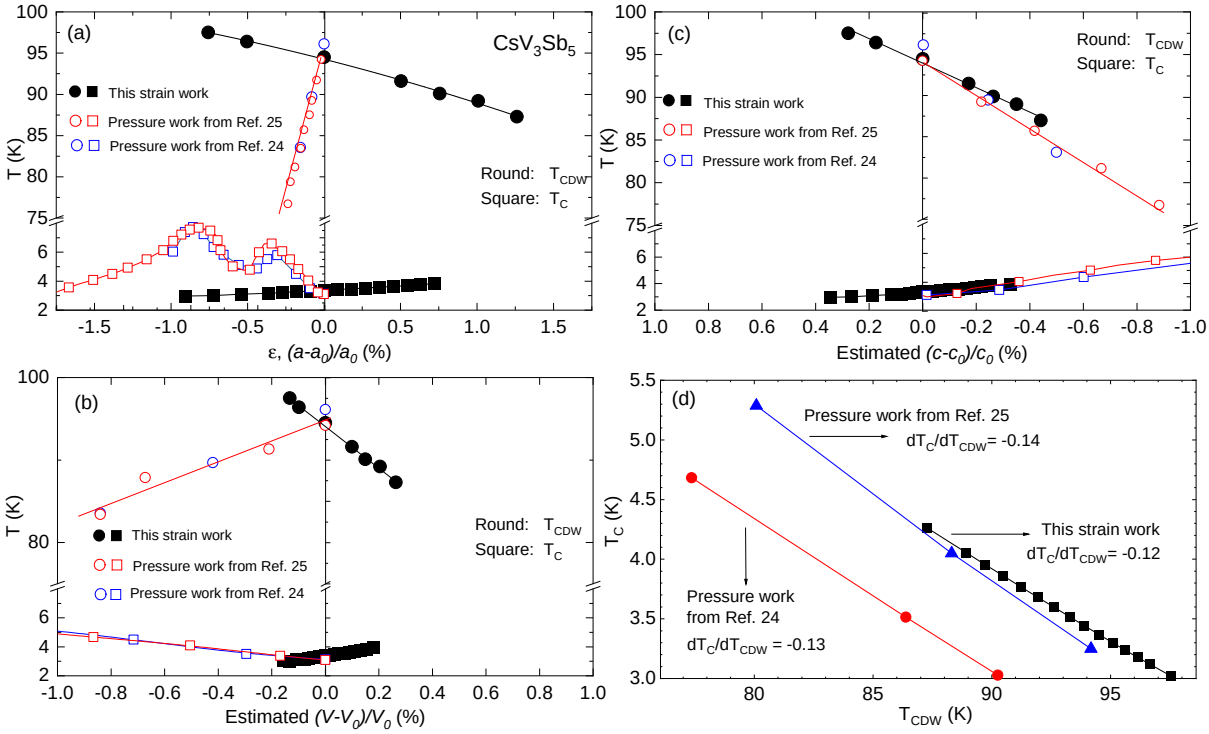

Figure 6.4: Comparison between the phase diagrams obtained from uniaxial strain measurements (this work) and previous hydrostatic pressure measurements [143, 144] (a) The effect of the change in lattice parameter a on T_{CDW} and T_c. The relationship between the lattice parameters and pressure was obtained from Ref. [145]. (b) The effect of the change in volume V on T_{CDW} and T_c. The response of the lattice parameter c with respect to the strain was extracted from DFT calculations. (c) The effect of the change in c on T_{CDW} and T_c. (d) T_c plotted as a function T_{CDW} for both pressure and uniaxial strain experiments.

expands along the a axis, being 97.5 K when the a-axis is strained by -0.76%, 94.5 K for no applied strain, and 87.3 K when the a-axis expands by 1.26%. A polynomial fitting to $T_{CDW}(\varepsilon)$ gives $T_{CDW}(\varepsilon) = 94.5 - 4.72\varepsilon - 0.60\varepsilon^2$, revealing a dominant linear term.

Figure 3(a) shows the $R_{xx}(T)$ data around the superconducting transition under applied strain. T_c increases with compressive strain and decreases for tensile strain. T_c is determined using the 50%-resistance criterion, as shown in Fig. 3(a). Figure 3(b) summarizes the strain-dependent $T_c(\varepsilon)$. It is 3.0 K at -0.90% strain, 3.4 K for no applied strain, and 4.0 K at 0.90% strain. A polynomial fitting to $T_c(\varepsilon)$ gives $T_c(\varepsilon) = 3.4 + 0.56\varepsilon + 0.12\varepsilon^2$.

Figure 3(c) shows a representative example of the behavior of $R_{xx}(T)$ in a strained sample ($\varepsilon = 0.90\%$ in this case) under different magnetic fields applied along the c-axis, $H \parallel c$. As expected, the SC transition is suppressed with increasing fields. The field dependence of T_c under different strains is summarized in Fig. 3(d). The zero-temperature upper critical field $H_{c2}^{\parallel c}(0)$ can then be estimated by fitting the $H_{c2}(T)$ data with the empirical Ginzburg-Landau equation, $H_{c2}(T) = H_{c2}(0)(1-t^2)/(1+t^2)$, where $H_{c2}(0)$ is the zero-temperature upper critical field and $t = T/T_c$ is the reduced temperature. The fitting curves are shown in Fig. 3(d) as solid lines. We see that $H_{c2}^{\parallel c}(0)$ has a strong strain dependence, increasing to 0.77 T when 0.90% strain is applied and decreasing to 0.29 T when -0.72% strain is applied.

Although strain was applied along the a-axis, the sample will deform (unequally) in all three directions according to the Poisson ratios. To obtain a better understanding of which of the lattice parameters controls T_{CDW} and T_c in our experiments, DFT calculations were performed to calculate the changes in the lattice parameter c and in the volume V under our experimental conditions. The data were then compared to previous hydrostatic pressure measurements, in which case all three directions are compressed equally. Using the lattice parameter changes with respect to pressure reported in Ref. zhang2021pressure, the relationship between the CDW/SC transition temperatures and the changes in different lattice parameters can be compared for our uniaxial strain experiment and the hydrostatic pressure experiments of Refs. chen2021double,yu2021unusual.

In Figs. 4(a), (b) and (c), we plot the transition temperatures T_{CDW} and T_c as a function

of the change in the lattice parameter a, volume V and lattice parameter c, respectively, for our work and for the pressure data of Refs. chen2021double,yu2021unusual. Figure 4(a) shows that, in the case of hydrostatic pressure, a decreasing a leads to a decrease in T_{CDW} and an initial increase in T_C. Meanwhile, in the case of uniaxial strain, upon decreasing a, T_{CDW} increases and T_C decreases. The opposite response of T_{CDW} and T_c with respect to changes in a via two different experimental techniques suggests that a is not the primary lattice parameter tuning the CDW and SC. A similar conclusion can be drawn from Fig. 4(b), indicating that the volume V is not the main tuning parameter either. On the other hand, as shown in Fig. 4(c), for both the pressure and the uniaxial strain data, T_{CDW} decreases and T_c increases with decreasing c. Clearly, the agreement is not only qualitative, but also quantitative: the ratio of change of T_{CDW} (T_c) with respect to the c-axis compression is nearly the same for both uniaxial strain and pressure data. These observations provide strong evidence that c is the primary lattice parameter responsible for tuning the CDW and SC transitions.

In both pressure and strain measurements, in the region of c-axis compression, T_{CDW} is suppressed while T_c is enhanced. In the strain measurements, which can also assess the region of c-axis expansion, we further notice that when T_{CDW} is enhanced, T_c is suppressed. This competing relationship between CDW and SC indicates that both phenomena are affected by similar electronic states. Figure 4(d) presents a plot of T_c as a function of T_{CDW} for both pressure and strain experiments. In all cases, T_C depends linearly on T_{CDW} with a negative slope that varies weakly from -0.12 to -0.14, within the experimental error. Combined with Fig. 4(c), this result suggests the reason why T_c increases upon the application of pressure or tensile a-axis strain is because the competing CDW order is suppressed due to the change in the c-axis lattice parameter.

Last but not least, one important difference between uniaxial strain and hydrostatic pressure is that the former breaks the (sixfold) rotational symmetry of the lattice, but the latter does not. The fact that T_c and T_{CDW} change in the same way regardless of whether pressure or uniaxial strain is applied, as long as the c-axis compression is the same in both

cases, indicates that the impact of the explicit breaking of the lattice symmetry is negligible compared to the effect arising from the change in the c-axis lattice parameter.

6.4 Discussion

We have shown that the c-axis lattice parameter is the dominant structural parameter that controls the changes of T_{CDW} and T_c upon the application of uniaxial strain or pressure. To shed light on the microscopic mechanism of this effect, we calculate the strain-dependent phonon frequencies and density of states (DOS) using DFT in the non-CDW phase. Similar to Ref. ratcliff2021coherent, our DFT results reveal CsV_3Sb_5 to have at least two unstable phonon modes at the M and L points of the Brillouin zone, which are associated with the CDW transition (see also Ref. christensen2021theory). These phonon modes transform as the M_1^+ and L_2^- irreducible representations of the space group, as shown in Fig. 6.5(a).

In Fig. 6.5(b), we display the behavior of these unstable phonon frequencies as a function of changes in the lattice parameter c. We find that the frequencies associated with the two modes show opposite and non-monotonic trends as a function of c in the region $-1\% \leq (c - c_0)/c_0 \leq 1\%$ (see Fig. 4(c)). Similar calculations repeated with different electronic smearing parameters indicate that Fig. 6.5 sensitively depends on how the electronic structure is treated. Such an observed sensitivity supports the view that the electronic degrees of freedom are responsible for the unstable phonons observed in DFT [159]. While a precise quantitative prediction is obscured due to the dependence on the electronic smearing, the non-monotonic features and the opposite trends of the two modes remain robust. So qualitatively, if we associate the unstable phonon frequencies to the energy scale of the CDW transition, the opposite trends in the L and M modes, which will both condense in the $2 \times 2 \times 2$ CDW state, seems difficult to reconcile with the monotonic, nearly linear suppression of T_{CDW} with $(c - c_0)/c_0$ seen experimentally.

To further elucidate this issue, we employ the Landau free-energy expansion for the CDW transition in AV_3Sb_5 [159]. The two unstable phonon modes are three-fold degenerate

because the hexagonal symmetry of the lattice gives rise to three distinct M and L wave-vectors at different faces of the Brillouin zone. We denote the CDW order parameters associated with different M wave-vectors as M_1, M_2, and M_3, and similarly, we use L_1, L_2, and L_3 to denote the order parameters with L wave-vectors. An illustration of these different order parameters can be found in Fig. 6.5(a) in terms of distortions of the bonds connecting the V atoms. Since the out-of-plane component of the M wave-vector is zero, the displacement of atoms on two consecutive layers are in phase. On the other hand, because of the out-of-plane component of the wave-vector L, the displacement of atoms on two consecutive layers are out of phase. To quadratic order, the free energies of these two order parameters are decoupled and given simply by:

$$\mathcal{F}^{(2)} = \alpha_M \left(M_1^2 + M_2^2 + M_3^2\right) + \alpha_L \left(L_1^2 + L_2^2 + L_3^2\right) \tag{6.1}$$

The leading coupling between the two order parameters appears in cubic order as the trilinear coupling [159]:

$$\mathcal{F}^{(3)} = \gamma_{ML} \left(M_1 L_2 L_3 + M_2 L_3 L_1 + M_3 L_1 L_2\right) \tag{6.2}$$

This term is allowed since adding up one of the three M wave-vectors with the two "opposite" L wave-vectors gives zero [159].

The Landau coefficients α_M, α_L, and γ_{ML} are material-specific and, quite generically, expected to depend on the lattice parameter c. While they can in principle be calculated by DFT, this is an involved calculation that is beyond the scope of this work. Notwithstanding the aforementioned issues with the calculated DFT phonon frequencies, we can still gain some insight from the trends shown in Fig. 6.5(b). Generally, the quadratic coefficient of a Landau free-energy expansion is positive in the disordered state and negative in the ordered state. Thus, in our case, we expect the quadratic coefficients α_M and α_L to be negative in the $2 \times 2 \times 2$ CDW state. Because the squared frequencies of the M_1^+ and L_2^- phonon modes are positive in the non-CDW state and negative in the CDW state, it is reasonable to assume that α_M, α_L are proportional to the squared frequencies of the unstable phonon modes. We emphasize that, in Fig. 6.5(b), we are showing the square root of the absolute value of the negative squared frequency. Therefore, in the experimentally relevant range

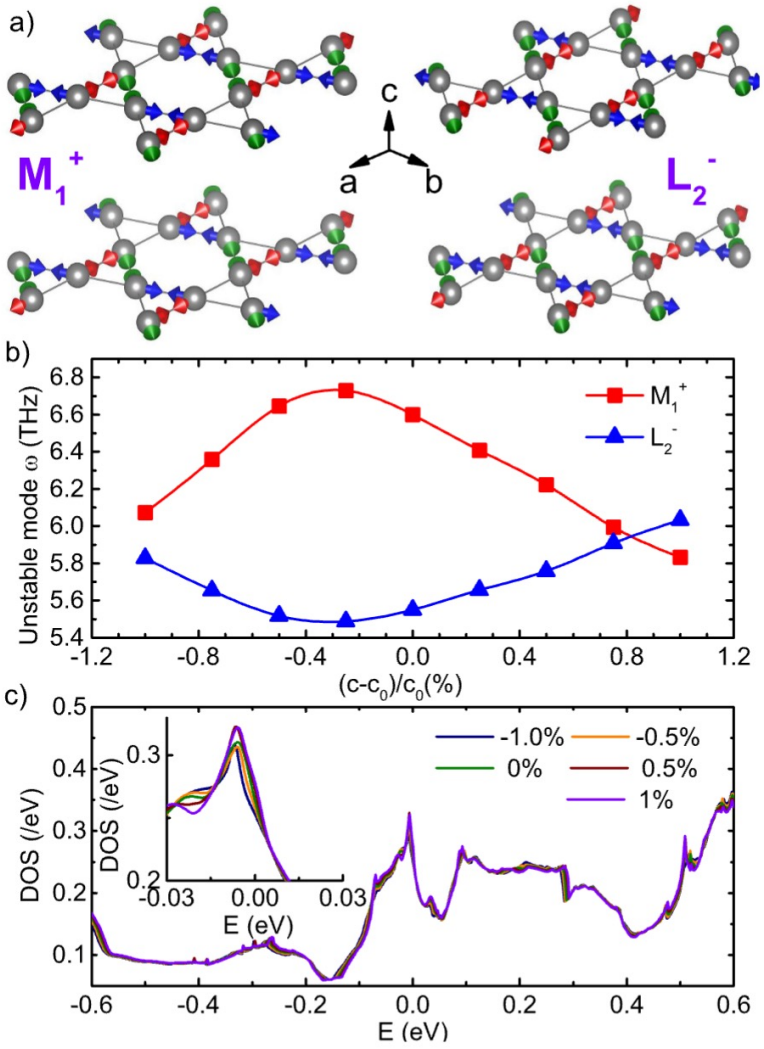

Figure 6.5: (a) Left: the displacement pattern of the M_1^+ phonon mode. For clarity, only the vanadium ions and two consecutive kagome layers are shown. Red, blue, and green arrows correspond to displacements according to the M_1, M_2 and M_3 components. Right: Same as the left panel, but for the L_2^- mode. (b) Unstable phonon frequencies as a function of the c lattice parameter from first principles calculations. Because the squared phonon frequencies are negative for unstable modes, we plot the square root of the absolute value of the squared frequencies. (c) Electronic density of states (DOS) of CsV_3Sb_5, calculated from DFT, in the high temperature, high symmetry phase, as a function of the lattice parameter c. The inset is a zoom of the low-energy part of the spectrum. The van Hove singularity peak below the Fermi level is suppressed under compression of the c-axis.

$-0.4\% \leq (c - c_0)/c_0 \leq 0.4\%$, we conclude that $|\alpha_M|$ and $|\alpha_L|$ have an almost monotonic dependence on $(c-c_0)/c_0$. In particular, $|\alpha_M|$ decreases with increasing $(c-c_0)/c_0$, suggesting that the tensile c-axis strain brings the M mode closer to the disordered phase. On the other hand, $|\alpha_L|$ increases with increasing $(c-c_0)/c_0$, indicating that the tensile c-axis strain moves the L mode deeper into the ordered phase. Now, experimentally, from Fig. 4(c), we see that T_{CDW} is enhanced by an expanding c-axis. One possibility, therefore, is that it is the L mode that is becoming soft at the CDW transition, with the M mode being triggered only due to the trilinear coupling in Eq. (6.2). The caveat with this scenario is that the M mode seems to generally have a larger (absolute) frequency than the L mode.

Another possibility is that the main effect of the c-axis change is not on the phonon frequencies, but on the trilinear coupling γ_{ML} of Eq. (6.2). This scenario seems more likely for several reasons. First, as discussed in Ref. [159], a relatively large trilinear coupling is needed to obtain a single transition to a $2 \times 2 \times 2$ CDW state that breaks sixfold rotational symmetry, as observed experimentally [136, 141]. Second, in this scenario T_{CDW} is rather sensitive to γ_{ML}. Third, because γ_{ML} couples order parameters with the same in-plane wave-vector components but different out-of-plane wave-vector components, it seems reasonable to expect that γ_{ML} has a pronounced dependence on c. As a result, c will be the primary parameter in controlling T_{CDW}, as revealed in Fig. 4. Of course, additional DFT calculations are needed to conclusively decide if changes in the parameters $\alpha_{L,M}$ or γ_{ML} are responsible for the experimentally observed change in the CDW transition temperature upon uniaxial strain.

The DFT results also provide insight into the mechanism by which T_c increases when the c axis is compressed. The DOS of the high symmetry (i.e. non-CDW) phase of CsV_3Sb_5 is displayed in Fig. 6.5(c). By not taking into account the structural symmetry lowering induced by the CDW, we focus only on the direct effect of strain on the DOS. We observe the van Hove singularity (VHS) right below the Fermi level [160–162], which is believed to be important in determining the superconducting instability [163–166]. Since in our calculations no CDW order is considered, if the change in the DOS under strain can account

for the change in T_c observed experimentally, this would suggest that the strain-induced enhancement of T_c would happen even in the absence of CDW order, suggesting a weak effect of the CDW phase on the SC properties. However, this does not seem to be the case here. Although a quantitative estimate of T_c is challenging, we see that decreasing the c-axis lattice parameter partially suppresses the DOS peak corresponding to the VHS. This is expected to cause a decrease in T_c, as opposed to the experimental observation. This analysis corroborates the conclusion drawn from Fig. 4(d) that the changes in T_c under uniaxial strain are dominated by the competition with the CDW state, such that a strain-driven enhancement (suppression) of T_{CDW} results in a suppression (enhancement) of T_c. This result, in turn, could be a consequence of the CDW and SC states competing for the same electronic states.

6.5 Summary and Outlook

In summary, we investigated the interplay between CDW and SC in CsV_3Sb_5 under uniaxial strain applied along the a-axis. Comparing our results with recent pressure measurements [143–145], we conclude that both T_c and T_{CDW} are dominated by changes in the c-axis lattice parameter, regardless of whether they are promoted by hydrostatic pressure or uniaxial strain. Therefore, this comparison further suggests that the effect of the broken rotational-symmetry induced by the uniaxial strain on the CDW and SC states is weak [143, 144]. Moreover, combined with a theoretical analysis, our results not only highlight the importance of the coupling between the two unstable phonon modes on the formation of the CDW, but also indicate that the enhancement of T_c with decreasing c is due to the suppression of the competing CDW instability.

CHAPTER 7

Conclusion

In this dissertation, I present our studies on tuning the magnetism and superconductivity in magnetic and superconducting topological materials through chemical doping, external pressure and uniaxial strain.

First, we have used high-quality $(Mn_{1-x}Pb_x)Bi_2Te_4$ to investigate the doping effect in $MnBi_2Te_4$. We find that unlike Sb-doped $MnBi_2Te_4$ where Sb doping introduces more Mn_{Bi} antisites and leads to complicated magnetic competitions, upon Pb doping, the amount of the Mn_{Bi} antisites remains minimal, making this doping series a great system to investigate the dilution effect on both magnetism and band topology. Indeed, the Nel temperature and saturation field decreases linearly with doping. Furthermore, our DFT calculations reveal two gapless points within the doping series. Along with the sign change of the anomalous Hall resistivity, this could suggest possible topological phase transitions.

In the second project, we use hydrostatic pressure to tune magnetic interactions in $Mn(Bi_{1-x}Sb_x)_4Te_7$. We find that the pressure effect on the transition temperature from the paramagnetic state to the ordered state is weak, which we demonstrate is due to its logarithmically weak dependence on the ratio of intralayer coupling to magnetic anisotropy. We also discover unconventional pressure-activated metamagnetic transitions with respect to pressure and temperature. We conclude that the pressure and temperature dependence of the two competing interlayer exchange interactions lead to these unconventional behaviors. Therefore, our study independently probes the interlayer coupling, intralayer coupling, and magnetic anisotropy, elucidating their roles in van der Waals magnetism.

In the third study, we have grown high-quality single crystals of $(Ge_{1-\delta-x}Mn_x)_2Bi_2Te_5$

with the doping level x up to 0.47. Site mixing between Ge and Bi together with significant Ge vacancies are revealed by elemental analysis and diffraction techniques. When Mn is doped into the system, long-range AFM order with a bilayer A-type AFM structure and easy c axis appears. From magnetization data we obtain a much larger interlayer AFM exchange interaction and much smaller uniaxial magnetic anisotropy with respect to $MnBi_2Te_4$. The former can be explained by a much shorter interlayer superexchange path and the latter can be qualitatively explained by a smaller ligand-field splitting. Overall, we have demonstrated $(Ge_{1-\delta-x}Mn_x)_2Bi_2Te_5$ as a good AFM topological insulator candidate that holds promise for the investigation of the Layer Hall effect and quantum metric nonlinear Hall effect.

Lastly, we have investigated the interplay between charge-density-wave (CDW) and superconductivity (SC) in the kagome topological superconductor candidate CsV_3Sb_5 with the uniaxial strain applied along the in-plane a-axis. Our experiment reveals the competition between CDW and SC. Comparing our results with pressure measurements, we conclude that both transitions are dominated by changes in the c-axis lattice parameter. This comparison further indicates that the effect of the broken rotational-symmetry induced by the uniaxial strain on the CDW and SC states is insignificant. Moreover, our theoretical analysis has pointed to the importance of the trilinear coupling of the unstable phonon modes in the formation of CDW.

In summary, our research enhances the understanding of the interplay between magnetism, band topology, and superconductivity in magnetic and superconducting topological material systems and the insights gained from our work pave the way for future experimental and theoretical investigations into novel topological materials.

Appendix A

Additional Structural Refinement of $(\mathbf{Ge}_{1-\delta-x}\mathbf{Mn}_x)_2\mathbf{Bi}_2\mathbf{Te}_5$ $(x \leq 0.47, 0.11 \leq \delta \leq 0.20)$

A.1 Neutron diffraction to determine stacking

Neutron diffraction is used to determine if Mn is doped into site 1 or site 2. The refinement was made using P-3'm'1 magnetic space group. For simplicity, we mainly care about Mn distributions, and assume Ge and Bi each occupy one site only. We examined three possible scenarios, stacking A with Mn in the inner sites, stacking B with Mn on the outer sites, and a mixed stacking where Mn can go into either. The results of three stacking scenarios are shown in Table S1 - 3.

Table A.1: Refined structural parameters for the x =0.53 sample based on the single crystal neutron diffraction data for stacking A, where Mn is located on site 2d, or inner layers. (for magnetic refinement, number of reflections: 38; $R_F = 9.83\%$; $\chi^2 = 5.56$)

Atom	site	x	y	z	occ	Moment at 5 K
Ge1	2d	1/3	2/3	0.105(5)	0.57(2)	
Mn1	2d	1/3	2/3	0.105(5)	0.43(2)	2.8(7) μ_B/Mn
Bi2	2c	0	0	0.212(2)	1	
Te1	1a	0	0	0	1	
Te2	2d	1/3	2/3	0.800(2)	1	
Te3	2d	1/3	2/3	0.420(2)	1	

A.2 Powder X-ray Refinement

A.2.1 Determine vacancy amount

For powder X-ray, the total scattering strength of each site should be the same. Two special refinements were done, each of them only contain one type of element in both site 1 and site 2. One is with Ge and one is with Bi, as shown in Table S4 and S5. The ratio between the amount of Ge and Bi in each individual site can help derive the ratio of scattering strength between each element. Here $B_{Bi}^2/B_{Ge}^2 = 2.7$ can be obtained.

Table A.2: Refined structural parameters for the x =0.53 sample based on the single crystal neutron diffraction data for stacking B, where Mn is located on site 2c, or outer layers. (for magnetic refinement, number of reflections: 38; $R_F = 16.5\%$; $\chi^2 = 9.04$)

Atom	site	x	y	z	occ	Moment at 5 K
Bi1	2d	1/3	2/3	0.123(3)	1	
Ge2	2c	0	0	0.374(6)	0.55(2)	
Mn2	2c	0	0	0.374(6)	0.45(2)	2.4(9) μ_B/Mn
Te1	1a	0	0	0	1	
Te2	2d	1/3	2/3	0.769(3)	1	
Te3	2d	1/3	2/3	0.441(3)	1	

A.2.2 Determine vacancy position

PXRD can be used to show how Bi, Ge and vacancy distributed on each sites. We have refined three different situations, when the distribution of vacancy on site 2d and 3c is at the ratio of 0.2 : 0, 0.1 : 0.1 and 0 : 0.2. The first two refinements are shown in Table S6 and S7, while the last refinement is presented in the main text.

Table A.3: Refined structural parameters for the x =0.53 sample based on the single crystal neutron diffraction data for mixed stacking. (for magnetic refinement, number of reflections: 38; $R_F = 11.7\%$; $\chi^2 = 6.38$)

Atom	site	x	y	z	occ	Moment at 5 K
Ge1	2d	1/3	2/3	0.105(5)	0.50(2)	
Mn1	2d	1/3	2/3	0.105(5)	0.50(2)	2(1) μ_B/Mn
Bi2	2c	0	0	0.212(2)	0.95(2)	
Mn2	2c	0	0	0.212(2)	0.05(2)	-2(1) μ_B/Mn
Te1	1a	0	0	0	1	
Te2	2d	1/3	2/3	0.769(3)	1	
Te3	2d	1/3	2/3	0.441(3)	1	

Table A.4: Refined structural parameters for the $Ge_2Bi_2Te_5$ sample based on the powder X-ray sample with only Ge on both site 1 and site 2. ((Number of reflections: 6474; $R_F = 8.56\%$; $\chi^2 = 46.1$)

Atom	site	x	y	z	occ.
Ge1	2d	1/3	2/3	0.1041(3)	1.59(1)
Ge2	2c	0	0	0.3256(2)	1.79(1)
Te1	2a	0	0	0	1
Te2	2d	1/3	2/3	0.2044(3)	1
Te3	2d	1/3	2/3	0.4243(2)	1

Table A.5: Refined structural parameters for the $Ge_2Bi_2Te_5$ sample based on the powder X-ray sample with only Bi on both site 1 and site 2. ((Number of reflections: 6474; $R_F = 8.64\%$; $\chi^2 = 45.8$)

Atom	site	x	y	z	occ.
Bi1	2d	1/3	2/3	0.1041(3)	0.58(1)
Bi2	2c	0	0	0.3258(2)	0.66(1)
Te1	2a	0	0	0	1
Te2	2d	1/3	2/3	0.2045(2)	1
Te3	2d	1/3	2/3	0.4237(2)	1

Table A.6: Refined structural parameters for $Ge_2Bi_2Te_5$ sample based on the powder X-ray sample with WDS result been forced. The vacancy is all in site $2d$ ((Number of reflections: 6474; $R_F = 8.64\%$; $\chi^2 = 45.8$)

Atom	site	x	y	z	occ.
Ge1	$2d$	1/3	2/3	0.1041(3)	0.32(1)
Bi1	$2d$	1/3	2/3	0.1041(3)	0.48(1)
Ge2	$2c$	0	0	0.3258(2)	0.48(1)
Bi2	$2c$	0	0	0.3258(2)	0.52(1)
Te1	$2a$	0	0	0	1
Te2	$2d$	1/3	2/3	0.2045(2)	1
Te3	$2d$	1/3	2/3	0.4239(2)	1

Table A.7: Refined structural parameters for $Ge_2Bi_2Te_5$ sample based on the powder X-ray sample with WDS result been forced. The vacancy is evenly distributed on site $2d$ and $2c$ ((Number of reflections: 6474; $R_F = 8.64\%$; $\chi^2 = 45.8$)

Atom	site	x	y	z	occ.
Ge1	$2d$	1/3	2/3	0.1041(3)	0.48(1)
Bi1	$2d$	1/3	2/3	0.1041(3)	0.42(1)
Ge2	$2c$	0	0	0.3258(2)	0.32(1)
Bi2	$2c$	0	0	0.3258(2)	0.58(1)
Te1	$2a$	0	0	0	1
Te2	$2d$	1/3	2/3	0.2045(2)	1
Te3	$2d$	1/3	2/3	0.4239(2)	1

Bibliography

[1] M. E. Cage, K. Klitzing, A. Chang, F. Duncan, M. Haldane, R. B. Laughlin, A. Pruisken, and D. Thouless, *The quantum Hall effect*. Springer Science & Business Media, 2012.

[2] Y. Chen, J. G. Analytis, J.-H. Chu, Z. Liu, S.-K. Mo, X.-L. Qi, H. Zhang, D. Lu, X. Dai, Z. Fang, *et al.*, "Experimental realization of a three-dimensional topological insulator, bi2te3," *science*, vol. 325, no. 5937, pp. 178–181, 2009.

[3] Y. Tokura, K. Yasuda, and A. Tsukazaki, "Magnetic topological insulators," *Nature Reviews Physics*, vol. 1, no. 2, pp. 126–143, 2019.

[4] P. Zhang, K. Yaji, T. Hashimoto, Y. Ota, T. Kondo, K. Okazaki, Z. Wang, J. Wen, G. D. Gu, H. Ding, *et al.*, "Observation of topological superconductivity on the surface of an iron-based superconductor," *Science*, vol. 360, no. 6385, pp. 182–186, 2018.

[5] B. A. Bernevig and S.-C. Zhang, "Quantum spin hall effect," *Physical review letters*, vol. 96, no. 10, p. 106802, 2006.

[6] C.-Z. Chang, J. Zhang, X. Feng, J. Shen, Z. Zhang, M. Guo, K. Li, Y. Ou, P. Wei, L.-L. Wang, *et al.*, "Experimental observation of the quantum anomalous hall effect in a magnetic topological insulator," *Science*, vol. 340, no. 6129, pp. 167–170, 2013.

[7] S.-Y. Xu, C. Liu, S. K. Kushwaha, R. Sankar, J. W. Krizan, I. Belopolski, M. Neupane, G. Bian, N. Alidoust, T.-R. Chang, *et al.*, "Observation of fermi arc surface states in a topological metal," *Science*, vol. 347, no. 6219, pp. 294–298, 2015.

[8] C.-Z. Chang and M. Li, "Quantum anomalous hall effect in time-reversal-symmetry breaking topological insulators," *Journal of Physics: Condensed Matter*, vol. 28, no. 12, p. 123002, 2016.

[9] N. Nagaosa, J. Sinova, S. Onoda, A. H. MacDonald, and N. P. Ong, "Anomalous hall effect," *Reviews of modern physics*, vol. 82, no. 2, p. 1539, 2010.

[10] M. I. Dyakonov, "Possibility of orienting electron spins with current," *JETP Lett. USSR*, vol. 13, p. 467, 1971.

[11] Y. K. Kato, R. C. Myers, A. C. Gossard, and D. D. Awschalom, "Observation of the spin hall effect in semiconductors," *science*, vol. 306, no. 5703, pp. 1910–1913, 2004.

[12] L. Liu, C.-T. Chen, and J. Z. Sun, "Spin hall effect tunnelling spectroscopy," *Nature Physics*, vol. 10, no. 8, pp. 561–566, 2014.

[13] J. Sinova, S. O. Valenzuela, J. Wunderlich, C. Back, and T. Jungwirth, "Spin hall effects," *Reviews of modern physics*, vol. 87, no. 4, p. 1213, 2015.

[14] Wikipedia, "Quantum hall effect — Wikipedia, the free encyclopedia," 2024. [Online; accessed 16-April-2024].

[15] K. v. Klitzing, G. Dorda, and M. Pepper, "New method for high-accuracy determination of the fine-structure constant based on quantized hall resistance," *Physical review letters*, vol. 45, no. 6, p. 494, 1980.

[16] C. Day, "Quantum spin hall effect shows up in a quantum well insulator, just as predicted," *Physics Today*, vol. 61, no. 1, pp. 19–23, 2008.

[17] F. D. M. Haldane, "Model for a quantum hall effect without landau levels: Condensed-matter realization of the" parity anomaly"," *Physical review letters*, vol. 61, no. 18, p. 2015, 1988.

[18] C. L. Kane and E. J. Mele, "Z 2 topological order and the quantum spin hall effect," *Physical review letters*, vol. 95, no. 14, p. 146802, 2005.

[19] L. Fu and C. L. Kane, "Topological insulators with inversion symmetry," *Physical Review B*, vol. 76, no. 4, p. 045302, 2007.

[20] E. C. Stoner and E. Wohlfarth, "A mechanism of magnetic hysteresis in heterogeneous alloys," *Philosophical Transactions of the Royal Society of London. Series A, Mathematical and Physical Sciences*, vol. 240, no. 826, pp. 599–642, 1948.

[21] C. WAYMAN and H. BHADESHIA, "Chapter 16 - phase transformations, nondiffusive," in *Physical Metallurgy (Fourth Edition)* (R. W. CAHN and P. HAASEN†, eds.), pp. 1507–1554, Oxford: North-Holland, fourth edition ed., 1996.

[22] K. He, Y. Wang, and Q.-K. Xue, "Topological materials: quantum anomalous hall system," *Annual Review of Condensed Matter Physics*, vol. 9, pp. 329–344, 2018.

[23] Z. S. Aliev, I. R. Amiraslanov, D. I. Nasonova, A. V. Shevelkov, N. A. Abdullayev, Z. A. Jahangirli, E. N. Orujlu, M. M. Otrokov, N. T. Mamedov, M. B. Babanly, *et al.*, "Novel ternary layered manganese bismuth tellurides of the mnte-bi2te3 system: Synthesis and crystal structure," *Journal of Alloys and Compounds*, vol. 789, pp. 443–450, 2019.

[24] Y. Deng, Y. Yu, M. Z. Shi, Z. Guo, Z. Xu, J. Wang, X. H. Chen, and Y. Zhang, "Quantum anomalous hall effect in intrinsic magnetic topological insulator mnbi2te4," *Science*, vol. 367, no. 6480, pp. 895–900, 2020.

[25] A. Gao, Y.-F. Liu, C. Hu, J.-X. Qiu, C. Tzschaschel, B. Ghosh, S.-C. Ho, D. Bérubé, R. Chen, H. Sun, *et al.*, "Layer hall effect in a 2d topological axion antiferromagnet," *Nature*, vol. 595, no. 7868, pp. 521–525, 2021.

[26] A. Gao, Y.-F. Liu, J.-X. Qiu, B. Ghosh, T. V. Trevisan, Y. Onishi, C. Hu, T. Qian, H.-J. Tien, S.-W. Chen, *et al.*, "Quantum metric nonlinear hall effect in a topological antiferromagnetic heterostructure," *Science*, vol. 381, no. 6654, pp. 181–186, 2023.

[27] K. Okamoto, K. Kuroda, H. Miyahara, K. Miyamoto, T. Okuda, Z. Aliev, M. Babanly, I. Amiraslanov, K. Shimada, H. Namatame, *et al.*, "Observation of a highly spin-polarized topological surface state in gebi 2 te 4," *Physical Review B*, vol. 86, no. 19, p. 195304, 2012.

[28] C. Hu, T. Qian, and N. Ni, "Recent progress in mnbi2 n te3 n+ 1 intrinsic magnetic topological insulators: crystal growth, magnetism and chemical disorder," *National Science Review*, vol. 11, no. 2, p. nwad282, 2024.

[29] L. Ding, C. Hu, F. Ye, E. Feng, N. Ni, and H. Cao, "Crystal and magnetic structures of magnetic topological insulators mnbi 2 te 4 and mnbi 4 te 7," *Physical Review B*, vol. 101, no. 2, p. 020412(R), 2020.

[30] L. Ding, C. Hu, E. Feng, C. Jiang, I. A. Kibalin, A. Gukasov, M. Chi, N. Ni, and H. Cao, "Neutron diffraction study of magnetism in van der waals layered mnbi2n te3n+ 1," *Journal of Physics D: Applied Physics*, vol. 54, no. 17, p. 174003, 2021.

[31] C. Hu, L. Ding, K. N. Gordon, B. Ghosh, H.-J. Tien, H. Li, A. G. Linn, S.-W. Lien, C.-Y. Huang, S. Mackey, *et al.*, "Realization of an intrinsic ferromagnetic topological state in mnbi8te13," *Science Advances*, vol. 6, no. 30, p. eaba4275, 2020.

[32] C. Hu, K. N. Gordon, P. Liu, J. Liu, X. Zhou, P. Hao, D. Narayan, E. Emmanouilidou, H. Sun, Y. Liu, *et al.*, "A van der waals antiferromagnetic topological insulator with weak interlayer magnetic coupling," *Nature communications*, vol. 11, no. 1, pp. 1–8, 2020.

[33] S. Tian, S. Gao, S. Nie, Y. Qian, C. Gong, Y. Fu, H. Li, W. Fan, P. Zhang, T. Kondo, *et al.*, "Magnetic topological insulator mnbi 6 te 10 with a zero-field ferromagnetic state and gapped dirac surface states," *Physical Review B*, vol. 102, no. 3, p. 035144, 2020.

[34] J.-Q. Yan, S. Okamoto, M. A. McGuire, A. F. May, R. J. McQueeney, and B. C. Sales, "Evolution of structural, magnetic, and transport properties in mnbi 2- x sb x te 4," *Physical Review B*, vol. 100, no. 10, p. 104409, 2019.

[35] Y. Liu, L.-L. Wang, Q. Zheng, Z. Huang, X. Wang, M. Chi, Y. Wu, B. C. Chakoumakos, M. A. McGuire, B. C. Sales, *et al.*, "Site mixing for engineering magnetic topological insulators," *Physical Review X*, vol. 11, no. 2, p. 021033, 2021.

[36] Y. Chen, Y.-W. Chuang, S. H. Lee, Y. Zhu, K. Honz, Y. Guan, Y. Wang, K. Wang, Z. Mao, J. Zhu, *et al.*, "Ferromagnetism in van der waals compound mns b 1.8 b i 0.2 t e 4," *Physical Review Materials*, vol. 4, no. 6, p. 064411, 2020.

[37] B. C. Chakoumakos, H. Cao, F. Ye, A. D. Stoica, M. Popovici, M. Sundaram, W. Zhou, J. S. Hicks, G. W. Lynn, and R. A. Riedel, "Four-circle single-crystal neutron diffractometer at the high flux isotope reactor," *Journal of Applied Crystallography*, vol. 44, no. 3, pp. 655–658, 2011.

[38] J. Rodríguez-Carvajal, "Recent advances in magnetic structure determination by neutron powder diffraction," *Physica B: Condensed Matter*, vol. 192, no. 1-2, pp. 55–69, 1993.

[39] K. Yokogawa, K. Murata, H. Yoshino, and S. Aoyama, "Solidification of high-pressure medium daphne 7373," *Japanese journal of applied physics*, vol. 46, no. 6R, p. 3636, 2007.

[40] M. Clark and T. Smith, "Pressure dependence of t_c for lead," *Journal of Low Temperature Physics*, vol. 32, no. 3, pp. 495–503, 1978.

[41] T. Qian, Y.-T. Yao, C. Hu, E. Feng, H. Cao, I. I. Mazin, T.-R. Chang, and N. Ni, "Magnetic dilution effect and topological phase transitions in (mn 1- x pb x) bi 2 te 4," *Physical Review B*, vol. 106, no. 4, p. 045121, 2022.

[42] D. S. Lee, T.-H. Kim, C.-H. Park, C.-Y. Chung, Y. S. Lim, W.-S. Seo, and H.-H. Park, "Crystal structure, properties and nanostructuring of a new layered chalcogenide semiconductor, bi 2 mnte 4," *CrystEngComm*, vol. 15, no. 27, pp. 5532–5538, 2013.

[43] M. M. Otrokov, I. I. Klimovskikh, H. Bentmann, D. Estyunin, A. Zeugner, Z. S. Aliev, S. Gaß, A. Wolter, A. Koroleva, A. M. Shikin, *et al.*, "Prediction and observation of an antiferromagnetic topological insulator," *Nature*, vol. 576, no. 7787, pp. 416–422, 2019.

[44] D. Zhang, M. Shi, T. Zhu, D. Xing, H. Zhang, and J. Wang, "Topological axion states in the magnetic insulator mnbi 2 te 4 with the quantized magnetoelectric effect," *Physical review letters*, vol. 122, no. 20, p. 206401, 2019.

[45] J. Li, Y. Li, S. Du, Z. Wang, B.-L. Gu, S.-C. Zhang, K. He, W. Duan, and Y. Xu, "Intrinsic magnetic topological insulators in van der waals layered mnbi2te4-family materials," *Science Advances*, vol. 5, no. 6, p. eaaw5685, 2019.

[46] M. M. Otrokov, I. P. Rusinov, M. Blanco-Rey, M. Hoffmann, A. Y. Vyazovskaya, S. V. Eremeev, A. Ernst, P. M. Echenique, A. Arnau, and E. V. Chulkov, "Unique thickness-dependent properties of the van der waals interlayer antiferromagnet mnbi 2 te 4 films," *Physical Review Letters*, vol. 122, no. 10, p. 107202, 2019.

[47] C. Liu, Y. Wang, H. Li, Y. Wu, Y. Li, J. Li, K. He, Y. Xu, J. Zhang, and Y. Wang, "Robust axion insulator and chern insulator phases in a two-dimensional antiferromagnetic topological insulator," *Nature Materials*, vol. 19, no. 5, pp. 522–527, 2020.

[48] J. Ge, Y. Liu, J. Li, H. Li, T. Luo, Y. Wu, Y. Xu, and J. Wang, "High-chern-number and high-temperature quantum hall effect without landau levels," *National science review*, vol. 7, no. 8, pp. 1280–1287, 2020.

[49] J. Wu, F. Liu, M. Sasase, K. Ienaga, Y. Obata, R. Yukawa, K. Horiba, H. Kumigashira, S. Okuma, T. Inoshita, *et al.*, "Natural van der waals heterostructural single crystals with both magnetic and topological properties," *Science advances*, vol. 5, no. 11, p. eaax9989, 2019.

[50] I. I. Klimovskikh, M. M. Otrokov, D. Estyunin, S. V. Eremeev, S. O. Filnov, A. Koroleva, E. Shevchenko, V. Voroshnin, A. G. Rybkin, I. P. Rusinov, *et al.*, "Tunable 3d/2d magnetism in the (mnbi 2 te 4)(bi 2 te 3) m topological insulators family," *npj Quantum Materials*, vol. 5, no. 1, pp. 1–9, 2020.

[51] M. Shi, B. Lei, C. Zhu, D. Ma, J. Cui, Z. Sun, J. Ying, and X. Chen, "Magnetic and transport properties in the magnetic topological insulators mnb i 2 t e 4 (b i 2 t e 3) n (n= 1, 2)," *Physical Review B*, vol. 100, no. 15, p. 155144, 2019.

[52] Y. Chen, L. Xu, J. Li, Y. Li, H. Wang, C. Zhang, H. Li, Y. Wu, A. Liang, C. Chen, *et al.*, "Topological electronic structure and its temperature evolution in antiferromagnetic topological insulator mnbi 2 te 4," *Physical Review X*, vol. 9, no. 4, p. 041040, 2019.

[53] S. H. Lee, Y. Zhu, Y. Wang, L. Miao, T. Pillsbury, H. Yi, S. Kempinger, J. Hu, C. A. Heikes, P. Quarterman, *et al.*, "Spin scattering and noncollinear spin structure-induced intrinsic anomalous hall effect in antiferromagnetic topological insulator mnb i 2 t e 4," *Physical Review Research*, vol. 1, no. 1, p. 012011(R), 2019.

[54] S. Tian, S. Gao, S. Nie, Y. Qian, C. Gong, Y. Fu, H. Li, W. Fan, P. Zhang, T. Kondo, S. Shin, J. Adell, H. Fedderwitz, H. Ding, Z. Wang, T. Qian, and H. Lei, "Magnetic topological insulator $mnbi_6te_{10}$ with a zero-field ferromagnetic state and gapped dirac surface states," *Phys. Rev. B*, vol. 102, p. 035144, Jul 2020.

[55] K. N. Gordon, H. Sun, C. Hu, A. G. Linn, H. Li, Y. Liu, P. Liu, S. Mackey, Q. Liu, N. Ni, *et al.*, "Strongly gapped topological surface states on protected surfaces of antiferromagnetic mnbi _4 te _7 and mnbi _6 te _{10}," *arXiv preprint arXiv:1910.13943*, 2019.

[56] K. Chen, B. Wang, J.-Q. Yan, D. Parker, J.-S. Zhou, Y. Uwatoko, and J.-G. Cheng, "Suppression of the antiferromagnetic metallic state in the pressurized mnb i 2 t e 4 single crystal," *Physical Review Materials*, vol. 3, no. 9, p. 094201, 2019.

[57] J. Shao, Y. Liu, M. Zeng, J. Li, X. Wu, X.-M. Ma, F. Jin, R. Lu, Y. Sun, M. Gu, *et al.*, "Pressure-tuned intralayer exchange in superlattice-like mnbi2te4/(bi2te3) n topological insulators," *Nano Letters*, vol. 21, no. 13, pp. 5874–5880, 2021.

[58] T. Qian, E. Emmanouilidou, C. Hu, J. C. Green, I. I. Mazin, and N. Ni, "Unconventional pressure-driven metamagnetic transitions in topological van der waals magnets," *Nano Letters*, vol. 22, no. 13, pp. 5523–5529, 2022. PMID: 35731986.

[59] B. Chen, F. Fei, D. Zhang, B. Zhang, W. Liu, S. Zhang, P. Wang, B. Wei, Y. Zhang, Z. Zuo, *et al.*, "Intrinsic magnetic topological insulator phases in the sb doped mnbi 2 te 4 bulks and thin flakes," *Nature communications*, vol. 10, no. 1, pp. 1–8, 2019.

[60] C. Hu, S.-W. Lien, E. Feng, S. Mackey, H.-J. Tien, I. I. Mazin, H. Cao, T.-R. Chang, and N. Ni, "Tuning magnetism and band topology through antisite defects in sb-doped mnbi 4 te 7," *Physical Review B*, vol. 104, no. 5, p. 054422, 2021.

[61] T. Murakami, Y. Nambu, T. Koretsune, G. Xiangyu, T. Yamamoto, C. M. Brown, and H. Kageyama, "Realization of interlayer ferromagnetic interaction in mns b 2 t e 4 toward the magnetic weyl semimetal state," *Physical Review B*, vol. 100, no. 19, p. 195103, 2019.

[62] Y. Lai, L. Ke, J. Yan, R. D. McDonald, and R. J. McQueeney, "Defect-driven ferrimagnetism and hidden magnetization in mnbi 2 te 4," *Physical Review B*, vol. 103, no. 18, p. 184429, 2021.

[63] C. Hu, A. Gao, B. S. Berggren, H. Li, R. Kurleto, D. Narayan, I. Zeljkovic, D. Dessau, S. Xu, and N. Ni, "Growth, characterization, and chern insulator state in mnbi 2 te 4 via the chemical vapor transport method," *Physical Review Materials*, vol. 5, no. 12, p. 124206, 2021.

[64] R. Matsumoto, Z. Hou, M. Nagao, S. Adachi, H. Hara, H. Tanaka, K. Nakamura, R. Murakami, S. Yamamoto, H. Takeya, *et al.*, "Data-driven exploration of new pressure-induced superconductivity in pbbi2te4," *Science and Technology of Advanced Materials*, vol. 19, no. 1, pp. 909–916, 2018.

[65] M. Frachet, I. Vinograd, R. Zhou, S. Benhabib, S. Wu, H. Mayaffre, S. Krämer, S. K. Ramakrishna, A. P. Reyes, J. Debray, *et al.*, "Hidden magnetism at the pseudogap critical point of a cuprate superconductor," *Nature Physics*, vol. 16, no. 10, pp. 1064–1068, 2020.

[66] K. Christensen, "Percolation theory," *Imperial College London*, vol. 1, p. 25, 2002.

[67] T. V. Menshchikova, S. V. Eremeev, Y. M. Koroteev, V. M. Kuznetsov, and E. V. Chulkov, "Ternary compounds based on binary topological insulators as an efficient way for modifying the dirac cone," *JETP letters*, vol. 93, no. 1, pp. 15–20, 2011.

[68] K. Kuroda, H. Miyahara, M. Ye, S. Eremeev, Y. M. Koroteev, E. Krasovskii, E. Chulkov, S. Hiramoto, C. Moriyoshi, Y. Kuroiwa, *et al.*, "Experimental verification of pbbi 2 te 4 as a 3d topological insulator," *Physical Review Letters*, vol. 108, no. 20, p. 206803, 2012.

[69] R. McQueeney. private communication, 2022.

[70] M. A. McGuire, G. Clark, K. Santosh, W. M. Chance, G. E. Jellison Jr, V. R. Cooper, X. Xu, and B. C. Sales, "Magnetic behavior and spin-lattice coupling in cleavable van der waals layered crcl 3 crystals," *Physical Review Materials*, vol. 1, no. 1, p. 014001, 2017.

[71] M. A. McGuire, H. Dixit, V. R. Cooper, and B. C. Sales, "Coupling of crystal structure and magnetism in the layered, ferromagnetic insulator cri3," *Chemistry of Materials*, vol. 27, no. 2, pp. 612–620, 2015.

[72] J. Zhu, M. Naveed, B. Chen, Y. Du, J. Guo, H. Xie, and F. Fei, "Magnetic and electrical transport study of the antiferromagnetic topological insulator sn-doped mnbi 2 te 4," *Physical Review B*, vol. 103, no. 14, p. 144407, 2021.

[73] K. Novoselov, A. Mishchenko, A. Carvalho, and A. C. Neto, "2d materials and van der waals heterostructures," *Science*, vol. 353, no. 6298, p. aac9439, 2016.

[74] C. Gong, L. Li, Z. Li, H. Ji, A. Stern, Y. Xia, T. Cao, W. Bao, C. Wang, Y. Wang, *et al.*, "Discovery of intrinsic ferromagnetism in two-dimensional van der waals crystals," *Nature*, vol. 546, no. 7657, pp. 265–269, 2017.

[75] Y. Deng, Y. Yu, Y. Song, J. Zhang, N. Z. Wang, Z. Sun, Y. Yi, Y. Z. Wu, S. Wu, J. Zhu, *et al.*, "Gate-tunable room-temperature ferromagnetism in two-dimensional fe_3gete_2," *Nature*, vol. 563, no. 7729, pp. 94–99, 2018.

[76] Z. Wang, T. Zhang, M. Ding, B. Dong, Y. Li, M. Chen, X. Li, J. Huang, H. Wang, X. Zhao, *et al.*, "Electric-field control of magnetism in a few-layered van der waals ferromagnetic semiconductor," *Nature nanotechnology*, vol. 13, no. 7, pp. 554–559, 2018.

[77] X. Sun, W. Li, X. Wang, Q. Sui, T. Zhang, Z. Wang, L. Liu, D. Li, S. Feng, S. Zhong, *et al.*, "Room temperature ferromagnetism in ultra-thin van der waals crystals of 1t-$crte_2$," *Nano Research*, vol. 13, no. 12, pp. 3358–3363, 2020.

[78] A. F. May, D. Ovchinnikov, Q. Zheng, R. Hermann, S. Calder, B. Huang, Z. Fei, Y. Liu, X. Xu, and M. A. McGuire, "Ferromagnetism near room temperature in the cleavable van der waals crystal fe_3gete_2," *ACS nano*, vol. 13, no. 4, pp. 4436–4442, 2019.

[79] E. Gati, Y. Inagaki, T. Kong, R. J. Cava, Y. Furukawa, P. C. Canfield, and S. L. Bud'Ko, "Multiple ferromagnetic transitions and structural distortion in the van der waals ferromagnet vi_3 at ambient and finite pressures," *Physical Review B*, vol. 100, no. 9, p. 094408, 2019.

[80] B. Huang, G. Clark, E. Navarro-Moratalla, D. R. Klein, R. Cheng, K. L. Seyler, D. Zhong, E. Schmidgall, M. A. McGuire, D. H. Cobden, *et al.*, "Layer-dependent ferromagnetism in a van der waals crystal down to the monolayer limit," *Nature*, vol. 546, no. 7657, pp. 270–273, 2017.

[81] B. Huang, G. Clark, D. R. Klein, D. MacNeill, E. Navarro-Moratalla, K. L. Seyler, N. Wilson, M. A. McGuire, D. H. Cobden, D. Xiao, *et al.*, "Electrical control of 2d magnetism in bilayer cri_3," *Nature nanotechnology*, vol. 13, no. 7, pp. 544–548, 2018.

[82] S. Jiang, L. Li, Z. Wang, K. F. Mak, and J. Shan, "Controlling magnetism in 2d cri_3 by electrostatic doping," *Nature nanotechnology*, vol. 13, no. 7, pp. 549–553, 2018.

[83] S. Jiang, J. Shan, and K. F. Mak, "Electric-field switching of two-dimensional van der waals magnets," *Nature materials*, vol. 17, no. 5, pp. 406–410, 2018.

[84] L. Webster and J.-A. Yan, "Strain-tunable magnetic anisotropy in monolayer $crcl_3$, $crbr_3$, and cri_3," *Physical Review B*, vol. 98, no. 14, p. 144411, 2018.

[85] Z. Wu, J. Yu, and S. Yuan, "Strain-tunable magnetic and electronic properties of monolayer cri_3," *Physical Chemistry Chemical Physics*, vol. 21, no. 15, pp. 7750–7755, 2019.

[86] T. Song, Z. Fei, M. Yankowitz, Z. Lin, Q. Jiang, K. Hwangbo, Q. Zhang, B. Sun, T. Taniguchi, K. Watanabe, *et al.*, "Switching 2d magnetic states via pressure tuning of layer stacking," *Nature materials*, vol. 18, no. 12, pp. 1298–1302, 2019.

[87] J. Cenker, S. Sivakumar, K. Xie, A. Miller, P. Thijssen, Z. Liu, A. Dismukes, J. Fonseca, E. Anderson, X. Zhu, *et al.*, "Reversible strain-induced magnetic phase transition in a van der waals magnet," *Nature Nanotechnology*, pp. 1–6, 2022.

[88] N. P. Wilson, K. Lee, J. Cenker, K. Xie, A. H. Dismukes, E. J. Telford, J. Fonseca, S. Sivakumar, C. Dean, T. Cao, *et al.*, "Interlayer electronic coupling on demand in a 2d magnetic semiconductor," *Nature Materials*, vol. 20, no. 12, pp. 1657–1662, 2021.

[89] C. Yan, Y. Zhu, S. Fernandez-Mulligan, E. Green, R. Mei, B. Yan, C. Liu, Z. Mao, and S. Yang, "Delicate ferromagnetism in $mnbi_6te_{10}$," *arXiv preprint arXiv:2107.08137*, 2021. visited on 06/13/2022.

[90] H. Xie, F. Fei, F. Fang, B. Chen, J. Guo, Y. Du, W. Qi, Y. Pei, T. Wang, M. Naveed, *et al.*, "Charge carrier mediation and ferromagnetism induced in $mnbi_6te_{10}$ magnetic topological insulators by antimony doping," *Journal of Physics D: Applied Physics*, vol. 55, no. 10, p. 104002, 2021.

[91] C. Pei, M. Xi, Q. Wang, W. Shi, J. Wu, L. Gao, Y. Zhao, S. Tian, W. Cao, C. Li, *et al.*, "Pressure-induced superconductivity in magnetic topological insulator candidate mnsb 4 te 7," *Physical Review Materials*, vol. 6, no. 10, p. L101801, 2022.

[92] L. Vinokurova, A. Vlasov, and M. Pardavi-Horváth, "Pressure effects on magnetic phase transitions in ferh and ferhir alloys," *physica status solidi (b)*, vol. 78, no. 1, pp. 353–357, 1976.

[93] E. Stern-Taulats, T. Castán, A. Planes, L. H. Lewis, R. Barua, S. Pramanick, S. Majumdar, and L. Manosa, "Giant multicaloric response of bulk fe 49 rh 51," *Physical Review B*, vol. 95, no. 10, p. 104424, 2017.

[94] A. A. Katanin and V. Y. Irkhin, "Magnetic order and spin fluctuations in low-dimensional insulating systems," *Physics-Uspekhi*, vol. 50, no. 6, p. 613, 2007.

[95] T. Qian, C. Hu, J. C. Green, E. Feng, H. Cao, and N. Ni, "Single crystal growth, chemical defects, magnetic and transport properties of antiferromagnetic topological insulators $(ge_{1-\delta-x}mn_x)_2bi_2te_5$ ($x \leq 0.47$, $0.11 \leq \delta \leq 0.20$)," *arXiv preprint arXiv:2404.17764*, 2024.

[96] J. Wang, B. Lian, X.-L. Qi, and S.-C. Zhang, "Quantized topological magnetoelectric effect of the zero-plateau quantum anomalous hall state," *Physical Review B*, vol. 92, no. 8, p. 081107, 2015.

[97] C.-X. Liu, S.-C. Zhang, and X.-L. Qi, "The quantum anomalous hall effect: Theory and experiment," *Annual Review of Condensed Matter Physics*, vol. 7, pp. 301–321, 2016.

[98] E. Rienks, S. Wimmer, J. Sánchez Barriga, O. Caha, P. Mandal, J. Růžička, A. Ney, H. Steiner, V. Volobuev, H. Groiss, *et al.*, "Large magnetic gap at the dirac point in bi 2 te 3/mnbi 2 te 4 heterostructures," *Nature*, vol. 576, no. 7787, pp. 423–428, 2019.

[99] Y. Gong, J. Guo, J. Li, K. Zhu, M. Liao, X. Liu, Q. Zhang, L. Gu, L. Tang, X. Feng, *et al.*, "Experimental realization of an intrinsic magnetic topological insulator," *Chinese Physics Letters*, vol. 36, no. 7, p. 076801, 2019.

[100] J.-Q. Yan, Q. Zhang, T. Heitmann, Z. Huang, K. Chen, J.-G. Cheng, W. Wu, D. Vaknin, B. C. Sales, and R. J. McQueeney, "Crystal growth and magnetic structure of mnbi 2 te 4," *Physical Review Materials*, vol. 3, no. 6, p. 064202, 2019.

[101] A. Zeugner, F. Nietschke, A. U. Wolter, S. Gaß, R. C. Vidal, T. R. Peixoto, D. Pohl, C. Damm, A. Lubk, R. Hentrich, *et al.*, "Chemical aspects of the candidate antiferromagnetic topological insulator mnbi2te4," *Chemistry of Materials*, vol. 31, no. 8, pp. 2795–2806, 2019.

[102] J.-Q. Yan, Y. Liu, D. Parker, Y. Wu, A. Aczel, M. Matsuda, M. McGuire, and B. Sales, "A-type antiferromagnetic order in mnbi 4 te 7 and mnbi 6 te 10 single crystals," *Physical Review Materials*, vol. 4, no. 5, p. 054202, 2020.

[103] H. Deng, Z. Chen, A. Wołłoś, M. Konczykowski, K. Sobczak, J. Sitnicka, I. V. Fedorchenko, J. Borysiuk, T. Heider, ŁL. Pluciński, K. Park, A. B. Georgescu, J. Cano, and L. Krusin Elbaum, "High-temperature quantum anomalous Hall regime in a MnBi2Te4/Bi2Te3 superlattice," *Nature Physics*, Aug. 2020.

[104] L. Shelimova, O. Karpinskii, P. Konstantinov, E. Avilov, M. Kretova, and V. Zemskov, "Crystal structures and thermoelectric properties of layered compounds in the ate–bi 2 te 3 (a= ge, sn, pb) systems," *Inorganic Materials*, vol. 40, no. 5, pp. 451–460, 2004.

[105] M. Neupane, S.-Y. Xu, L. A. Wray, A. Petersen, R. Shankar, N. Alidoust, C. Liu, A. Fedorov, H. Ji, J. M. Allred, *et al.*, "Topological surface states and dirac point tuning in ternary topological insulators," *Physical Review B*, vol. 85, no. 23, p. 235406, 2012.

[106] B. A. Kuropatwa and H. Kleinke, "Thermoelectric properties of stoichiometric compounds in the (snte) x (bi2te3) y system," *Zeitschrift für anorganische und allgemeine Chemie*, vol. 638, no. 15, pp. 2640–2647, 2012.

[107] A. Chatterjee and K. Biswas, "Solution-based synthesis of layered intergrowth compounds of the homologous pbmbi2nte3n+ m series as nanosheets," *Angewandte Chemie*, vol. 127, no. 19, pp. 5715–5719, 2015.

[108] T. Matsunaga, R. Kojima, N. Yamada, K. Kifune, Y. Kubota, and M. Takata, "Structures of stable and metastable ge2bi2te5, an intermetallic compound in a gete–bi2te3 pseudobinary system," *Acta Crystallographica Section B: Structural Science*, vol. 63, no. 3, pp. 346–352, 2007.

[109] Y. Li, Y. Jiang, J. Zhang, Z. Liu, Z. Yang, and J. Wang, "Intrinsic topological phases in mn 2 bi 2 te 5 tuned by the layer magnetization," *Physical Review B*, vol. 102, no. 12, p. 121107, 2020.

[110] J. Zhang, D. Wang, M. Shi, T. Zhu, H. Zhang, and J. Wang, "Large dynamical axion field in topological antiferromagnetic insulator mn2bi2te5," *Chinese Physics Letters*, vol. 37, no. 7, p. 077304, 2020.

[111] S. Eremeev, M. Otrokov, A. Ernst, and E. V. Chulkov, "Magnetic ordering and topology in mn 2 bi 2 te 5 and mn 2 sb 2 te 5 van der waals materials," *Physical Review B*, vol. 105, no. 19, p. 195105, 2022.

[112] Y. Li, Y. Jia, B. Zhao, H. Bao, H. Huan, H. Weng, and Z. Yang, "Stacking-layer-tuned topological phases in m 2 bi 2 te 5 (m= ge, sn, pb) films," *Physical Review B*, vol. 108, no. 8, p. 085428, 2023.

[113] X.-Y. Tang, Z. Li, F. Xue, P. Ji, Z. Zhang, X. Feng, Y. Xu, Q. Wu, and K. He, "Intrinsic and tunable quantum anomalous hall effect and magnetic topological phases in x y bi 2 te 5," *Physical Review B*, vol. 108, no. 7, p. 075117, 2023.

[114] J.-Q. Yan, Z. Huang, W. Wu, and A. F. May, "Vapor transport growth of mnbi2te4 and related compounds," *Journal of Alloys and Compounds*, vol. 906, p. 164327, 2022.

[115] L. Cao, S. Han, Y.-Y. Lv, D. Wang, Y.-C. Luo, Y.-Y. Zhang, S.-H. Yao, J. Zhou, Y. Chen, H. Zhang, *et al.*, "Growth and characterization of the dynamical axion insulator candidate mn 2 bi 2 te 5 with intrinsic antiferromagnetism," *Physical Review B*, vol. 104, no. 5, p. 054421, 2021.

[116] C. Hu, A. Gao, B. S. Berggren, H. Li, R. Kurleto, D. Narayan, I. Zeljkovic, D. Dessau, S. Xu, and N. Ni, "Growth, characterization, and chern insulator state in mnbi 2 te 4 via the chemical vapor transport method," *Physical Review Materials*, vol. 5, no. 12, p. 124206, 2021.

[117] R. Huisman, R. De Jonge, C. Haas, and F. Jellinek, "Trigonal-prismatic coordination in solid compounds of transition metals," *Journal of Solid State Chemistry*, vol. 3, no. 1, pp. 56–66, 1971.

[118] S. Yan, W. Qiao, D. Jin, X. Xu, W. Mi, and D. Wang, "Role of exchange splitting and ligand-field splitting in tuning the magnetic anisotropy of an individual iridium atom on ta s 2 substrate," *Physical Review B*, vol. 103, no. 22, p. 224432, 2021.

[119] T. Qian, M. H. Christensen, C. Hu, A. Saha, B. M. Andersen, R. M. Fernandes, T. Birol, and N. Ni, "Revealing the competition between charge density wave and superconductivity in csv 3 sb 5 through uniaxial strain," *Physical Review B*, vol. 104, no. 14, p. 144506, 2021.

[120] A. Gabovich, A. Voitenko, J. Annett, and M. Ausloos, "Charge-and spin-density-wave superconductors," *Superconductor Science and Technology*, vol. 14, no. 4, p. R1, 2001.

[121] X. Zhu, Y. Cao, J. Zhang, E. Plummer, and J. Guo, "Classification of charge density waves based on their nature," *Proceedings of the National Academy of Sciences*, vol. 112, no. 8, pp. 2367–2371, 2015.

[122] A. F. Kusmartseva, B. Sipos, H. Berger, L. Forró, and E. Tutiš, "Pressure induced superconductivity in pristine $1t-tise_2$," *Phys. Rev. Lett.*, vol. 103, p. 236401, Nov 2009.

[123] E. Morosan, H. W. Zandbergen, B. S. Dennis, J. W. G. Bos, Y. Onose, T. Klimczuk, A. P. Ramirez, N. P. Ong, and R. J. Cava, "Superconductivity in cuxtise2," *Nature Physics*, vol. 2, pp. 544–550, Aug 2006.

[124] T. Wu, H. Mayaffre, S. Krämer, M. Horvatić, C. Berthier, W. Hardy, R. Liang, D. Bonn, and M.-H. Julien, "Magnetic-field-induced charge-stripe order in the high-temperature superconductor $yba_2cu_3o_y$," *Nature*, vol. 477, no. 7363, pp. 191–194, 2011.

[125] J. Chang, E. Blackburn, A. Holmes, N. B. Christensen, J. Larsen, J. Mesot, R. Liang, D. Bonn, W. Hardy, A. Watenphul, *et al.*, "Direct observation of competition between superconductivity and charge density wave order in $yba_2cu_3o_{6.67}$," *Nature Physics*, vol. 8, no. 12, pp. 871–876, 2012.

[126] B. Sipos, A. F. Kusmartseva, A. Akrap, H. Berger, L. Forró, and E. Tutiš, "From mott state to superconductivity in 1t-tas 2," *Nature materials*, vol. 7, no. 12, pp. 960–965, 2008.

[127] Y. Feng, J. Wang, R. Jaramillo, J. Van Wezel, S. Haravifard, G. Srajer, Y. Liu, Z.-A. Xu, P. Littlewood, and T. Rosenbaum, "Order parameter fluctuations at a buried quantum critical point," *Proceedings of the National Academy of Sciences*, vol. 109, no. 19, pp. 7224–7229, 2012.

[128] B. R. Ortiz, L. C. Gomes, J. R. Morey, M. Winiarski, M. Bordelon, J. S. Mangum, I. W. H. Oswald, J. A. Rodriguez-Rivera, J. R. Neilson, S. D. Wilson, E. Ertekin, T. M. McQueen, and E. S. Toberer, "New kagome prototype materials: discovery of kv_3sb_5, rbv_3sb_5, and csv_3sb_5," *Phys. Rev. Materials*, vol. 3, p. 094407, Sep 2019.

[129] B. R. Ortiz, P. M. Sarte, E. M. Kenney, M. J. Graf, S. M. L. Teicher, R. Seshadri, and S. D. Wilson, "Superconductivity in the $\mathbb{Z}_2$ kagome metal kv_3sb_5," *Phys. Rev. Materials*, vol. 5, p. 034801, Mar 2021.

[130] B. R. Ortiz, S. M. L. Teicher, Y. Hu, J. L. Zuo, P. M. Sarte, E. C. Schueller, A. M. M. Abeykoon, M. J. Krogstad, S. Rosenkranz, R. Osborn, R. Seshadri, L. Balents, J. He, and S. D. Wilson, "Csv_3sb_5: A $\mathbb{Z}_2$ topological kagome metal with a superconducting ground state," *Phys. Rev. Lett.*, vol. 125, p. 247002, Dec 2020.

[131] Q. Yin, Z. Tu, C. Gong, Y. Fu, S. Yan, and H. Lei, "Superconductivity and normal-state properties of kagome metal rbv3sb5 single crystals," *Chinese Physics Letters*, vol. 38, p. 037403, Mar 2021.

[132] H. Chen, H. Yang, B. Hu, Z. Zhao, J. Yuan, Y. Xing, G. Qian, Z. Huang, G. Li, Y. Ye, S. Ma, S. Ni, H. Zhang, Q. Yin, C. Gong, Z. Tu, H. Lei, H. Tan, S. Zhou, C. Shen, X. Dong, B. Yan, Z. Wang, and H.-J. Gao, "Roton pair density wave in a strong-coupling kagome superconductor," *Nature*, 2021.

[133] Z. Liang, X. Hou, F. Zhang, W. Ma, P. Wu, Z. Zhang, F. Yu, J.-J. Ying, K. Jiang, L. Shan, Z. Wang, and X.-H. Chen, "Three-dimensional charge density wave and surface-dependent vortex-core states in a kagome superconductor csv_3sb_5," *Phys. Rev. X*, vol. 11, p. 031026, Aug 2021.

[134] H. Tan, Y. Liu, Z. Wang, and B. Yan, "Charge density waves and electronic properties of superconducting kagome metals," *Phys. Rev. Lett.*, vol. 127, p. 046401, Jul 2021.

[135] H. Li, T. T. Zhang, T. Yilmaz, Y. Y. Pai, C. E. Marvinney, A. Said, Q. W. Yin, C. S. Gong, Z. J. Tu, E. Vescovo, C. S. Nelson, R. G. Moore, S. Murakami, H. C. Lei, H. N. Lee, B. J. Lawrie, and H. Miao, "Observation of unconventional charge density wave without acoustic phonon anomaly in kagome superconductors AV_3sb_5 (a = Rb, cs)," *Phys. Rev. X*, vol. 11, p. 031050, Sep 2021.

[136] H. Zhao, H. Li, B. R. Ortiz, S. M. L. Teicher, T. Park, M. Ye, Z. Wang, L. Balents, S. D. Wilson, and I. Zeljkovic, "Cascade of correlated electron states in a kagome superconductor csv3sb5," *Nature*, 2021.

[137] B. R. Ortiz, S. M. Teicher, L. Kautzsch, P. M. Sarte, J. P. Ruff, R. Seshadri, and S. D. Wilson, "Fermi surface mapping and the nature of charge density wave order in the kagome superconductor csv _3 sb _5," *arXiv preprint arXiv:2104.07230*, 2021.

[138] Y.-X. Jiang, J.-X. Yin, M. M. Denner, N. Shumiya, B. R. Ortiz, G. Xu, Z. Guguchia, J. He, M. S. Hossain, X. Liu, J. Ruff, L. Kautzsch, S. S. Zhang, G. Chang, I. Belopolski, Q. Zhang, T. A. Cochran, D. Multer, M. Litskevich, Z.-J. Cheng, X. P. Yang, Z. Wang, R. Thomale, T. Neupert, S. D. Wilson, and M. Z. Hasan, "Unconventional chiral charge order in kagome superconductor kv3sb5," *Nature Materials*, vol. 20, no. 10, pp. 1353–1357, 2021.

[139] C. Mielke III, D. Das, J.-X. Yin, H. Liu, R. Gupta, C. Wang, Y.-X. Jiang, M. Medarde, X. Wu, H. Lei, *et al.*, "Time-reversal symmetry-breaking charge order in a correlated kagome superconductor," *arXiv preprint arXiv:2106.13443*, 2021.

[140] N. Shumiya, M. S. Hossain, J.-X. Yin, Y.-X. Jiang, B. R. Ortiz, H. Liu, Y. Shi, Q. Yin, H. Lei, S. S. Zhang, *et al.*, "Intrinsic nature of chiral charge order in the kagome superconductor rb v 3 sb 5," *Physical Review B*, vol. 104, no. 3, p. 035131, 2021.

[141] H. Li, H. Zhao, B. R. Ortiz, T. Park, M. Ye, L. Balents, Z. Wang, S. D. Wilson, and I. Zeljkovic, "Rotation symmetry breaking in the normal state of a kagome superconductor kv3sb5," *arXiv preprint arXiv:2104.08209*, 2021.

[142] C. Zhao, L. Wang, W. Xia, Q. Yin, J. Ni, Y. Huang, C. Tu, Z. Tao, Z. Tu, C. Gong, *et al.*, "Nodal superconductivity and superconducting domes in the topological kagome metal csv3sb5," *arXiv preprint arXiv:2102.08356*, 2021.

[143] K. Chen, N. Wang, Q. Yin, Y. Gu, K. Jiang, Z. Tu, C. Gong, Y. Uwatoko, J. Sun, H. Lei, *et al.*, "Double superconducting dome and triple enhancement of t c in the kagome superconductor csv 3 sb 5 under high pressure," *Physical Review Letters*, vol. 126, no. 24, p. 247001, 2021.

[144] F. H. Yu, D. H. Ma, W. Z. Zhuo, S. Q. Liu, X. K. Wen, B. Lei, J. J. Ying, and X. H. Chen, "Unusual competition of superconductivity and charge-density-wave state in a compressed topological kagome metal," *Nature Communications*, vol. 12, no. 1, p. 3645, 2021.

[145] Z. Zhang, Z. Chen, Y. Zhou, Y. Yuan, S. Wang, J. Wang, H. Yang, C. An, L. Zhang, X. Zhu, *et al.*, "Pressure-induced reemergence of superconductivity in the topological kagome metal cs v 3 sb 5," *Physical Review B*, vol. 103, no. 22, p. 224513, 2021.

[146] X. Chen, X. Zhan, X. Wang, J. Deng, X.-B. Liu, X. Chen, J.-G. Guo, and X. Chen, "Highly robust reentrant superconductivity in csv3sb5 under pressure," *Chinese Physics Letters*, vol. 38, p. 057402, Jun 2021.

[147] A. A. Tsirlin, P. Fertey, B. R. Ortiz, B. Klis, V. Merkl, M. Dressel, S. D. Wilson, and E. Uykur, "Anisotropic compression and role of sb in the superconducting kagome metal csv _3 sb _5," *arXiv preprint arXiv:2105.01397*, 2021.

[148] W. Duan, Z. Nie, S. Luo, F. Yu, B. R. Ortiz, L. Yin, H. Su, F. Du, A. Wang, Y. Chen, and et al., "Nodeless superconductivity in the kagome metal csv3sb5," *Science China Physics, Mechanics & Astronomy*, vol. 64, Jul 2021.

[149] J. Mutch, W.-C. Chen, P. Went, T. Qian, I. Z. Wilson, A. Andreev, C.-C. Chen, and J.-H. Chu, "Evidence for a strain-tuned topological phase transition in zrte5," *Science advances*, vol. 5, no. 8, p. eaav9771, 2019.

[150] A. Stern, M. Dzero, V. Galitski, Z. Fisk, and J. Xia, "Surface-dominated conduction up to 240 k in the kondo insulator smb 6 under strain," *Nature materials*, vol. 16, no. 7, pp. 708–711, 2017.

[151] J.-H. Chu, H.-H. Kuo, J. G. Analytis, and I. R. Fisher, "Divergent nematic susceptibility in an iron arsenide superconductor," *Science*, vol. 337, no. 6095, pp. 710–712, 2012.

[152] C. W. Hicks, D. O. Brodsky, E. A. Yelland, A. S. Gibbs, J. A. Bruin, M. E. Barber, S. D. Edkins, K. Nishimura, S. Yonezawa, Y. Maeno, *et al.*, "Strong increase of tc of sr2ruo4 under both tensile and compressive strain," *Science*, vol. 344, no. 6181, pp. 283–285, 2014.

[153] T. Kissikov, R. Sarkar, M. Lawson, B. Bush, E. I. Timmons, M. A. Tanatar, R. Prozorov, S. Bud'ko, P. C. Canfield, R. Fernandes, *et al.*, "Uniaxial strain control of spin-polarization in multicomponent nematic order of bafe 2 as 2," *Nature communications*, vol. 9, no. 1, pp. 1–6, 2018.

[154] C. W. Hicks, M. E. Barber, S. D. Edkins, D. O. Brodsky, and A. P. Mackenzie, "Piezoelectric-based apparatus for strain tuning," *Review of Scientific Instruments*, vol. 85, no. 6, p. 065003, 2014.

[155] G. Kresse and J. Hafner, "Ab initio molecular dynamics for liquid metals," *Phys. Rev. B*, vol. 47, pp. 558–561, Jan 1993.

[156] G. Kresse and J. Furthmüller, "Efficiency of ab-initio total energy calculations for metals and semiconductors using a plane-wave basis set," *Computational materials science*, vol. 6, no. 1, pp. 15–50, 1996.

[157] G. Kresse and J. Furthmüller, "Efficient iterative schemes for ab initio total-energy calculations using a plane-wave basis set," *Physical Review B*, vol. 54, pp. 11169–11186, Oct 1996.

[158] J. P. Perdew, A. Ruzsinszky, G. I. Csonka, O. A. Vydrov, G. E. Scuseria, L. A. Constantin, X. Zhou, and K. Burke, "Restoring the density-gradient expansion for exchange in solids and surfaces," *Physical review letters*, vol. 100, p. 136406, Apr 2008.

[159] M. H. Christensen, T. Birol, B. M. Andersen, and R. M. Fernandes, "Theory of the charge-density wave in $a\mathrm{v}_3\mathrm{sb}_5$ kagome metals," *arXiv preprint arXiv:2107.04546*, 2021.

[160] M. Kang, S. Fang, J.-K. Kim, B. R. Ortiz, J. Yoo, B.-G. Park, S. D. Wilson, J.-H. Park, and R. Comin, "Twofold van hove singularity and origin of charge order in topological kagome superconductor csv3sb5," *arXiv preprint arXiv:2105.01689*, 2021.

[161] S. Cho, H. Ma, W. Xia, Y. Yang, Z. Liu, Z. Huang, Z. Jiang, X. Lu, J. Liu, Z. Liu, *et al.*, "Emergence of new van hove singularities in the charge density wave state of a topological kagome metal rbv3sb5," *arXiv preprint arXiv:2105.05117*, 2021.

[162] Y. Hu, X. Wu, B. R. Ortiz, S. Ju, X. Han, J. Ma, N. Plumb, M. Radovic, R. Thomale, S. Wilson, *et al.*, "Rich nature of van hove singularities in kagome superconductor csv _3 sb _5," *arXiv preprint arXiv:2106.05922*, 2021.

[163] R. Nandkishore, L. S. Levitov, and A. V. Chubukov, "Chiral superconductivity from repulsive interactions in doped graphene," *Nature Physics*, vol. 8, pp. 158–163, Feb 2012.

[164] M. L. Kiesel, C. Platt, and R. Thomale, "Unconventional fermi surface instabilities in the kagome hubbard model," *Phys. Rev. Lett.*, vol. 110, p. 126405, Mar 2013.

[165] W.-S. Wang, Z.-Z. Li, Y.-Y. Xiang, and Q.-H. Wang, "Competing electronic orders on kagome lattices at van hove filling," *Phys. Rev. B*, vol. 87, p. 115135, Mar 2013.

[166] X. Wu, T. Schwemmer, T. Müller, A. Consiglio, G. Sangiovanni, D. Di Sante, Y. Iqbal, W. Hanke, A. P. Schnyder, M. M. Denner, *et al.*, "Nature of unconventional pairing in the kagome superconductors av _3 sb _5," *arXiv preprint arXiv:2104.05671*, 2021.